# Polarization Enhanced Texture Analysis

With Applications to Precision Agriculture

*by*

Nicholas Ericksen

A document submitted in partial fulfillment of the requirements for the degree of

*Masters of Science*

at

Manhattan College

This document certifies that the following committee members have reviewed and approved the thesis, *"Polarization Enhanced Texture Analysis: With Applications to Precision Agriculture"* by Nicholas Ericksen, for the partial fulfillment of the requirements towards a degree of Masters of Science at Manhattan College. The student, Nicholas Ericksen, hereby affirms this work is inline with the guidelines previously set forth by scientific and academic thought.

| | |
|---|---|
| Dr. Romeo Pascone, Advisor | Dr. Brent Horine |
| _____ | _____ |
| *Signature* | *Signature* |
| _____ | _____ |
| *Date* | *Date* |
| Dr. Yi Wang | Mr. Nicholas Ericksen |
| _____ | _____ |
| *Signature* | *Signature* |
| _____ | _____ |
| *Date* | *Date* |

## Abstract

As agricultural inputs, such as water and fertilizer, become scarce a higher level of precision will be required when utilizing these resources in food production. Remote sensing is a field that aims to understand data from radiation reflected from vegetation. Determination of water content with remote sensing techniques of vegetation remains a long term goal. Furthermore as agricultural production has shifted to indoor growing environments, the use of indoor sensors at smaller scales may prove to be useful for determining the physiological status of crops. In this study the use of texture, polarization and pseudo-spectral features captured in the acquired images are shown to be useful for the successful classification of three different deciduous tree species common to the northeastern part of the United States using a linear support vector classifier. The observations are extended to the intra-class variance of the derived features which are shown to be useful for the prediction of the relative water content of individual leaves when analyzed using linear regression in the specular direction.

## Acknowledgments

For my parents, family and friends who have continuously demonstrated support in my pursuit of happiness.

A special thanks to Dr. Romeo Pascone, Dr. George Giakos, and Dr. Mark DeBonis whose input on this journey has been of great benefit.

The work performed in obtaining the resulting data could not have been accomplished without support from the labs at Manhattan College in the areas of Exploratory Image Research, Biology and Environmental Engineering.

# Contents

# List of Figures

# List of Tables

# 1 Introduction

> "The motion of a pendulum has exerted a fascination for human minds since the first savage watched the swaying of the first tree branch. The smooth sinusoidal motion back and forth, seems to express some secret of the universe… Indeed, nature loves the sinusoid".
>
> *Linear Circuits, Scott[1]*

The natural environment contains a finite amount of resources. It provides a limiting principle to the uncontrolled, exponential capital growth of consumerism. If ancient civilization describes itself as a political social animal, modern culture must append the term consumer. Consumption of these resources is occurring at an increasing rate, as the world's population increases, putting a strain on the modern agricultural system. In 1798 Thomas Malthus wrote in his "Essay on the Principal of Population" that the standard of living would eventually be undermined as population grows exponentially, and food supplies grow geometrically. He predicted this would eventually lead to mass food shortages and famine.

Today precision agriculture attempts to reduce the number of inputs to a farm, while maximizing its outputs. Its goal is the management of agricultural inputs on an individual plant basis. Minimizing water and fertilizer inputs are of central importance to this problem.

The areas of remote sensing, image processing, and machine learning have all been aided by advances in modern computing power. The application of these disciplines to areas of precision agriculture are widespread.

Remote sensing in particular has had a tremendous impact on precision agricultural as it opens up the possibility of large area surveying and field health assessment. Recently satellite data has been made easily available to the public through hosting on Amazon Web Services S3 buckets. They include data from Landsat 8, the Geostationary Operational Environmental Satellites (GOES), NASA Earth Exchange (NEX), and the National Agricultural Imagery Program (NAIP). These datasets contain information on various spectral responses recorded by various satellites. Some of the datasets also contain scenes captured through polarization filters oriented at various angles. These polarization images can be useful for deriving certain backscatter and volume scattering properties of the scene under investigation and have been utilized by [2], [3].

When interpreting data of remotely sensed vegetation, it is important to understand the scattering mechanisms inherent to the various features found within a particular image. This includes scattering from background objects such as soil, man made objects, canopies, etc. as well as target objects such as crops. Canopies are made up of individual leaves. The scattering mechanisms that occur from each leaf can provide an increased insight into the larger effects evident in canopies. More precise models can then be created for the purpose of extrapolating micro level effects to the macro level.

Furthermore, as more agricultural operations move indoors, information acquired from cameras monitoring these greenhouses can provide insights into the health and growth stages of various crops. Research into building greenhouses in space for the colonization of other planets, has grown substantially recently, with programs such as SpaceX looking into the possibility of placing a greenhouse on Mars. This provides an opportunity for utilizing image sensors into confined growing areas for monitoring plants on a micro scale.

Vegetation indices (VI) have been created for quantifying the health of land plants from remotely sensed data. These indices rely on the spectral signatures exhibited by plants that vary with the state of a vegetation's health [4]. It is possible that these ideas can be applied to smaller scale indoor scenarios as well.

Additional image processing can result in texture features being extracted from images for the purposes of segmentation and texture based classification. It has been found that certain materials when captured from satellites and other airborne imaging devices, exhibit texture signatures that can be useful for these purposes [5].

Machine learning techniques have been applied to a large number of different research areas. Their usefulness for classification and regression problems in the agricultural and environmental fields has been demonstrated for the purposes of plant disease detection and prevention, plant discrimination, levee management, etc. [2], [6], [7], [8], [9].

As consumer drones have entered the marketplace, it has become more reasonable for smaller scale farmers to utilize these remote sensors for monitoring there fields. Consumer off the shelf (COTS) cameras have also decreased in price, allowing for cheap installation and modification for the purpose of agricultural monitoring at different scales.

This work investigates the effects of light reflected from individual plant leaves by multiple scattering mechanisms using a COTS camera at a micro scale. This information is intended to be useful for the purpose of classification and ultimately determining the health of a plant based on the physiological properties of individual leaves by observing their polarization and texture properties as detected by the camera. As resources become more scare, and the price of certain technologies decreases, the impact of utilizing information acquired by these sensors for precision agricultural will be large.

# 2 Background

"The interaction between material bodies can be described either by formuating the action at a distance between the interacting bodies or by separating the interaction process into the production of a field by one system and the action of the field on another system".

*Classical Electricity & Magnetism. Panofksy, Phillips*

## 2.1 The Nature of Light and the Electromagnetic Spectrum

Light is fundamental to life. In Maxwell's' theory on light he explained how electromagnetic phenomenon can be expressed in terms of waves [10]. These waves move at the speed of light. The light that human eyes can detect is a small portion of the electromagnetic spectrum called 'visible light'. Different frequencies of light correspond to different colors on the visible spectrum. These

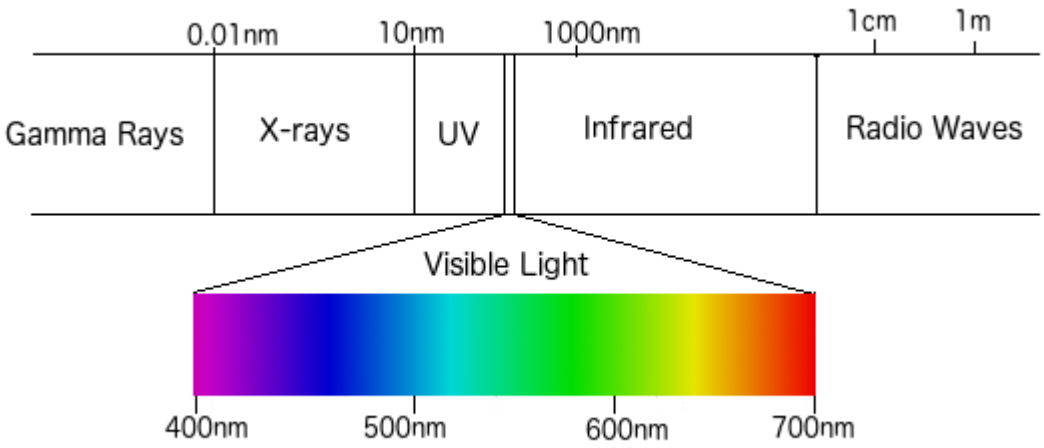


Figure 2.1: Electromagnetic Spectrum - Partial

waves are made up of two parts, the electric and magnetic. Due to their similar nature often only the electrical portion is considered at first for mathematical simplicity.

The electrical portion of EM waves, and the only portion considered here, can be described as the sum of two sinusoidal waves representing the orthogonal x and y components in Cartesian space.

$$E(z,t) = E_x(t) + E_y(t) \tag{2.1}$$
$$E_x(t) = E_{0x}cos(\theta + \delta_x) \tag{2.2}$$
$$E_y(t) = E_{0y}cos(\theta + \delta_y) \tag{2.3}$$

where $\theta = \omega t - kz$ is the wave propagator that determines the frequency and direction of propagation for the wave. $\delta_y$ and $\delta_x$ represent the phase delay for each component of the wave.

When more than one sine wave is considered, as in the case of EM waves, an overall phase delay between the them is considered and represented as $\delta = \delta_y - \delta_x$. $E_{0x}$ and $E_{0y}$ represent the amplitudes of the sinusoidal wave in the $x$ and $y$ direction.

Light can also be viewed as packets of energy known as photons. The energy of photons is related to its frequency $v$ and a constant, known as Planck's constant $h$ [11].

$$h = 6.62 \times 10^{-34}[m^2kg/s] \tag{2.4}$$
$$E = hv[Joules] \tag{2.5}$$

This simple equation shows that for higher frequencies, particles have higher energy.

### 2.1.1 Polarization of EM Waves

The polarization of EM waves is determined, for monochromatic frequencies, by the relative intensity and phase of their respective $x$ and $y$ components. These relationships can be viewed as the path traced by the tip of the electric field vector when looking in the direction of illumination. Common sources of illumination are lasers, light emitting diodes, halogen lamps, the sun, etc.

In its most general form, the polarization is referred to as being elliptical, and its $x$ and $y$ amplitudes, and phase delay can be described in the form of the polarization ellipse.

It has been shown that the form of the polarization ellipse can be derived from the solution to the plane wave equation for the electromagnetic wave. Using the relationships defined in the previous section and defining,

$$\tau = \omega t - kz + \delta_x \tag{2.6}$$

We can then define the $x$ and $y$ component of the wave as

$$E_x(t) = E_{0x}cos(\tau) \tag{2.7}$$
$$E_y(t) = E_{0y}cos(\tau + \delta) \tag{2.8}$$

Dividing each equation by its intensity results in

$$\frac{E_x(t)}{E_{0x}} = cos(\tau) \tag{2.9}$$

$$\frac{E_y(t)}{E_{0y}} = cos(\tau + \delta) \tag{2.10}$$

The $y$ component is then separated using known trigonometric identities and equation

$$\frac{E_y(t)}{E_{0y}} = (cos(\tau)cos(\delta) - sin(\tau)sin(\delta)) \tag{2.11}$$

Again using known trigonometric identities

$$\frac{E_y(t)}{E_{0y}} = \frac{E_x(t)}{E_{0x}}cos(\delta) - \sqrt{1 - \frac{E_x(t)^2}{E_{0x}^2}}sin(\delta) \tag{2.12}$$

Rearranging and squaring both sides results in

$$(\frac{E_x(t)}{E_{0x}}cos(\delta) - \frac{E_y(t)}{E_{0y}})^2 = (\sqrt{1 - \frac{E_x(t)^2}{E_{0x}^2}}sin(\delta))^2 \tag{2.13}$$

The factorization of this equation can be rearranged into the standard form of an ellipse such that

$$\frac{E_x(t)^2}{E_{0x}^2} + \frac{E_y(t)^2}{E_{0y}^2} - 2\frac{E_xE_y}{E_{0x}E_{0y}}cos(\delta) = sin^2(\delta) \tag{2.14}$$

And is graphed as seen in Figure 2.2.

Due to the restraints of modern optical sensors, it is not possible to directly measure the polarization ellipse, for a light beam, at any instant in time. Taking the time average of the ellipse results in quantities that can measured by detectors in order to quantify the polarization state of an EM wave. It is therefore necessary to derive parameters from the ellipse that can be measured. Starting from the equation for the polarization ellipse, taking the time average of the E field results in

$$\frac{E_x(t)^2}{E_{0x}^2} + \frac{E_y(t)^2}{E_{0y}^2} - \frac{2E_x(t)E_y(t)}{E_{0x}E_{0y}}cos(\delta) = sin^2(\delta) \tag{2.15}$$

the time averages are calculated as

$$< E_x(t)^2 >= lim_{T\to\infty}\int_0^{2\pi} E_{0x}cos(\tau)d\tau = \frac{1}{2}E_{0x}^2 \tag{2.16}$$

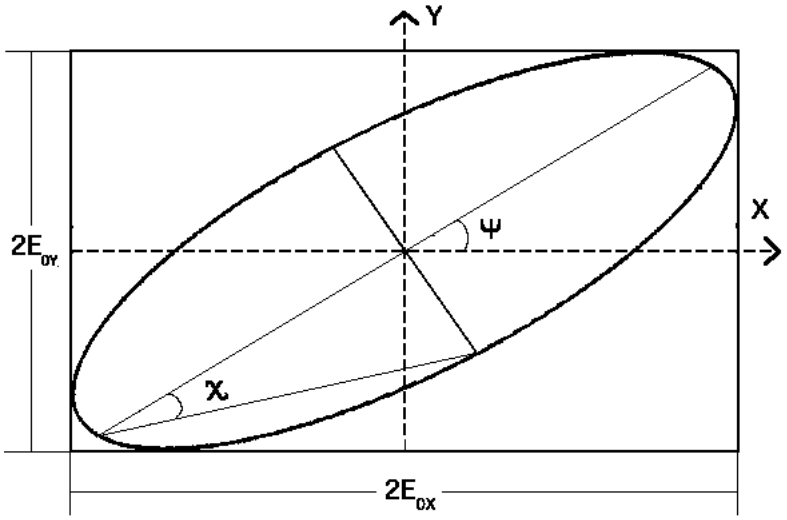


Figure 2.2: Polarization Ellipse

and similarly

$$< E_y(t)^2 >= \frac{1}{2}E_{0y}^2 \tag{2.17}$$

$$< E_x(t)E_y(t) >= \frac{1}{2}E_{0x}E_{0y}cos(\delta) \tag{2.18}$$

substitution into equation and completing the square results in

$$(E_{0x}^2 + E_{0x}^2)^2 - (E_{0x}^2 - E_{0x}^2)^2 - (2E_{0x}^2E_{0x}^2cos(\delta))^2 = (2E_{0x}E_{0y}sin(\delta))^2 \tag{2.19}$$

The terms of this equation represent the polarization state of a wave in relation to the x and y intensities and relative phase delay between the two components. These quantities are known as the Stokes parameters and describe the state of polarization and are often represented as a vector,

$$\vec{S} = \begin{bmatrix} S_0 \\ S_1 \\ S_2 \\ S_3 \end{bmatrix} = \begin{bmatrix} E_{0x}^2 + E_{0y}^2 \\ E_{0x}^2 - E_{0y}^2 \\ 2E_{0x}^2E_{0y}^2cos(\delta) \\ 2E_{0x}E_{0y}sin(\delta) \end{bmatrix} \tag{2.20}$$

The degree of polarization for an EM wave is the magnitude of the Stokes vector such that

$$\alpha = DOP = \frac{\sqrt{S_1^2 + S_2^2 + S_3^2}}{S_0} \tag{2.21}$$

and ranges from 0 for unpolarized light, to 1 for completely polarized light. It is possible to show the polarized and unpolarized intensities as individual components summed together as

$$S = S_P + S_U = \begin{bmatrix} S_0 \\ S_1 \\ S_2 \\ S_3 \end{bmatrix} + (1 - DOP) \begin{bmatrix} 1 \\ 0 \\ 0 \\ 0 \end{bmatrix} \tag{2.22}$$

The degree of polarization for the linear (DOLP) and circular polarization (DOCP) can specifically be quantified as

$$DOLP = \frac{\sqrt{S_1^2 + S_2^2}}{S_0} \tag{2.23}$$

$$DOCP = \frac{S_3}{S_0} \tag{2.24}$$

Note the unpolarized light is represented as

$$S = \begin{bmatrix} S_0 \\ S_1 \\ S_2 \\ S_3 \end{bmatrix} = \begin{bmatrix} 1 \\ 0 \\ 0 \\ 0 \end{bmatrix} \tag{2.25}$$

The Stokes parameters can be graphed on a unit sphere, known as the Poincare sphere. The sphere plots the radial coordinates describing ellipticity and eccentricy of the polarization ellipse as angles of

$$Ellipicity = \frac{S_3}{S_0 + \sqrt{S_1^2 + S_2^2}} \tag{2.26}$$

$$Eccentricity = \sqrt{1 - Ellipticity^2} \tag{2.27}$$

The ellipticity of the polarization ellipse varies from 0, for linearly polarized light, to 1 for purely circular polarization [12]. For graphical representation, Stokes vectors can be plotted on a 3-dimensional sphere known as the Poincare sphere. The sphere is only capable of showing the polarized portion of the EM wave. Prior to normalization, if the EM wave is not fully polarized, the intensity of the polarized beam must be normalized in relation to the total beam intensity. The zenith angle of the polarization ellipse, represented in Figure 2.3 as $2\chi$ is found to be related to the parameters of the polarization ellipse by

$$sin2\chi = \frac{2E_{0x}2E_{0y}sin\delta}{E_{0x}^2 + E_{0y}^2} \qquad -\pi/4 \leq \chi \leq \pi/4 \tag{2.28}$$

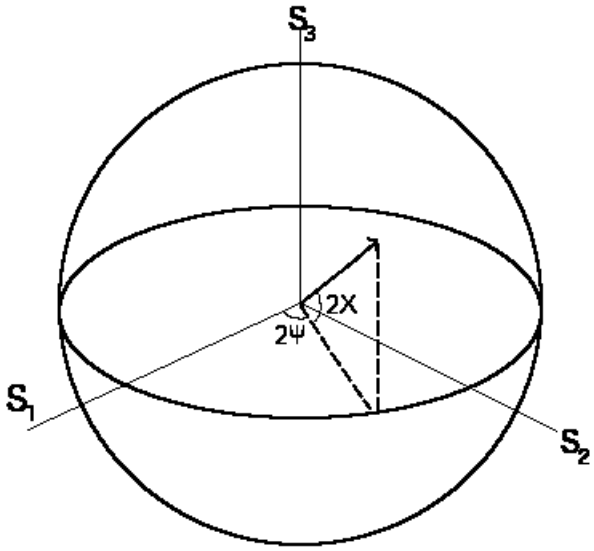


Figure 2.3: Poincare Sphere

The azimuth angle $2\psi$ is defined in relation to the parameters of the polarization ellipse as

$$tan2\psi = \frac{2E_{0x}2E_{0y}cos\delta}{E_{0x}^2 - E_{0y}^2} \qquad 0 \leq \psi \leq \pi \tag{2.29}$$

For a given state of the polarization ellipse, the angles for plotting the corresponding polarization state on the Poincare sphere can be found using these equations[13].

### 2.1.2 Jones Vector Representation

For the special case of fully polarized EM waves, DOP = 1, the polarization of the beam can be described by a 2x1 complex vector known as a Jones vector. The Jones vector relies on the fact that the polarization state of a beam depends only on its relative $x$ and $y$ intensities, as well as the phase delay between each respective component.

Converting the equation for the electric component of the EM wave into a phasor makes it easy to see the parameters that determine the beam's polarization. A phasor represents a sinusoidal wave with a constant frequency. The Jones vectors can be formulated from this representation as

$$\underline{\hat{E}}(z) = (\vec{i_x}E_{0x}e^{j\delta_x} + \vec{i_y}E_{0y}e^{j\delta_y})e^{-kz} \tag{2.30}$$

since the polarization depends on the amplitude and phase difference of the $X$ and $Y$ components, the Jones vector is formally written as

$$\underline{J} = \begin{bmatrix} E_{0x}e^{j\delta_x} \\ E_{0y}e^{j\delta_y} \end{bmatrix} \tag{2.31}$$

Since only the relative phase differences matter it is common to denote $\delta = \delta_y - \delta_x$. The vector is also normalized by dividing by its magnitude,

$$\underline{J} = \frac{1}{\sqrt{E_{0x}^2 + E_{0y}^2}} \begin{bmatrix} E_{0x}e^{j\delta_x} \\ E_{0y}e^{j\delta_y} \end{bmatrix} \tag{2.32}$$

An angle can then be defined such that

$$tan(\psi) = \frac{E_{0y}}{E_{0x}} \tag{2.33}$$

The Jones vector can then be written in terms of a single angle

$$\underline{J_\delta}(\psi) = \begin{bmatrix} cos(\psi) \\ sin(\psi)e^{j\delta} \end{bmatrix} \tag{2.34}$$

General states of linear polarization are represented as

$$\underline{J_0}(\psi) = \begin{bmatrix} cos(\psi) \\ sin(\psi) \end{bmatrix} \tag{2.35}$$

where $\psi$ is any angle in relation to the X axis. Circular polarization is represented as

$$RCP : \underline{J}_{\frac{\pi}{2}} = \frac{1}{\sqrt{2}} \begin{bmatrix} 1 \\ j \end{bmatrix} \tag{2.36}$$

$$LCP : \underline{J}_{-\frac{\pi}{2}} = \frac{1}{\sqrt{2}} \begin{bmatrix} 1 \\ -j \end{bmatrix} \tag{2.37}$$

#### 2.1.2.1 Optical Devices

Polarization can be naturally occurring, such as in the case of skylight, or it can be created by passing light through an optical device such as a linear polarizer or a quarter wave plate. Jones vectors are useful for describing the polarization state of an EM wave, while Jones matrices describe non-depolarizing optical devices and the transformation of pure incident polarization states through them.

A linear polarizer is a device that transmits linear polarization states for incident light beams that are aligned with their transmission axis (TA) of the polarizer [14]. For example, if horizontally polarized light is passed through a polarizer with a $TA = 90°$, all of the incident light will be

extinguished. In practice all of the light is not completely extinguished and there are often spectral differences to the response of polarizers.

Since linear polarizers block light that is orthogonal to the TA, it can be shown that the general equation for a linear polarizer is such that

$$\underline{J}_{in}(\psi + \frac{\pi}{2}) = \begin{pmatrix} cos(\psi + \frac{pi}{2}) \\ sin(\psi + \frac{pi}{2}) \end{pmatrix} = \begin{pmatrix} -sin(\psi) \\ cos(\psi) \end{pmatrix} \tag{2.38}$$

and

$$\underline{J}_{out} = \begin{pmatrix} 0 \\ 0 \end{pmatrix} \tag{2.39}$$

The general equation for Jones interaction with a linear polarizer is

$$P(\psi)\underline{J}_{in} = \underline{J}_{out} \tag{2.40}$$

$$\begin{pmatrix} a & b \\ c & d \end{pmatrix} \begin{pmatrix} -sin(\psi) \\ cos(\psi) \end{pmatrix} = \begin{pmatrix} 0 \\ 0 \end{pmatrix} \tag{2.41}$$

$$-asin(\psi) + bcos(\psi) = 0 \rightarrow atan(\psi) \tag{2.42}$$
$$-csin(\psi) = dcos(\psi) = 0 \rightarrow ctan(\psi) \tag{2.43}$$

When the incident polarization state is aligned with the polarizers TA, it must also be true that the incident beam goes through the device unchanged. Therefore,

$$\underline{J}_{in}(\psi) = \begin{pmatrix} cos(\psi) \\ sin(\psi) \end{pmatrix} \tag{2.44}$$
$$\underline{J}_{out}(\psi) = \begin{pmatrix} cos(\psi) \\ sin(\psi) \end{pmatrix} \tag{2.45}$$

$$acos(\psi) + bsin(\psi) = cos(\psi) \tag{2.46}$$
$$ccos(\psi) + dsin(\psi) = sin(\psi) \tag{2.47}$$

substituting in for previous values of b and d give

$$a = \frac{cos(\psi)}{cos(\psi) + tan(\psi)sin(\psi)} = cos^2\psi \tag{2.48}$$

$$b = atan(\psi) = sin(\psi)cos(\psi) \tag{2.49}$$

```
>>> from noobee.jones import j, lp
>>> j_in = j(1,0)
>>> lp_1 = lp(0)
>>> lp_1 * j_in
matrix([[ 1.],
        [ 0.]])
```

Figure 2.4: noobee code for Jones Vectors

$$c = \frac{sin(\psi)}{cos(\psi) + tan(\psi)sin(\psi)} = sin(\psi)cos(\psi) \tag{2.50}$$

$$d = ctan(\psi) = sin^2\psi \tag{2.51}$$

The general form of a linear polarizer with transmission axis angle $\psi$ from the X axis is

$$P(\psi) = \begin{pmatrix} cos^2\psi & sin(\psi)cos(\psi) \\ sin(\psi)cos(\psi) & sin^2\psi \end{pmatrix} \tag{2.52}$$

The intensity of light emerging from a polarizer is governed by Malus law,

$$I = I_0 cos^2(\theta_i) \tag{2.53}$$

where $I$ is the intensity of the exiting beam, $I_0$ is the intensity of the incident beam and $\theta_i$ is the angle between the incident polarization state, and the angle of the polarizer. For incident unpolarized light the equation becomes $I/I_0 = \frac{1}{2}$. Therefore, the maximum transmittance for an unpolarized beam of light through a polarizer is 50

Wave plates create a phase delay between the fast and slow axis of incident linearly polarized light. Its generalized Jones matrix form can be denoted with a relative phase delay $\delta = \delta_y - \delta_x$,

$$C(\delta) = \begin{pmatrix} 1 & 0 \\ 0 & e^{-j\delta} \end{pmatrix} \tag{2.54}$$

Two common wave plates are the half wave plate and the quarter wave plate. These produce a delay of $\pi$ and $\pi/2$ respectively.

The noobelectric python package has a module for dealing with these types of problems and it automates Jones optical calculations for purely polarized light beams. An example for a linear polarizer combined with a quarter wave plate can be created and various input polarization states into the system as shown below.

### 2.1.3 Mueller Matrices

Interactions with materials that can create depolarization and model partially polarized input and outputs cannot be handled by Jones calculus. For these problems, Mueller Matrices are used to

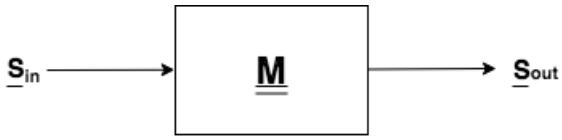


Figure 2.5: Stokes-Mueller System Diagram

model the polarization of light with varying degrees of polarization as it interacts with a material. These interactions are modeled with equation and shown in Figure 2.4.

$$\mathbf{S}_{out} = \mathbf{M}\mathbf{S}_{in} \tag{2.55}$$

When EM waves interact with optically active materials, their state of polarization may change. The characteristics of a material which changes the amplitude or phase of the $x$ or $y$ component for an incident EM wave, i.e. the polarization, is defined by its Mueller matrix. Mueller matrices determine how input Stokes' vectors change upon interaction with a material. They are defined as

$$\mathbf{M} = \begin{bmatrix} m_{00} & m_{01} & m_{02} & m_{03} \\ m_{10} & m_{11} & m_{12} & m_{13} \\ m_{20} & m_{21} & m_{22} & m_{23} \\ m_{30} & m_{31} & m_{32} & m_{33} \end{bmatrix} \tag{2.56}$$

and describe the diattenuation, depolarization, and retardance of a materials' polarization response to an input EM beam.

Diattenuation – the two attenuations of orthogonal polarization states [12]

Retardance – the phase difference between two orthogonal polarization states [15]

Depolarization – a process where polarized light becomes unpolarized [15]

It has been shown that these parameters can be found by determining a sample's corresponding Mueller Matrix. The scalar parameters are mathematically defined as,

$$\textbf{Diattenuation} = \frac{T_{max} - T_{min}}{T_{max} + T_{min}} \tag{2.57}$$

$$\textbf{Retardance} = \delta = \frac{2\pi(n_1 - n_2)t}{\lambda} \tag{2.58}$$

$$\textbf{Depolarization} = 1 - DOP \tag{2.59}$$

were $T_{max}$ and $T_{min}$ are the intensity transmittances through a polarizer, $n_1$, $n_2$ and $t$ are the refractive indices and thickness of a retarder [12].

For nondepolarizing materials, their MM can be converted into Jones matrices. Examples of Mueller Matrices for common optical elements can be found in [12]. The general form of a linear polarizer with transmission axis at 0 degrees to the $x$ axis is

$$\mathbf{M} = \begin{bmatrix} q+r & q-r & 0 & 0 \\ q-r & q+r & 0 & 0 \\ 0 & 0 & 2\sqrt{qr} & 0 \\ 0 & 0 & 0 & 2\sqrt{qr} \end{bmatrix} \tag{2.60}$$

where $q$ and $r$ are the attenuation coefficients for the $x$ and $y$ axis.

#### 2.1.3.1 Mueller Matrix Decomposition

The effects of diattenuation, depolarization and retardance can be found to be represented as subsets of the Muller matrix through its decomposition such that the result is

$$\mathbf{M} = m_{00} \begin{bmatrix} 1 & \mathbf{D}^T \\ \mathbf{P} & \mathbf{m} \end{bmatrix} \tag{2.61}$$

The derivation of the MM decomposition was made known by Lu and Chipman and is reproduced in [14]. $\mathbf{D}^T$ is the diattenutation vector that describes the amount of decrease in overall polarization for each set of orthogonal polarization states. The m matrix represents the retardance of a material.

$\mathbf{P}$ is the polarizance vector, and describes the amount of light that becomes polarized when unpolarized light is incident. It is analogous to the effect of depolarization. This vector can be measured by detecting the output Stokes vector of a material when unpolarized light is incident. This effect is only evident in materials that create polarization.

### 2.1.4 Reflection and Transmission

When light interacts with two materials that have different indexes of refraction, the incident beam is reflected and transmitted according to Fresnel's equations.

The law of reflection states

$$\theta_i = \theta_r \tag{2.62}$$

The transmission is derived directly from Snells equation,

$$n_1 sin(\theta_i) = n_2 sin(\theta_2) \tag{2.63}$$

Note that part of the transmitted spectra may be absorbed, although this is not considered in these equations.

Two main scenarios are often presented when demonstrating the principles which guide the reflected and transmitted rays; when the incident electromagnetic wave is polarized perpendicular to the plane of incidence, and when the wave is polarized parallel to it. The perpendicular po-

larized wave is often denoted S or TE for transverse electric, while the parallel scenario is often denoted P or TM for transverse magnetic.

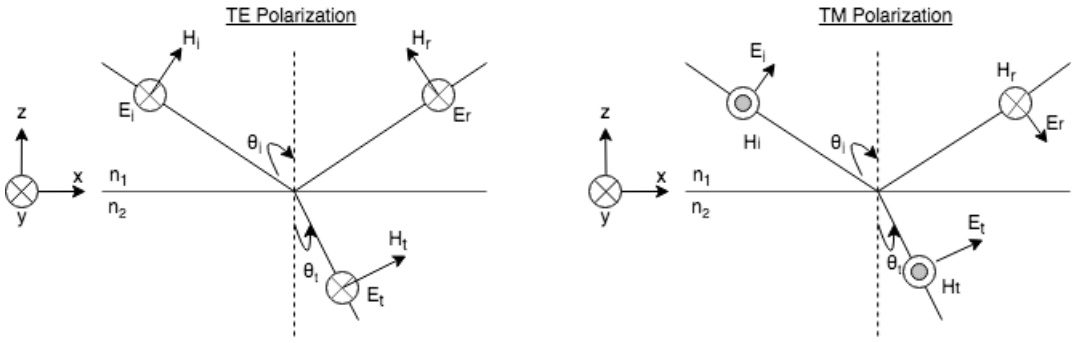


Figure 2.6: Fresnel Reflection and Transmittance

The intensity of the reflected waves for the S and P polarized case are

$$\mathbf{R_S} = |\frac{Z_2 cos(\theta_i) - Z_1 cos(\theta_t)}{Z_2 cos(\theta_i) + Z_1 cos(\theta_t)}|^2 \tag{2.64}$$

$$\mathbf{R_P} = |\frac{Z_2 cos(\theta_t) - Z_1 cos(\theta_i)}{Z_2 cos(\theta_t) + Z_1 cos(\theta_i)}|^2 \tag{2.65}$$

where Z is the wave impedance for medium 1 and 2. The power coefficients for transmission are then derived by following the law of conservation of energy such that,

$$T_S = 1 - R_S \tag{2.66}$$
$$T_P = 1 - R_P \tag{2.67}$$

The Brewster angle is a special case where the $P$ polarization state is completely transmitted and no reflection of the TM wave occurs. The reflected ray is therefore completely $S$ polarized since $R_P$ is zero and $R_S$ is a nonzero intensity. For perfect air glass interactions typically considered, this angle is approximately 55 degrees.

The Mueller matrix formulation for reflection and transmission reduces to the form of a linear polarizer for ideal surfaces. It has been shown in [14] that the equation for a reflected beam off of a perfectly smooth dielectric surface is

$$\begin{bmatrix} S_{0r} \\ S_{1r} \\ S_{2r} \\ S_{3r} \end{bmatrix} = \frac{1}{2}(\frac{tan(\theta_-)}{sin(\theta_+)})^2 \begin{bmatrix} p_S^2 + p_P^2 & p_S^2 - p_P^2 & 0 & 0 \\ p_S^2 - p_P^2 & p_S^2 + p_P^2 & 0 & 0 \\ 0 & 0 & 2p_S p_P & 0 \\ 0 & 0 & 0 & 2p_S p_P \end{bmatrix} \begin{bmatrix} S_0 \\ S_1 \\ S_2 \\ S_3 \end{bmatrix} \tag{2.68}$$

$$p_S = cos^2(\theta_-) \tag{2.69}$$
$$p_P = cos^2(\theta_+) \tag{2.70}$$

and $\theta_\pm = \theta_i \pm \theta_r$. This is identical to the form of a linear diattenuator or polarizer from Equation 2.60. For incident unpolarized light the equation simplifies to

$$\begin{bmatrix} S_{0r} \\ S_{1r} \\ S_{2r} \\ S_{3r} \end{bmatrix} = \frac{1}{2}(\frac{tan(\theta_-)}{sin(\theta_+)})^2 \begin{bmatrix} cos^2(\theta_-) + cos^2(\theta_+) \\ cos^2(\theta_-) - cos^2(\theta_+) \\ 0 \\ 0 \end{bmatrix} S_0 \tag{2.71}$$

Therefore, for ideal reflective surfaces, at the Brewster angle, light will be completely polarized perpendicular to the plane of incidence. It should be noted that the case of incident unpolarized light onto the target material, gives the polarizance vector of the Mueller Matrix as described in Section 2.1.3.

Imperfect, non-ideal surfaces have the ability to reflect, transmit and absorb incident electromagnetic radiation. The outcome of these interactions are related to the physiological makeup of the material, as well as its surface topology. Multiple scattering mechanisms can be at work within a system, and numerous models have been attempted to balance the tradeoffs between practical realizability for measurements and accurate representation of scattering mechanisms [16], [17]. Only some of these models attempt to deal with the polarization of the incident, reflected, and transmitted beams.

### 2.1.5 Scattering Mechanisms

Fresnel's equations provide an explanation for light reflected and transmitted for ideal surfaces. This is not the case with most man made and natural materials. Therefore, more complex mechanisms must be considered when dealing with real world radiation scattering problems. It has become popular in the field of remote sensing to denote the additional types of interactions as volume scattering and multiple scatter interaction. Single scattering mechanisms are those governed solely by Fresnel's equations. The combination of these scattering mechanisms create the diffuse and specular components of reflection.

Single scattering mechanisms create a portion of reflectance known as specular reflectance. They are often denoted as Type A photons in remote sensing models. These interactions are highly polarized perpendicular to the plane of incidence as previously discussed. For perfectly smooth dielectrics, this is the dominate scattering mechanism.

Volume scattering occurs when light is absorbed by a material and is readmitted in all directions, including back towards the surface of the material. They are denoted Type B photons. Transmittance of this energy back into the first medium obeys the laws of Fresnel's equations, although the indices of refraction are reversed. This mechanism accounts for absorption and other higher level light matter interactions, not explained solely by Fresnel's equations.

Multiple scattering occurs when either Type A or Type B photons interact with the material surface more than once when either being reflected or re transmitted out of the material. These are denoted Type C photons [18]. Figure 2.7 shows each type of interaction. In general type A

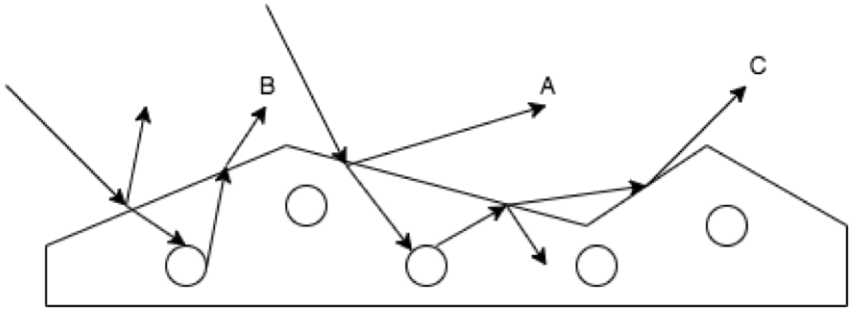


Figure 2.7: Various Types of Photon Interactions

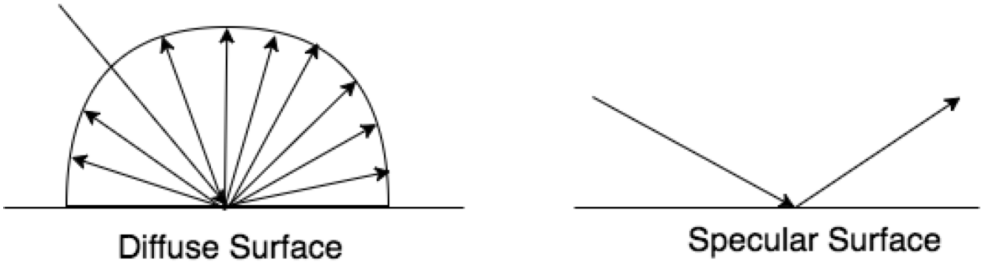


Figure 2.8: Diffuse and Specular Scattering

photons create specular highlights from surfaces that are smooth. Type B and C photons become more prevalent as a surface becomes rougher. In most real world applications, surfaces are neither purely specular or purely diffuse.

Surfaces that are perfectly smooth dielectrics are often considered to be purely specular reflectors of light. Incident energy is transmitted in an idealized single ray of light from the surface. Specular reflectors are single scattering mechanisms and result in purely polarized light due to the governance of Fresnel's equations and are denoted as type A photons. In simple models, rough surfaces can be viewed as purely diffuse reflectors that scatter incident light equally in all directions. Perfect diffuse surfaces are known as Lambertian surfaces. It has been assumed that the diffuse portion of light is unpolarized due to random nature of internal reflections [19], [20]. Bidirectional Reflectance Distribution Functions (BRDF) have been created to model the variety of surface interactions in order to handle the non ideal case of rough surfaces. BRDF defines how incident radiation is reflected off of opaque surfaces. It is defined as a ratio of reflected radiance along path $\omega_r$ to incident irradiance $\omega_i$. A simple depiction of this scenario can be found in Figure 2.9.

The BRDF function is often defined in the form

$$f_r(\omega_i, \omega_r) = \frac{dL_r(\omega_r)}{dE_i(\omega_i)} \tag{2.72}$$

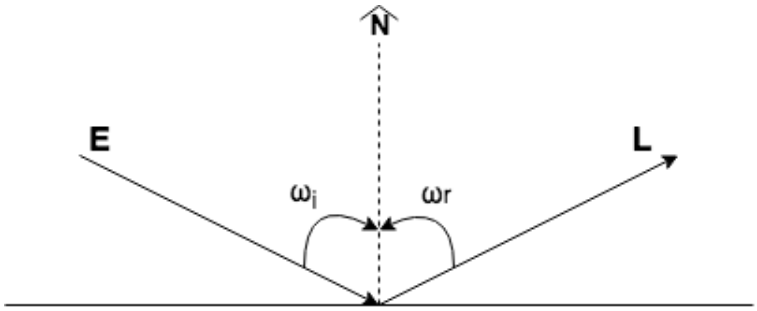


Figure 2.9: Simple BRDF Model

Each $\omega$ is a function of azimuth angle $\phi$ and zenith angle $\theta$. The input irradiance and output radiance are measured in units of steradians as shown in Figure 2.10. where numerous models have been developed for the functions of $L$ and $E$ [21][22]. In its simplest case the surface is a purely diffuse reflector of incident light and the BRDF becomes

$$f_r(\omega_i, \omega_r) = \frac{\rho}{\pi} \tag{2.73}$$

where $\rho$ is the surface albedo, or proportion of light reflected from a surface [23] and ranges from $0 \leq \rho \leq 1$. A general diagram can be found in Figure 2.9. In the most general case the portion of reflectance that is purely specular can be thought of as a $\delta$ function. Most surfaces create non-ideal reflections made up of both specular and diffuse components. The notion of a surface being rough, smooth, fine or coarse come with the connotation of touch and the feeling of a materials' surface. They are textures.

## 2.2 Texture and Tone

"When small image areas from black and white photographs are independently processed by a machine, then texture and tone are most important" [24]. Without tone there is no texture, as texture is created when there are certain frequencies of tonal change in an image [4].

A surface texture is classified according to the scale at which the human eye can see. It is import to determine the appropriate scale for a particular surface, when talking about its texture. A surfaces ability to appear smooth or rough in an image, is determined by the spatial frequency distribution of grey level pixel intensities in a greyscale image and the various shades of grey tones. The nature of light reflecting from surfaces of materials is also largely due to the how rough or smooth the surface is. Imaging devices are able to pick up pixel by pixel surface interactions in their large field of view. Cameras are able to detect multiple scattering mechanisms for analysis in material classification problems.

Tone is related to texture and is the grey level gradients distributed across an image. It is the "relative brightness or color of objects on an image" [4]. If an image has no differences in tone, then the texture and other features are indiscernible.

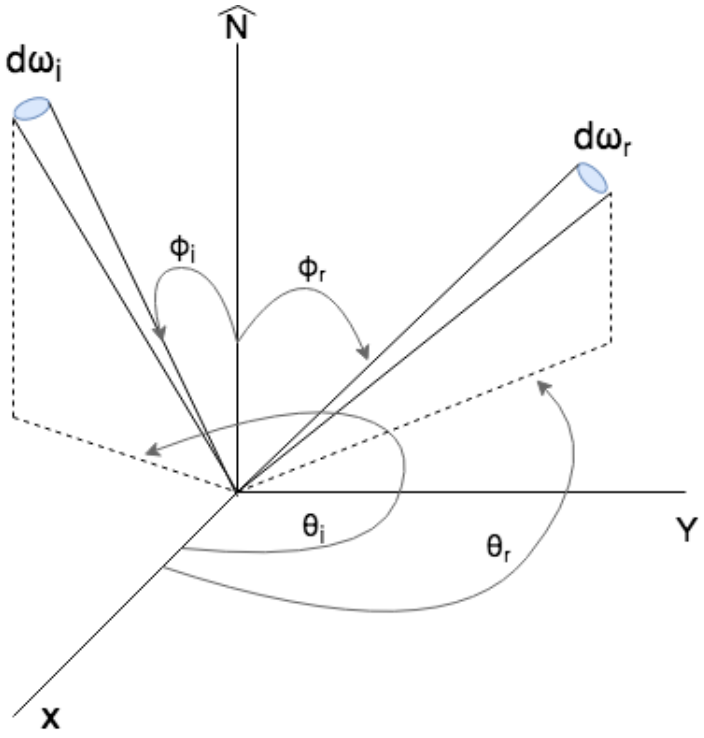


Figure 2.10: General BRDF Model

When a pixel is considered as a single color receptor, it represents only tone. The scaling of the window size to include more pixels allows for texture to become more prevalent. Scale is important when considering texture since texture is defined in relation to our perception of a materials' surface.

### 2.2.1 Grey Level Co-Occurence Matrix

A Grey Level Co-Occurrence Matrix (GLCM) is able to quantify the spatial frequency distribution of grey level pixel intensity pairs. The GLCM matrix is formed by determining the frequency of grey level value pixel pairs for a given image. A relationship is set a priori to determine the direction for grey level comparison. This relationship is an angle relating a pixel to its neighbor, and is chosen in multiples of either 0 or 45 degrees. Common GLCM spatial relationships are $0, \pi/4, 3\pi/4$, and $\pi/2$ radians. In order to quantify a texture in a rotationally consistent fash-

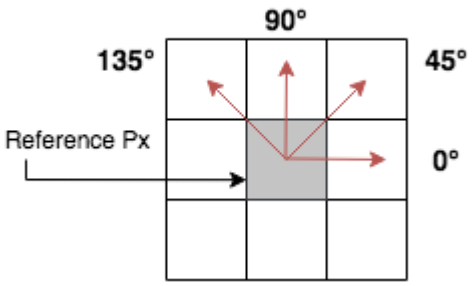


Figure 2.11: Defining GLCM Relationships

ion, all four relationships are usually calculated and averaged together in determining the overall GLCM matrix. The GLCM has a size of $NxN$ where $N$ is the discrete quantized levels.

A single relationship Co-Occurence matrix is formulated such that,

$$\phi_{ij}(\triangle x, \triangle y) = \sum_{x=0}^{n}\sum_{y=0}^{m}\begin{cases}1, if I(x,y) = i \quad \text{and} \quad I(x+\triangle x, y+\triangle y) = j \\ 0, otherwise\end{cases} \tag{2.74}$$

where $I(x, y)$ is an $nxm$ image and $\triangle x, \triangle y$ represent the predefined offset of the grey level pixel neighbor intensity relationship (i,j). Being defined as referencing one pixel to its neighbor to the right (0 degrees) the GLCM matrix is formulated as such, The example in Figure 2.12 shows the simplest case of a binary image, or an image that only contains white and black pixels. These pixels values captured by a camera are then converted into there corresponding digital numbers, in this case either zero or one. With the spatial relationship being defined as one to the right, the GLCM matrix is then formed.

Non symmetrical GLCMs should be symmetrized by adding each to its transpose,

$$\phi^{'} = \phi + \phi^{T} \tag{2.75}$$

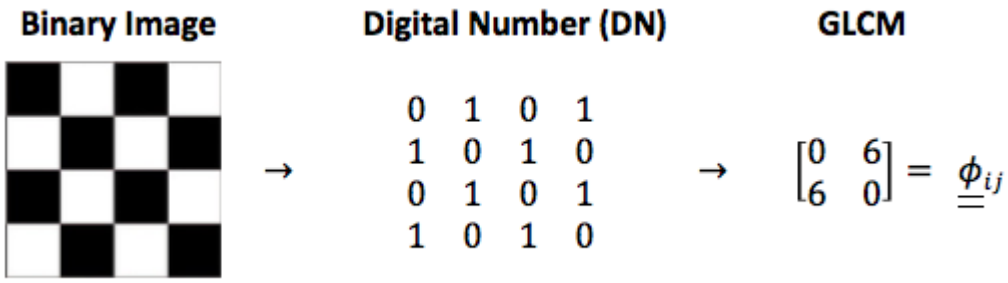


Figure 2.12: Converting a Binary Image to a GLCM Matrix

Normalizing the frequency to one by dividing the matrix by the sum of all its elements, results in a probability distribution for each grey level pixel pair.

$$\mathbf{P} = \frac{\phi'}{\sum_{i=0}^{N-1}\sum_{j=0}^{N-1}\phi'} \tag{2.76}$$

where for the example given above the resulting $\mathbf{P}$ is

$$\mathbf{P} = \frac{1}{12}\begin{bmatrix}0 & 6\\ 6 & 0\end{bmatrix} = \begin{bmatrix}0 & 0.5\\ 0.5 & 0\end{bmatrix} \tag{2.77}$$

As expected the probability of finding a 0 next to a 1 is the same as finding a 1 next to a zero in a binary checkerboard image.

Features can then be extracted from the formed matrix for the purpose of defining single quantitative values for texture. These features are known as Haralick features and generally fall into 3 distinct feature categories; Contrast, Statistical and measures of Orderliness [25].

Contrast measures are defined by weights that increase or decrease with distance from the GLCM diagonal. These weights can be linear, exponential, etc. For the N x N dimensional GLCM matrix the N - 1 term in the first row or column represents pixel relationships that are of the greatest intensity difference.

For example, an 8-bit image has 256 possible grey level values ranging from 0-255, so the maximum amount of contrast occurs when pixel pairs (i,j) are either (0, 255) or (255, 0).

Contrast has weights that increase exponentially away from the diagonal. It is calculated as

$$Contrast = \sum_{i=0}^{N-1}\sum_{j=0}^{N-1}(i-j)^2 P_{ij} \tag{2.78}$$

The dissimilarity is a measure of contrast with weights that increase linearly away from the diagonal

$$Diss = \sum_{i=0}^{N-1} \sum_{j=0}^{N-1} |i-j| P_{ij} \tag{2.79}$$

The dissimilarity of the example binary image can be calculated as

$$Diss = \sum_{i=0}^{N-1} \sum_{j=0}^{N-1} |i-j| P_{ij} = \sum_{1=0}^{1} |i| P_{i0} + |i-1| P_{i1} = 0 + P_{01} + 0 + P_{10} = \frac{1}{3} \tag{2.80}$$

Statistical measures utilize each individual element of the GLCM as weights to determine the moments of the probability distribution matrix. The mean, variance, correlation, etc. are not measures of individual pixel intensity values, but rather of the intensity of a pixel in relation to its neighbor's intensity. The mean is the first central moment and is defined by

$$\mu_i = \sum_{i=0}^{N-1} \sum_{j=0}^{N-1} i P_{ij} \tag{2.81}$$

$$\mu_j = \sum_{i=0}^{N-1} \sum_{j=0}^{N-1} j P_{ij} \tag{2.82}$$

Variance is the second moment of the GLCM and is defined as,

$$\sigma_i = \sum_{i=0}^{N-1} \sum_{j=0}^{N-1} (i-\mu_i)^2 P_{ij} \tag{2.83}$$

$$\sigma_j = \sum_{i=0}^{N-1} \sum_{j=0}^{N-1} (j-\mu_j)^2 P_{ij} \tag{2.84}$$

The correlation shows the "linear dependency of grey level values in the Co-Occurence matrix"[26]. It is computed from the values of the variance and mean such that

$$Corr = \sum_{i=0}^{N-1} \sum_{j=0}^{N-1} \left(\frac{(i-\mu_i)(j-\mu_j)}{\sqrt{\sigma_i^2 \sigma_j^2}}\right) \tag{2.85}$$

If a the GLCM is symmetric, the x and y means and variances are equal and the equations simplify to,

$$\mu = \sum_{i=0}^{N-1} \sum_{j=0}^{N-1} i P_{ij} \tag{2.86}$$

$$\sigma = \sum_{i=0}^{N-1} \sum_{j=0}^{N-1} (i-\mu)^2 P_{ij} \tag{2.87}$$

$$Corr = \sum_{i=0}^{N-1} \sum_{j=0}^{N-1} (\frac{(i-\mu)(j-\mu)}{\sigma^2}) \tag{2.88}$$

Measures of orderliness are quantified by the amount of entropy and energy within an image. Entropy is a measure of randomness in a system. In thermodynamics, it is the heat lost when a reaction occurs and hence is a measure of disorder. Energy is a measure of useful work that can occur due to the non random nature of the energy in a system. (clean up this bit on entropy)

The angular second moment (ASM) describes the amount of "inertia" around a pixel neighbor relationship and is defined as,

$$ASM = \sum_{i=0}^{N-1} \sum_{j=0}^{N-1} P_{ij}^2 \tag{2.89}$$

The square root of the ASM results in the energy of the system

$$Energy = \sqrt{ASM} \tag{2.90}$$

For perfectly uniform textures the energy will be at a maximum of 1.

## 2.3 Plant Physiology

A plant's health is greatly determined by the availability of light, water, and key nutrients in the soil. These elements are the fundamental inputs to photosynthesis, the process plants utilize to turn light energy into chemical energy for growth. Nitrogen, Potassium, and Phosphorus are fertilizers (agricultural inputs) that can incur large costs when applied over hectares of farmland, but are needed for healthy plant growth and cell reproduction.

Water is also an essential agricultural input needed for plant photosynthesis and aids in nutrient transport. Droughts are becoming a global epidemic and precision water management is becoming pivotal for a crops' survival.

The layers of a deciduous leaf contain protection mechanisms, transport systems, and reaction centers for the process of photosynthesis. The cuticle wax layer, upper epidermis, and mesophyll layer are the first layers of light interaction on the adaxial surface of the leaf.

The cuticle wax layer provides "the most critical adaptive trait for survival … the ability to retain water in increasingly dehydrating habitats" [27]. It is the first line of defense for plants and acts as a barrier between water transpiration.

The mesophyll layers contain chloroplasts that convert light energy into chemical energy and consists of two parts. The palisade mesophyll is made up of elongated, organized, compact cells that contain a large number of the chloroplasts. The spongy mesophyll is irregular in shape and has a large amount of space between its cells to facilitate air and gas exchange [28].

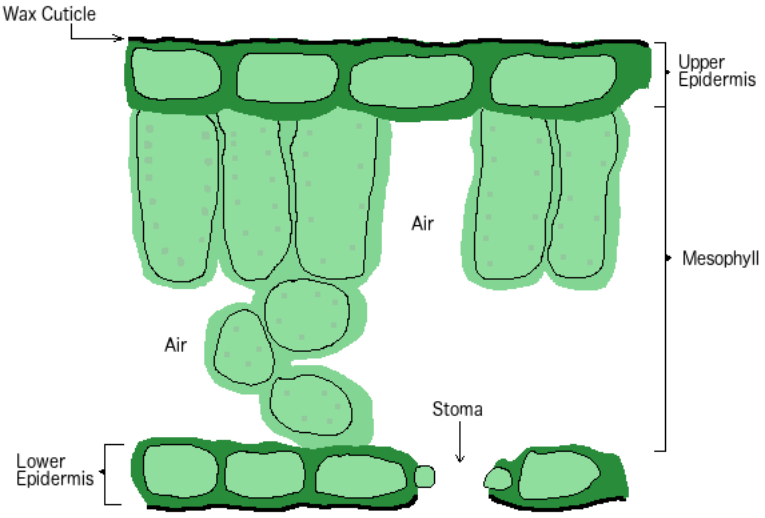


Figure 2.13: Major Structures of a Leaf

The upper epidermis consists of very few chloroplasts, and allows most of the light to pass through to the mesophyll layers.

### 2.3.1 Photosynthesis

Photosynthesis is a fundamental process that dictates the growth of all land plants. Water plays an important role in this chemical process, and its availability in plant leaves is an indicator of the plant's ability to perform photosynthesis.

The chemical reaction undergone during photosynthesis involves the conversion of carbon dioxide and water with light energy, to create a carbohydrate and oxygen. It is formally written as,

$$6CO_2 + 6H_2O \xrightarrow{\text{light}} C_6H_12O_6 + 6O_2 \tag{2.91}$$

Due to water's integral role in this reaction, water stress in plants can lead to decreased photosynthetic activity. It was pointed out by Ehleringer, referenced in [29], that water stress "can decrease…photosynthesis by reflecting quanta that might have been used in photosynthesis". Chlorophyll is an essential pigment in photosynthesis due to it being "an efficient light-absorbing molecule" [11]. It is highly absorbing in the blue and red spectrum of visible light, and more reflective in the green portion. The absorption spectrum for chlorophyll can be found in [30]. This spectrum is what causes many leaves to be green. Note that is regions outside the visible, chlorophyll does not absorb the incident radiation.

### 2.3.2 Relative Water Content

The Relative Water Content (RWC) of a leaf is a measure of the current water level based on the total leaf water retaining capacity. It is a useful measure of the water balance within a plant as it expresses the absolute amount of current water in a plant, in proportion to the minimum amount of water it can hold.

Water makes up over 90% of the mass of a leaf, and although RWC provides a good indicator of plant health and water capacity, it is highly dependent on the age and maturity of the leaf. It should also be taken into consideration that leaves can also be very heterogeneous and contain a variety of complex structures in different stages of growth, within each individual leaf.

Correlations between the RWC and other physiological responses have been found in [11].

| Relative Water Content (%) | Plant Physiological Response |
|---|---|
| 90-100 | closing of the stomata, reduction of cellular expansion and growth |
| 80-90 | tissue composition change, altered rates of photosynthesis and respiration |
| <80 | ceasing of photosynthesis |

Table 2.1: Plant physiological responses to detected relative water content levels.

"An increase in reflectance…is not directly related to water content but indirectly, since a decrease in water content can lead to an increase in internal lead air space or cell breakdown which may increase reflectance and decrease transmittance [31]".

This increase in internal air space leads to multiple scattering at air wax boundaries, and creates differences in the reflection and transmission of light, absorption, and the $S1$ and $S2$ Stokes parameters of the polarization response.

Field measurements of the physiological properties of plants are time consuming and error prone. It is therefore beneficial to pursue solutions to quantifying these metrics in large area field measurements.

## 2.4 Remote Sensing of Vegetation

### 2.4.1 Vegetation Indices and Spectral Responses

Spectral response patterns in remote sensing have been shown to useful [2][18][32] for determining the health of land vegetation. The reflection and scattering of light off vegetation using different spectral bands of incident light, allows for the classification of land objects and vegetation health. The detector response to these processes are known as spectral responses. Spectral responses are quantitative measures that change with the condition of the vegetation under inspection. As plants become stressed, as in the case of water deficiency or drought, their physiological makeup changes. A variety of different factors can affect the exact spectral response of an object [4].

Vegetative Indices (VI) are ratios between different spectral responses for the purpose of determining the condition and health of plants. Various combinations of frequencies have been

combined to form standard VI's utilizing the visible spectrum and the infrared spectrum. In its most basic form a vegetation index is defined by,

$$VI = Ch1 - Ch2 \tag{2.92}$$

where Ch1 and Ch2 are the channels of the detected spectral responses.

The Normalized Difference Vegetation Index (NDVI) utilizes a plant's response to Near Infrared and Visible Red energy. This is a measure of the chlorophyll content within the leaves since the leaf is highly reflective and transmissive in the NIR since plants cannot use light outside of the visible spectrum for photosynthesis. This band represents the amount of cellulose contained within the plant. The red light is used by chlorophyll for photosynthesis. It also interacts with the cell wall and is therefore a measure of both chlorophyll content and cellulose. The difference between these two spectral responses is the NDVI.

$$NDVI = \frac{NIR - VIS_{red}}{NIR + VIS_{red}} \tag{2.93}$$

In comparison, clouds, snow, and water all have relatively high visible responses and low NIR response. Therefore, little interference from these effects is contributed to the overall NDVI. Moreover, most satellites average NDVI recordings over a few days to also alleviate any interference with clouds and other particles in the atmosphere [4]. The NDVI takes advantage of the extreme shift in reflectance and transmittance for plants between the visible and near infrared regions known as the red gap shown in [33].

The reflectance curve for a plant leaf versus wavelength, shows that green light ( 500-600nm) is the most reflected wavelength of light, and accounts for the green color of leaves. Red is ( 600-750nm) and and blue light ( 400-500nm) are shown to be highly absorbed. This is due to these frequencies being used in photosynthesis and the high absorption of chlorophyll in these regions.

It should also be noted that as leaves dry down and become brown in color, the reflectance curve in the red part of the spectrum greatly increases [photon vegetation]. The magnitude of this change is dependent on the species of plant, as well as the maturity of the individual leaf structures.

There are also metrics that utilize the visible spectrum such as the Visible Atmospherically Resistant Index (VARI) [32]. It is defined as

$$VARI = \frac{VIS_{green} - VIS_{red}}{VIS_{green} + VIS_{red} - VIS_{blue}} \tag{2.94}$$

The vegetation indices described, all indirectly describe the amount of photosynthetic activity occurring within the plant. They are sensitive to the local growing conditions, growth stage of plants, and other factors. The major spectral responses of pigments within plants have been studied in vivo in order to gain insight into how light is utilized on a metabolic level by plants, in the process of photosynthesis.

### 2.4.2 Reflection and Transmission of Light and Leaves

The reflectance of light off of a leaf is dependent on many different factors. As plants undergo stressful conditions, their reflectance and transmittances change. In general, as photosynthetic activity decreases, the reflection off the surface increases. As a result there is also less transmission. The growth stage of the leaf is also important as younger leaves have not fully developed all of the internal complex structures. As the number of complex structures increases, there is an increase in the number of air wax interfaces to cause more randomized reflection and refraction [31].

Leaves that succumb to disease also may become deformed and further alter the response recorded from the canopy layer.

It has been shown [20], [34] that leaves are not purely diffuse or purely specular reflectors of light. Their response is best modeled as a combination of both components.

### 2.4.3 Polarization of Light from Leaves

An increase in the reflectance of light off the surface of a leaf, as it reflects wavelengths it would normally use for photosynthesis, allows for the polarization response of the leaf to be observed. As stated in [31] "Polarization provides the capability to separate light scattered by the leaf mesophyll from light scattered by the air-cuticle surface". Specular reflections, that occur at the Brewster angle provide information on the topology of leaf surfaces. Leaves are not optically smooth and therefore the typical application of Fresnel's equations for reflection and transmission must be extended to handle rough surfaces. BRDF models have been extended to include the polarization of light matter interactions on the on incident irradiance. These models are known as polarimetric Bi-directional Distribution Function (pBRDF). A pBRDF model adapted for leaf surfaces can be found in [31].

The specular component is sometimes so bright that it can make an entire canopy appear white to the observer. This portion is usually highly polarized and tells of the surface topology of the leaves [33]. The diffuse component is often assumed to be randomly polarized, although our results show there is potential to discriminate with diffuse polarization.

### 2.4.4 Classification of Vegetation Species

In addition to determining the relative health of vegetation, remote sensing can be useful to classify fields' and canopies' heterogeneous combination of species. The spectral characteristics of each pixel in an acquired image can be combined into similar groups for classification and is known as spectral pattern recognition.

Pixel relationships that represent texture, feature size, etc. can also be used for classification and is known as spatial pattern recognition. This method is often computationally more intensive than its spectral counterpart, as additional calculations need to be performed in order to extract this information.

A hybrid approach can also be used, which combines both spectral and spatial response patterns for the purpose of classifying image scenes.

Challenges to this include the variation of vegetation with different seasons, health status and growth stage.

# 3 Experimental Design

""I have not failed. I've just found 10,000 ways that won't work".

*Thomas Edison*

In order to demonstrate the effectiveness of polarization and texture features with support vector machines for the purpose of classification and relative water content determination, experiments were designed, conducted and analyzed. These experiments was designed to investigate the linear polarizance vector of the Mueller matrix for various species of tree leaves in the diffuse and specular directions. Leaves were investigated in different physiological states determined by both decomposition time and relative water content. Classification and regression techniques were used to correlate the polarization and texture information from images acquired of various species of leaves. Data for Red Oak, American Ash and Sugar Maple leaves was acquired for the purpose of classification. Devils Ivy was observed in studies on relative water content.

Specular reflections are well known to create highly polarized light [20],[33]. The diffuse portion of reflection has been less investigated. It has often been assumed that the diffuse portion is unpolarized due to multiple scattering and volume scattering caused by type B and C photons creating random orientations of light. Recently the polarization of the diffuse component has been observed in studies [35], [36] for the purpose of determining the geometry of various surfaces. In the experiments reported here, the diffuse portion was observed for indicators of physiological, chemical, and biological status for individual plant leaves. It was assumed that as the leaf surfaces decomposes or losses water content, the surface would become rougher as the epicuticle wax layer changed. The experiments presented here, attempt to demonstrate results that agree with previous outlined light leaf interactions in the specular direction, as well as extend the analysis for the diffuse direction. The acquired polarization and texture data is processed for the purpose of determining the surface texture and internal scattering mechanisms for classification between various species, and investigation into the differences in these processes during decomposition and water stress conditions.

There are numerous challenges to practical applications of BRDF models due to the large amount of measurements required to classify an object's reflective polarization properties. A digital microscope was utilized for the purpose of quantifying regions on leaves that include different surface structures such as veins, mold, undulations, cell walls, etc.

The polarizance of a material represents the first column of its Mueller Matrix, and determines the amount of polarization that results from unpolarized incident light. These elements represent the linear polarization that results from the light material interactions, and can be useful for characterizing a material. The polarizance can easily be acquired using simple light measuring Polarimetry techniques, when the incident light is unpolarized. The measurements required to determine this vector is severely reduced when compared to other measurement techniques.

All measurements were performed using light incident at approximately the Brewster angle of 55 degrees. This is the Brewster angle calculated between air $n = 1.0$ and glass $n = 1.5$. The index of refraction for leaves is estimated to be between 1.3 and 1.6. Specular observations were observed at 55 degrees from the normal to the plane of incidence. The diffuse measurements were taken at 0 degrees from the normal.

The Brewster angle was chosen since it represents the angle where light reflected from an ideal specular surface would be highly polarized. In the natural environment leaves are in various orientations to the normal surface of a plant canopy. It is typical to extend the results from micro level leaf studies to canopies by creating probability distribution models that can predict the various leaf orientations. Combining the results from individual leaf studies with probability models should provide more accurate information for interpreting plant image data. The experimental setups for the specular and diffuse components can be found in Figure 3.1 and Figure 3.2. Using

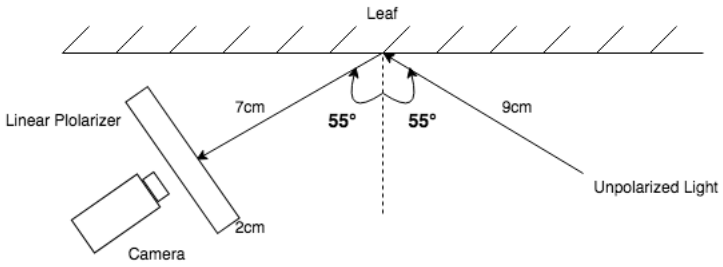


Figure 3.1: Specular Experimental Setup

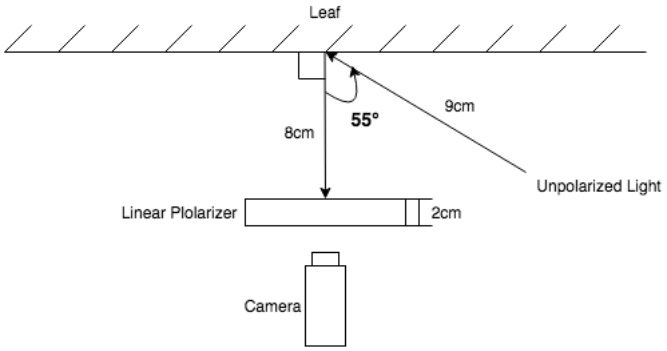


Figure 3.2: Diffuse Experimental Setup

measurements acquired through a linear polarizer, the polarizance of each sample was calculated and plotted as a histogram. The measurements were acquired using a digital microscope which produced images for each orientation of the polarizing filter. These images were additionally processed for texture feature extraction using GLCM techniques.

Each color image was split into its individual color channel to apply greyscale imaging techniques for pseudo-spectral analysis.

Extracted features were observed and utilized for the purpose of classification among species, and determining the relative water content of individual leaves using regression analysis. For each type of experiment the same orientation of polarizer and camera was used to capture images in the diffuse and specular directions.

# 4 Data Acquisition

> "I went to the woods because I wished to live deliberately, to front only the essential facts of life, and see if I could not learn what it had to teach, and not, when I came to die, discover that I had not lived".
>
> *Walden. Henry David Thoreau*

Images were acquired using a digital microscope through various polarization filter arrangements to determine each materials polarization and texture properties. A broadband white light source was utilized to illuminate the target under investigation. The DOP of the light source was found to be low of 0.02 percent. The lights within the room were turned off during data acquisition to reduce the amount of ambient light noise. In real world applications any ambient light should be accounted for using radiometric calibration techniques, or other correction methods. A custom web application was created to capture, label and store images for easy access and processing. The acquired data and processing code can be found in [37].

## 4.1 Measurement of Stokes Parameters

The Stokes parameters for a beam of light can be determined by measuring the flux values of orthogonal polarization states. A variety of optical setups can be required to measure all of the Stokes parameters. A Classical polarimeter is one that utilizes a rotating quarter wave plate in front of a linear polarizer to sample a sine wave from the intensities recorded by a detector. A Fourier analysis is then performed on this signal to determine all of the Stokes parameters.

It is shown in [12] that the Stokes parameter of a beam can be generally calculated as

$$\mathbf{S} = \begin{bmatrix} S_0 \\ S_1 \\ S_2 \\ S_3 \end{bmatrix} = S_0 \begin{bmatrix} P_H + P_V \\ P_H - P_V \\ P_P - P_M \\ P_R - P_L \end{bmatrix} \tag{4.1}$$

where $P_H, P_V, P_P, P_M, P_R$ and $P_L$ represent flux measurements recorded through filters that extinguish orthogonal polarization states.

For most natural and man made objects the reflections are assumed to contain little or no circular polarization. The last row of the Stokes vector is therefore left out of the discussion and the equation becomes

$$\mathbf{S} = \begin{bmatrix} S_0 \\ S_1 \\ S_2 \end{bmatrix} = S_0 \begin{bmatrix} P_H + P_V \\ P_H - P_V \\ P_P - P_M \end{bmatrix} \tag{4.2}$$

The linear elements of the Stokes vector can be determined using just a linear polarizer and rotating the polarizer to 0, 45 90 and 135 degrees. These measurements are denoted $P_H$, $P_P$, $P_V$, and $P_M$. They are the captured time average intensities for the $S$ and $P$ components of the electric field previously described. The linear polarizer was calibrated using a polarizer of known axis orientation. The calibration polarizer was kept with its axis constant to the S plane of the material. The lens of the measurement polarizer was rotated until a null intensity was reached and the axis of transmission for the polarizer was orthogonal to that of the calibration polarizer. The polarizer has a known extinction ratio of 19 and a polarization of 95

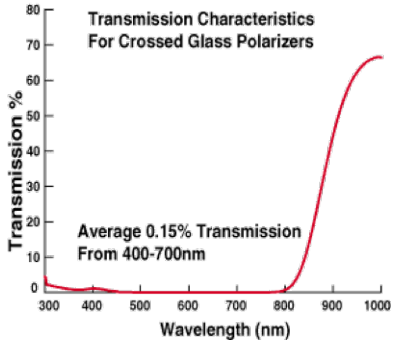


Figure 4.1: Polarizer Characteristic from Edmund Optics

When unpolarized light is incident, the Stokes vector for the exiting beam is identical to the polarizance of the Mueller matrix for the material and can be useful for classification of materials.

The intensity measurement is recorded with a detector.

## 4.2 Single and Multi-Pixel Detectors

For centuries the only photo detector available to those in the field of optics was the human eye. Many methods were only capable of producing measurements via a null intensity method, where light was extinguished to determine orthogonality between polarization and polarizer transmission axes. Modern single pixel photo detectors allow for the capturing of intensity or tone. There are numerous types of detectors available made with different materials that exhibit different properties when interacting with light. Silicon is a common substrate.

A single pixel is not enough to capture texture. Multiple measurements need to be made using a single pixel in order to quantify a region of space around the surface, denoted by the units of

steradians in the BRDF models. Multi-pixel detectors with a larger field of view allow for multiple features and texture to be captured in an image.

A camera is made up of a pattern of multiple silicon photo detectors and filters. The most common filter arrangement is that of a Bayer filter. This pattern consists of red, green, and blue spectral filters arranged as shown in Figure 4.2. The individual intensities from each of these filters

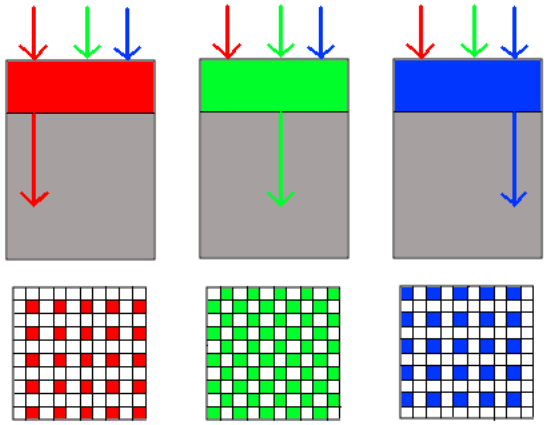

Figure 4.2: Bayer Filter Pattern

are combined with the camera to create a 3 channel RGB representation of the image scene. Each channel represents the intensity of a given pixel for the color filter in the Bayer pattern.

Single and multi-pixel devices have been utilized in Polarimetry for different applications. A camera was utilized for these experiments as it provides information on texture, as well as an ability to distinguish features in each of the spectral color channels.

The intensity values for each RGB channel of an image can easily be extracted using the OpenCV python package. Note that OpenCV actually holds images in reverse order as BGR.

OpenCV, a popular image processing library in Python, stores images as intensities in a multidimensional array representing the blue, green, and red response patterns. It is possible to separate these channels and access the discrete intensity values to perform a pseudo-spectral analysis.

## 4.3 Determining Relative Water Content

The steps for determining the RWC involve weighing the leaf in its current water state, artificially hydrating the leaf to its maximum capacity and completely drying out the leaf. The procedure for obtaining the measurements necessary for obtaining the RWC are as follows [11],[38]],

1. Remove leaf from host plant leaving approximately 2 cm of petiole
2. Weigh leaf to acquire the Fresh Leaf Weight (FW)
3. Place leaf petiole in solution of distilled water and CaCl2 at 2mM for at least 8 hours

4. Weigh leaf to acquire Turgid Weight (TW)
5. Place leaf in an oven at 60oC for 4 days
6. Weigh leaf to acquire the Dry Weight (DW)

The relative water content can then be calculated as a percentage,

$$RWC = \frac{FW - DW}{TW - DW} x100 \tag{4.3}$$

Note that the scale used for weighing needs to have at least 4 decimal places to ensure the accuracy of the measurements. Drying times and artificial hydration times can vary with species and oven temperature. An example of measurements can be found in Table 4.1. All acquired RWC data can be found in the Appendix.

| Leaf | TFW | TW | DW | RWC |
|---|---|---|---|---|
| 11 | 2.7931 | 2.8335 | 0.2472 | 98.4379 |
| 12 | 2.0883 | 2.1184 | 0.1876 | 98.4411 |
| 21 | 1.7804 | 1.8051 | 0.1376 | 98.5187 |
| 22 | 1.7655 | 1.8022 | 0.1404 | 97.7916 |
| 31 | 2.1874 | 2.2359 | 0.1656 | 97.6573 |
| 32 | 2.2511 | 2.3108 | 0.1687 | 97.2130 |
| 1_1 | 1.3687 | 1.3807 | 0.0826 | 99.0756 |
| 1_2 | 1.6860 | 1.7015 | 0.1024 | 99.0307 |
| 2_1 | 1.4904 | 1.4904 | 0.1029 | 97.0378 |
| 2_2 | 2.2324 | 2.2690 | 0.2003 | 98.2308 |
| 3_1 | 1.2877 | 1.3003 | 0.1070 | 98.9441 |
| 3_2 | 1.7654 | 1.7825 | 0.1330 | 98.9633 |
| 1+1 | 2.1297 | 2.1586 | 0.1667 | 98.5491 |
| 1+2 | 1.5341 | 1.5699 | 0.0973 | 97.5689 |
| 2+1 | 1.1938 | 1.3323 | 0.0867 | 88.8809 |
| 2+2 | 2.2729 | 2.4420 | 0.2165 | 92.4017 |
| 3+1 | 1.5755 | 1.6441 | 0.1314 | 95.4651 |
| 3+2 | 2.3954 | 2.4486 | 0.2114 | 97.6220 |
| 3&1 | 1.6107 | 1.6478 | 0.1380 | 98.4379 |
| 3&2 | 2.3541 | 2.4297 | 0.1987 | 98.4411 |
| 3&3 | 1.6821 | 1.7432 | 0.1758 | 98.5187 |
| 3&4 | 2.0762 | 2.1322 | 0.2168 | 97.7916 |
| 3&5 | 1.1001 | 1.1153 | 0.0823 | 97.6573 |
| 3&6 | 2.0207 | 2.2154 | 0.1737 | 97.2130 |
| 1.1 | 1.1294 | 1.1478 | 0.0702 | 98.2925 |
| 1.2 | 1.0425 | 1.0525 | 0.0631 | 98.9893 |
| 2.1 | 1.2669 | 1.2905 | 0.0987 | 98.0198 |
| 2.2 | 1.0833 | 1.0961 | 0.0769 | 98.7441 |
| 3.1 | 1.0311 | 1.0377 | 0.0872 | 99.3056 |
| 3.2 | 1.2738 | 1.2820 | 0.1097 | 99.3005 |
| 3^1 | 1.1240 | 1.1462 | 0.0959 | 97.8863 |
| 3^2 | 1.5232 | 1.5917 | 0.1597 | 95.2165 |
| 3^3 | 1.4585 | 1.4826 | 0.1218 | 98.2290 |
| 3^4 | 1.0184 | 1.0504 | 0.0822 | 96.6949 |
| 3^5 | 1.3605 | 1.3605 | 0.0967 | 97.6974 |
| 3^6 | 1.2660 | 1.2660 | 0.0935 | 97.9446 |

Table 4.1: Measurements for RWC Experiment

# 5 Feature Extraction

"Movement amongst the trees of a forest shows that the enemy is advancing. The appearance of a number of screens in the midst of this grass means that the enemy wants to make us suspicious".

*The Art of War, Sun Tzu*

After acquiring the necessary images for calculation of a leafs' polarizance, features were extracted from the images in each color channel for texture and polarization analysis. These features were extracted using various Python programming modules. 100 samples were extracted from each image to randomly create a training and testing set of data. Diffuse and specular datasets were processed separately.

In order to create testing and training data, samples were extracted from each polarization image $H$, $V$, $P$ and $M$ using code found in Figure 5.1. Each sample was extracted into three different color channels; red, green and blue.

This type of function mentioned in Figure 5.1 can be used to extract sample patches from all three (BGR) color channels. Features can then be extracted from each of the color samples. An example grey level histogram and image for each individual color channel through an H polarization filter can be found in Figure 5.2, 5.3 and 5.4. The corresponding V filter channels are found in Figure 5.5, 5.6 and 5.7 for a 75x75 pixel sample of Devils Ivy. Each of the samples were processed using pixel based analysis, to calculate their Stokes vector as well as various GLCM metrics. Pixels that were never illuminated were filtered out of the polarization analysis since they artificially inflated the zero mean of the produced histograms. Polarization is not the same as light intensity and polarization can not be determined without some illumination on the target. The Stokes vector was therefore calculated the code in Figure 5.8 where P1 and P2 represent orthogonal flux measurements through a linear polarizer. These values were binned into histograms in order to reduce the dimensionality and storage requirements for the data. These histograms were plotted using the following code in Figure 5.9. The resulting polarization histograms for a Devils Ivy sample can be found in Figure 5.10 for each corresponding BGR channel. A false image has also been included which shows the absolute value of the S1 polarization for each channel and location on the original image. The result of creating a false image out of the a polarization matrix, allows for a visualization for how polarization is resulting from specific surface and subsurface features. Window-based GLCM texture analysis was similarly performed on each of the extracted samples. The dissimilarity, correlation, contrast and entropy were calculated for each GLCM. The window size for GLCM was manually optimized by testing clustering effects for 5px, 9px, 25px, 55px, 75px, and 95px window sizes. A window size of 75 pixels was found to be ideal for this experimental design.

```
def extract_bgr_samples(filename, size, count):
    """
    Extract random samples from b, g, r image channels.

    Args:
        filename (str): Location to the image filename.
        size (int): The length/width of the square sample.
        count (int): The number of samples to generate.
    Returns:
        tuple: Random samples from each color channel.
    """
    img = cv2.imread(filename, 75, 1)
    samples = image.extract_patches_2d(img, (size, size), count, 1)
    cv2.imwrite('sample.png', samples[0])
    b, g, r = bgr_split(samples[0])

    return b, g, r
```

Figure 5.1: Extract samples from each BGR Image Channel Example Code

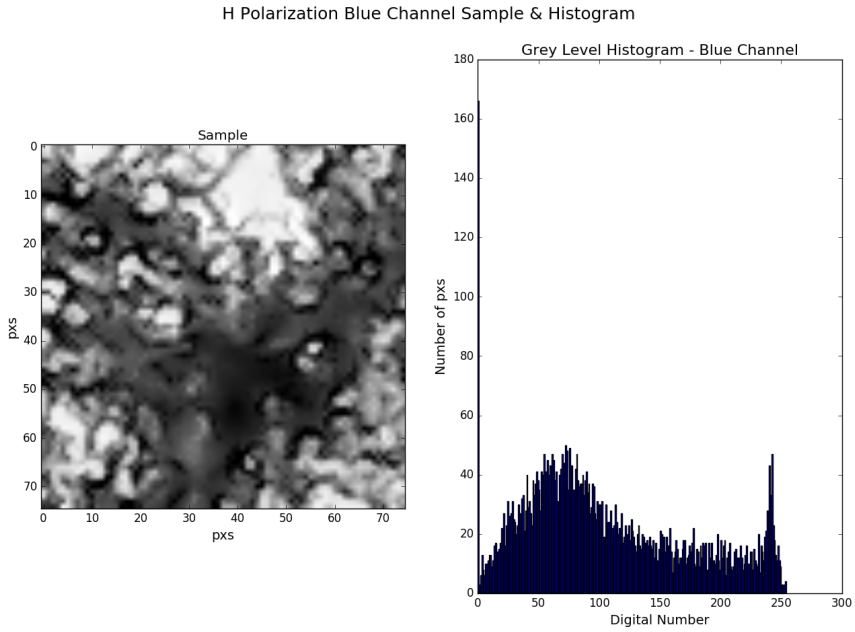


Figure 5.2: Devils Ivy Blue Channel H Filter Histogram

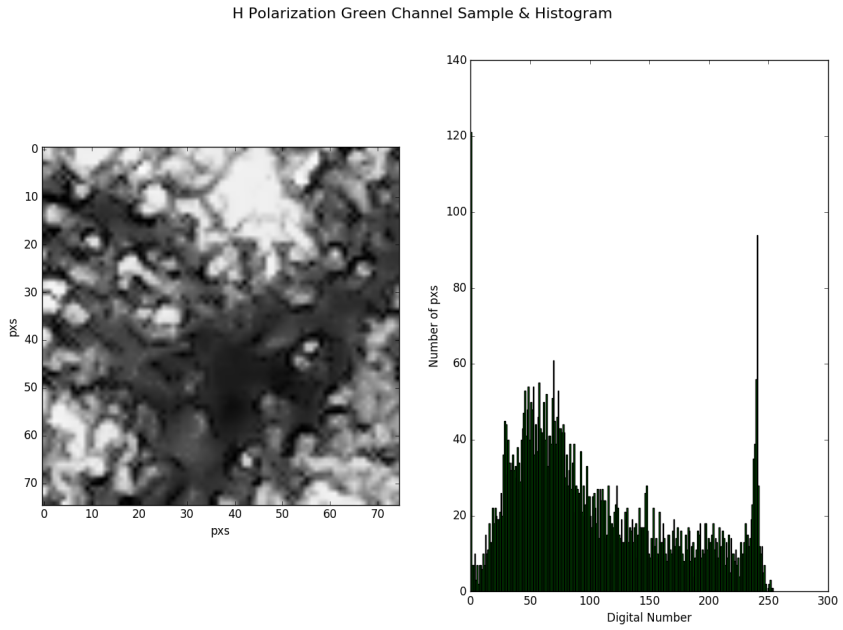


Figure 5.3: Devils Ivy Green Channel H Filter Histogram

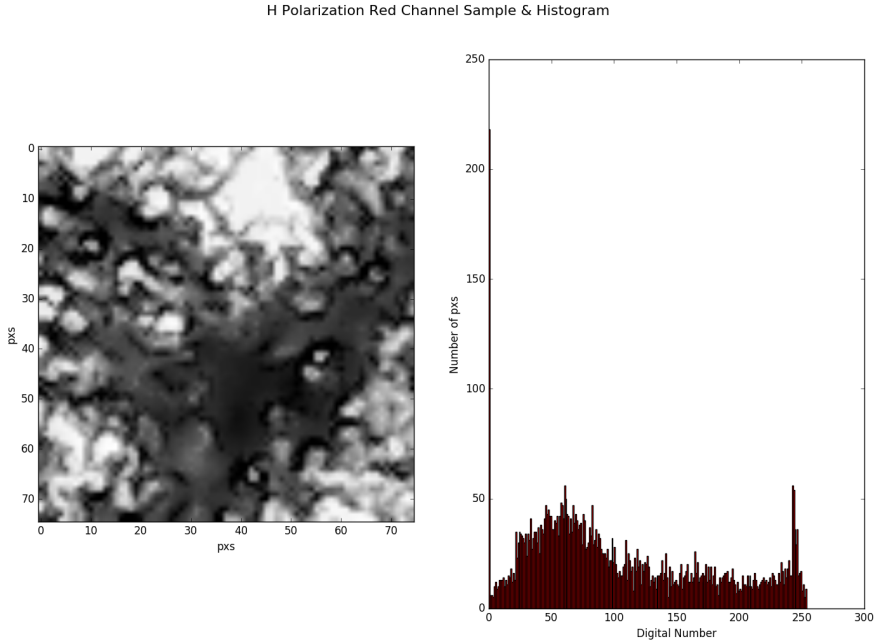


Figure 5.4: Devils Ivy Green Channel H Filter Histogram

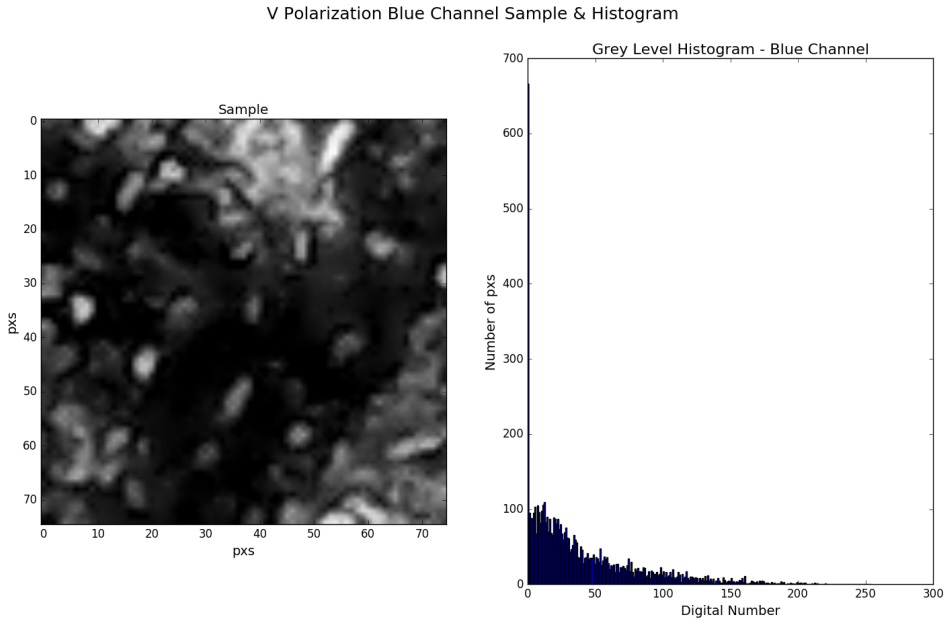


Figure 5.5: Devils Ivy Blue Channel V Filter Histogram

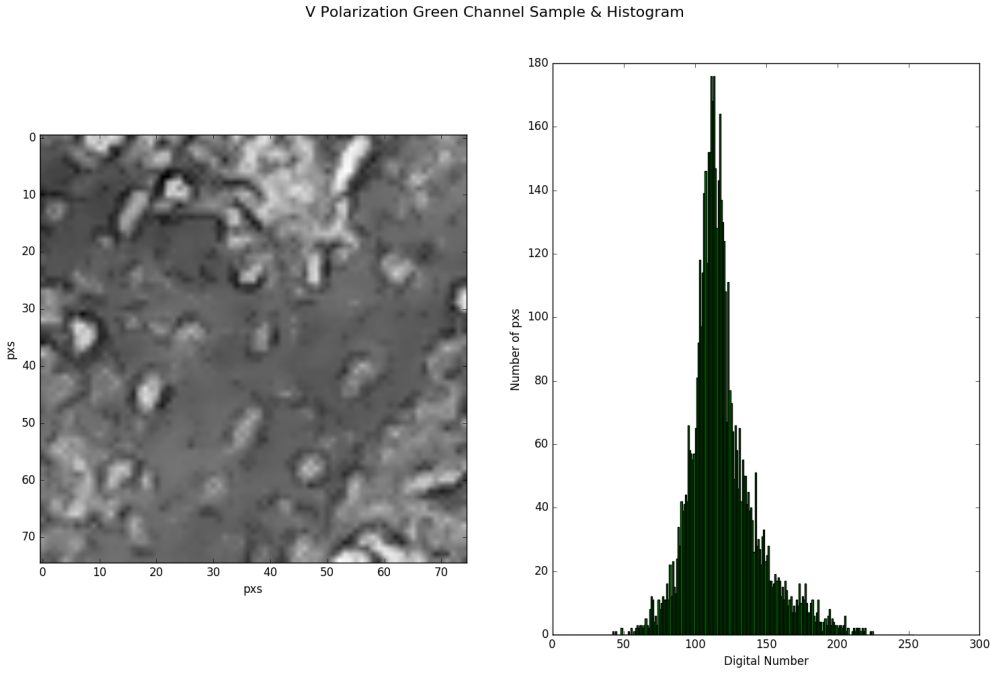


Figure 5.6: Devils Ivy Green Channel V Filter Histogram

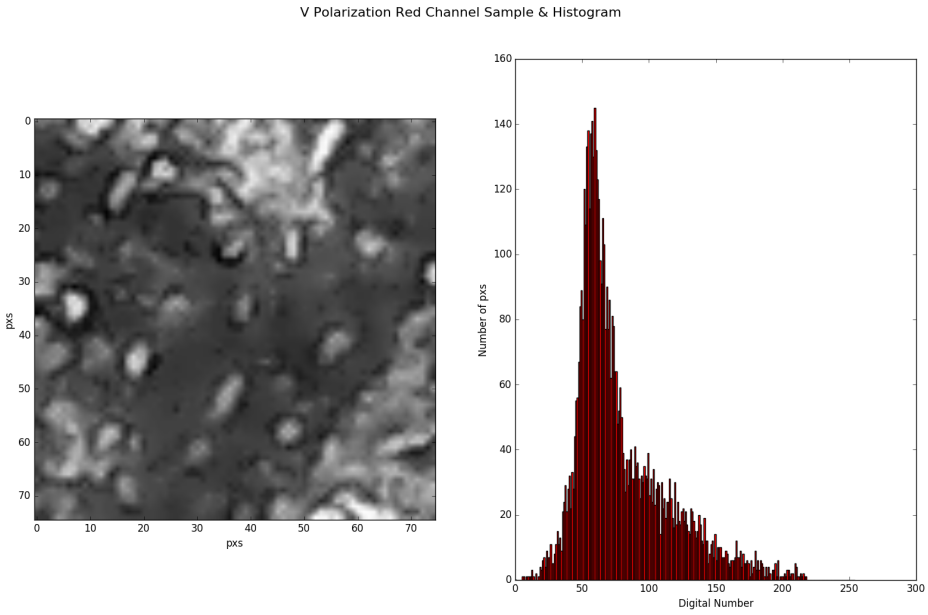


Figure 5.7: Devils Ivy Red Channel V Filter Histogram

In addition to performing a polarization based analysis on each color channel of the extracted samples, a GLCM texture analysis was also performed. The dissimilarity, contrast, correlation and energy were calculated for each sample window. The following code was used for these calculations, The metrics derived from the GLCM matrix can be plotted in various scatterplots as demonstrated in the Results chapter and Appendix. Data was exported to .csv files for future processing and analysis in Support Vector Machine classification and linear regression. Pixel-based, histogram counts and GLCM derived, window-based metrics were combined to form feature vector sets in the classification and regressions given in Chapter 7.

```
def calculate_stokes((P1, P2)):
    """
    Calulate the Stokes parameter for orthogonal images.

    Args:
        P1 (array): First polarization image.
        P2 (array): Orthogonal polarization image.
    Returns:
        array: Stokes parameters.
    """
    P1 = P1.astype(np.float32)
    P2 = P2.astype(np.float32)

    P1[np.abs(P1) < 1] = 0
    P2[np.abs(P2) < 1] = 0

    S = (P1 - P2) / (P1 + P2)

    # These represent values that have not been illuminated by the source
    # ie they are the product of masking and shadowing.
    S[~np.isfinite(S)] = 0

    return S
```

Figure 5.8: Example Code for Calculating the Stokes Parameters

```
S1 = calculate_stokes((H, V))
S2 = calculate_stokes((P, M))

plt.title('Polarizance Paramaters')

plt.hist(S1.ravel(), histtype='barstacked', bins=256)
plt.hist(S2.ravel(), histtype='barstacked', bins=256)

plt.show()
```

Figure 5.9: Calculate and Plot the Stokes Parameters

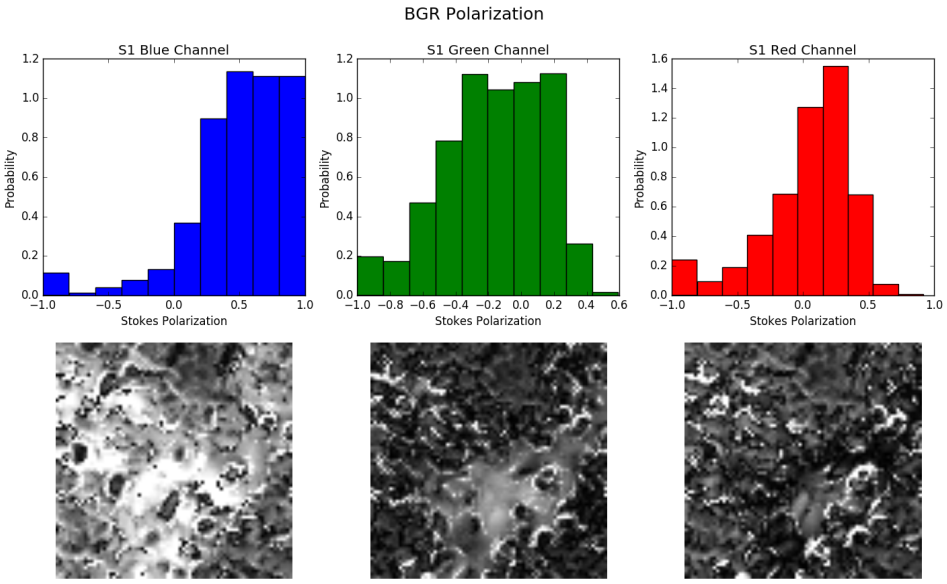


Figure 5.10: BGR Histograms for Devils Ivy Sample S1 Polarization Parameter

```
def extract_texture(samples):
    """
    Generate GLCM based texture features for a given color channel.

    Args:
        samples (array): Array containing each image sample. Each sample is a
            matrix of pixel intensities for a single color channel.
    Returns:
        array: Texture features extracted for an individual color channel.
    """
    texture = []
    for sample in samples:
        try:
            # Calculate texture features for a given sample
            relationships = [0, np.pi/4, np.pi/2, 3*np.pi/4]
            glcm = greycomatrix(sample, [1], relationships, 256, symmetric=True,
                 normed=True)
            metrics = ['dissimilarity', 'contrast', 'correlation', 'energy']
            diss, contrast, corr, energy = [greycoprops(glcm, metric)[0, 0] for metric in
                 metrics]

            texture.append([diss, contrast, corr, energy])
        except ValueError:
            print "Error in extracting the texture features"

    return np.array(texture)
```

Figure 5.11: noobee code for Jones Vectors

# 6 Classification and Regression Analysis

"...in the whole of nature there is something which makes all things, so too is it in the soul."

*On the Soul, The Philosopher*

## 6.1 Support Vector Machines

A Support Vector Machine (SVM) is binary classification tool that is used in machine learning classification and regression problems. SVMs attempt to separate data by creating a hyper plane that maximizes the distance between each of the classes. This is often performed in high dimensional spaces, where each sample is described by multiple features.

The python package Sci-Kit Learn provides access to SVM modules and utilities that make it easy to run analysis on datasets. This packages allows for easily performing machine learning classification and cross validation. Pipelines are useful for streamlining any preprocessing steps before classification. This allows for easy modification and testing of various steps in the machine learning process. A pipeline can be setup in order to allow for easy access to the classifier processing steps during analysis such as,

The OneVsRestClassifier was used to extend binary classification methods to multiclass problems, allowing for the use of SVC to classify Red Oak, American Ash and Sugar Maple leaves. The chosen kernel was linear. The GridSearch module of sklearn can additionally be utilized to find the most optimal parameters for fitting the data, when free parameters are available.

In Support vector classification, the C and epsilon are tunable parameters, that describe the penalty for support vectors inside of the margin of separation.

```
from sklearn import svm
from sklearn.multiclass import OneVsRestClassifier
from sklearn.preprocessing import StandardScaler

clf = OneVsRestClassifier(make_pipeline(
   StandardScaler(),
   svm.SVC(kernel='linear', probability=True)))
```

Figure 6.1: OneVsRestClassifier Pipeline Example

| Total Population | Condition Positive | Condition Negative |
|---|---|---|
| Predicted Positive | True Positive | False Positive |
| Predicted Negative | False Negative | True Negative |

Figure 6.2: Receiver Operating Characteristic Outcomes

### 6.1.1 Validation of Classifier Results

Cross validation of results is important for reducing the training and testing bias inherent to some datasets. Learning curves are useful visualization tools for showing how adding more samples to a testing set affects the classification score or ability.

A stratified K-fold validation can be used for ensuring that when sets of training and testing sets are created, the testing sets contain equal amounts of each class. This is especially useful in unequally distributed sets of data.

In binary classification problems, it is of interest to understand the ability of a classifier to correctly predict the true condition of the sample under inspection. The possible outcomes of a classification can be found in Figure 6.2. A true positive result is one that correctly identifies the sample. False negatives incorrectly predict that a sample was not in its own class. False positives are when samples are incorrectly identified with another class. True negatives correctly identify that a sample is not a member of the class being tested against. These rates can be combined into useful metrics for quantifying a classifiers performance.

The precision of a classifier is a measure of the relevancy of its results. It is an overall indicator of the false positive rate of a classifier.

$$P = \frac{T_p}{T_p + F_p} \tag{6.1}$$

were $T_p$ is the number of true positives and $F_p$ is the number of false positives that result from testing on the trained classifier. The recall, also known as the sensitivity, is defined as

$$R = \frac{T_p}{T_p + F_p} \tag{6.2}$$

and tells the amount of relevant samples returned and $F_n$ is the false negative rate. The F1 score is the harmonic mean between the precision and recall, and is defined as

$$F1 = 2\frac{PR}{P + R} \tag{6.3}$$

The classification report shows a useful cross validated summary of the precision, recall, F1 score, and support vectors that result from testing different dataset.

All of these features are available in the Sklearn package and an example is shown below.

```
from sklearn.model_selection import classification_report, StratifiedKFold

cv = StratifiedKFold(5, shuffle=True)

for train, test in cv.split(X, y):
    y_test = label_binarize(y[test], classes=[0,1,2])

    fit = clf.fit(X[train], y[train])

    y_pred = fit.predict(X[test])

    print classification_report(y[test], y_pred)
```

Figure 6.3: Training and Testing in K-fold

These metrics are often visualized using receiver operating characteristic (ROC) curves for binary classification, and confusion matrices for multi-class problems. ROC curves show the sensitivity vs the specificity of a binary classifier by plotting the false positive rate versus the true positive rate. It "is a graphical plot that illustrates the diagnostic ability of a binary classifier system as its discrimination threshold is varied" [39]. The area under the ROC curve, often denoted AUC, is a measure equivalent to the score of a classifier. It should be noted that for multi-class problems ROC curves can be more optimistic than the individual performance metrics.

ROCs can be extended to multi-class problems, by using a one verse many techniques although a confusion matrix is often used to show the accuracy of a classifier between each of the various classes. A mutli-class ROC curve would show each class in prediction to all other classes, therefore still becoming a binary decision. A confusion matrix shows the classifier score against each combination of true value and predicted value. It therefore shows all outcomes of classification.

It is important to understand the bias and variance of a model when determining its overall effectiveness. The bias is the average error for different training sets while the variance indicates how sensitive a model is to varying training sets.

Learning curves are a useful visualization tool for understanding the bias and variance of a classification model. It is useful for determining if a model gets better at classifying samples, as the number of training samples increases. If the score of a classifier decreases as the number of samples increases, the model has a high amount of bias. The model performance is not generalized enough to handle more training data. If, as the number of training samples increases, the score increases, the model could benefit from more training data. If the score remains constant as the training samples increase, the model has low bias.

## 6.2 Linear Regression

A linear regression is a simple approach to supervised learning that has long been in use in the field of statistical learning. It provides the ability to predict a quantitative response $Y$, given a predictor

variable $X$. The assumption when using this technique is that the relationship between these two variables is linear. In general the form of a Simple Linear Regression is

$$Y = \beta_0 + \beta_1 X \tag{6.4}$$

where $\beta_0$ and $\beta_1$ are parameters that are calculated using a set of training data. Once trained, this model can predict future output values for a given input. When given a set of observations $\beta_0$ and $\beta_1$ are set in order to have a closeness between the predicted line and the actual observed data. A common measure of this closeness is the least squares error.

The residual, $e$, for a given set of observations and predications is calculated

$$e_i = y_i - \hat{y}_i \tag{6.5}$$

These residuals can be used to calculate the Residual Sum of Squares $RSS$, or the amount of variation left unexplained after performing the regression. It is

$$RSS = {e_1}^2 + {e_2}^2 + \cdots + {e_n}^2 \tag{6.6}$$

where $n$ is the number of observations in a dataset.

The Total Sum of Squares is the measure of how much variability exists within the data before the regression has been performed. It is defined as

$$TSS = \sum_{i=0}^{n} (y_i - \bar{y})^2 \tag{6.7}$$

where $\bar{y}$ is the mean. Using the $RSS$ and $TSS$ allows for determining the accuracy within the model by calculating the $R^2$. The $R^2$ is the "proportion of variability in $Y$ that can be explained by $X$". It is defined as

$$R^2 = \frac{TSS - RSS}{TSS} = 1 - \frac{RSS}{TSS} \tag{6.8}$$

For a given application it is difficult to determine what a 'good' $R^2$ score is, although it has been noted that in biological applications there can be a great deal of unexplained variance, sometimes even less than 0.1 [40]. In these experiments a linear regression was utilized to correlate the relative water content of the Devils Ivy plant leaves, with the first principal component derived from texture and polarization characteristics. $R^2$ was used to gauge the accuracy of the results.

### 6.2.1 Principal Component Analysis

When a dataset has a large number of features, it becomes difficult to visualize these features against a given model. Principal Component Analysis (PCA) allows for reducing the dimensionality of data by combining variables that are highly correlated. By performing this process, it becomes possible to observe only the features that contain as much information as possible. For the dataset utilized in these experiments the features were more than a few dozen in total so reducing the dimensionality was important when visually interpreting the results. The Scikit-learn Python

module has a helper utility to provide this reduction in dimensionality. The code used for performing the linear regression and plotting the first principal component versus the relative water content can be found in Figure 6.4.

```
from __future__ import division
import numpy as np
from sklearn.model_selection import train_test_split, cross_val_score
from sklearn import linear_model
from sklearn.decomposition import PCA as sklearnPCA
import matplotlib.pyplot as plt
from sklearn.preprocessing import normalize
from sklearn.metrics import r2_score, explained_variance_score, mean_squared_error
from sklearn.preprocessing import FunctionTransformer
from sklearn.preprocessing import PolynomialFeatures

transformer = FunctionTransformer(np.log1p)
data = np.genfromtxt('data.csv', delimiter=',')
X = data[:,1:]
X = normalize(X, axis=1)
X = transformer.transform(X)
poly = PolynomialFeatures(degree=1)
X = poly.fit_transform(X)
y = data[:,0]

pca = sklearnPCA(n_components=1)
X = pca.fit_transform(X)

mean = np.mean(X)
std = np.std(X)

X_train, X_test, y_train, y_test = train_test_split(X, y, test_size=0.2, random_state=4)
regr = linear_model.LinearRegression()
regr.fit(X, y)

y_pred = regr.predict(X)

print "r2: ", r2_score(y, y_pred, multioutput='variance_weighted')
print "explained_variance_score: ", explained_variance_score(y, y_pred)
print "root mean squared: ", mean_squared_error(y, y_pred)
scores = cross_val_score(regr, X, y, cv=10)
print("Accuracy: %0.2f (+/- %0.2f)" % (scores.mean(), scores.std() * 2))

plt.title('Linear Regression For Relative Water Content')
plt.xlabel('First Principal Component')
plt.ylabel('Relative Water Content')
plt.scatter(X[:,0], y)
plt.plot(X[:,0].reshape(-1, 1), y_pred)

plt.show()
```

Figure 6.4: Linear Regression Example Code

# 7 Results

"I hear and I forget. I see and I remember. I do and I understand"

*Confucius*

## 7.1 Optimization of Parameters

The histograms that resulted from measuring the S1 and S2 polarization showed evidence of masking and shadowing effects due to macro level surface features. This caused some pixels to never be illuminated and have a large spike at zero.

Pixels that were never illuminated were removed from the histogram process. These were determined by checking if $P_H$, $P_V$, $P_P$, and $P_M$ never had a value more than 0. This removed the spike at zero.

The free parameters in Support Vector Classification were optimized using the Sklearn grid search module.

## 7.2 Classification

Images were acquired for each polarization filter orientation. Red Oak, American Ash, and Sugar Maple leaves were measured immediately after being removed from their host tree and polarization measurements were recorded. The same procedure was then performed 1 week later. These measurements produce interclass variance and show the effects of the decomposition process on the polarization response and texture of various leaf species. In total 18 different leaves were investigated for classification purposes under experimental design setup 1. Images were acquired in both the specular and diffuse directions for each leaf. 100 samples of 75 by 75 pixels were extracted from each leaf to represent various textures found on the surface and the physiological status below the surface. In total 1800 samples were used to perform classification and validation using a linear support vector classifier.

### 7.2.1 Specular Leaves

The principles of reflection and transmission as dictated by Fresnel's equations show that light reflecting from a specular surface will have higher amounts of polarization than when compared with the diffuse direction. The S1 component for all leaves showed this response as expected and produced higher amounts of polarization than when compared to their diffuse counterparts. The S2 component showed itself to have a near zero mean, with some variance.

Figure 7.1: From left to right: Red Oak, American Ash, and Sugar Maple through H polarization filter in the Specular Direction.

The histograms for the S1 and S2 parameters comparing different tree leaves were computed for the blue, green and red camera channels. These individual channels in general are the same as the overall grey level image shown as RGB here, although more distinguished features can be seen in Figure 7.2 for each individual channel. The blue and red channel show higher amounts of polar-

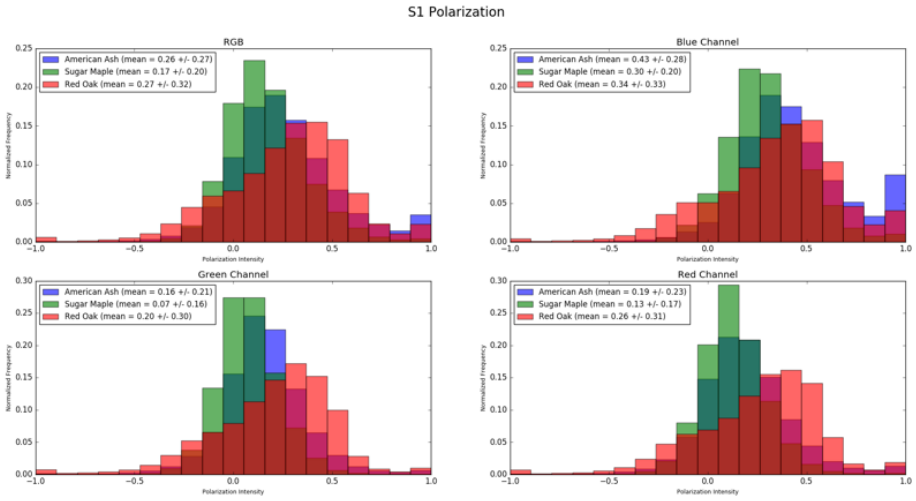


Figure 7.2: All plants specular observed direction for each RGB channelization 0 week for S1

ization, while the green channel shows the least amount of polarization, across each species. It has previously been shown, that Rayleigh scattering on a leafs' surface can greatly increase the polarization in the blue spectrum of light [26]. Since plants reflect highly in the green, the green channel shows the lowest amount of polarization. The blue channel shows the most amount of polarization, although this may be due to the sensitivity of the CMOS sensor or Rayleigh scattering [26]. The blue channel is extended to regions of red light and therefore is overall more sensitive in the visible region to spectral fluctuations. Perhaps in the future, the blue channel response should

be subtracted from the red channel response, and the blue channel can be normalized using the following ratio,

$$Blue_{calibration} = Blue - (Blue - Red) \tag{7.1}$$

Ideally the response of each channel would be carefully calculated using a spectrometer, and overall constants could be provided to normalize the sensitivity in each spectral region. This requires various narrow band spectral filters.

The S2 histograms in Figure 7.3 show very little polarization on average. This is expected polarization angles at 45 and 135 can be decomposed into $x$ and $y$ components. It is possible that the S2 component could be useful in understanding the calibration of the linear polarizer to its ideal orientation. If P and M measurements diverge drastically, it would serve as a notion to investigate the variance further for specular reflections. The specular direction of observation and incident

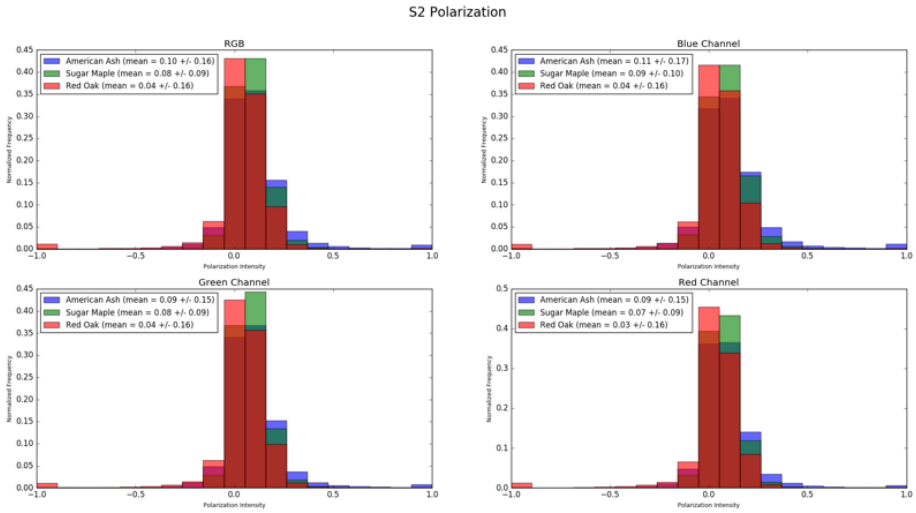


Figure 7.3: All plants RGB channels observed from the specular direction 0 week for S2

angle at the Brewster angle creates the highest amount of polarized light on an ideal smooth surface. Leaves can also be seen to similarly have specular components that correlate to the surface topology.

A GLCM texture analysis was also performed on each sample extracted to determine the dissimilarity, contrast, entropy, and correlation. Due to each of the GLCM features being generated from the same initial matrix, many of the features show high levels of correlation. In general, a measure should be taken from the orderliness group, contrast group and descriptive statistics group. It has been shown that a textures dissimilarity and correlation show low levels of correlation. Therefore, they are plotted here to represent the texture in 2 dimensions.

Although these features contain information regarding the texture of a surface, it is often difficult to determine what actually causes each metric to arise when describing specific surface GLCM properties [24].

Figure 7.4 shows the texture of the leaves above for the V filter orientation. It shows that each species exhibits its own unique texture that helps to visually create clusters, and therefore should prove useful for classification. Additional filter arrangements can be found in the Appendix.

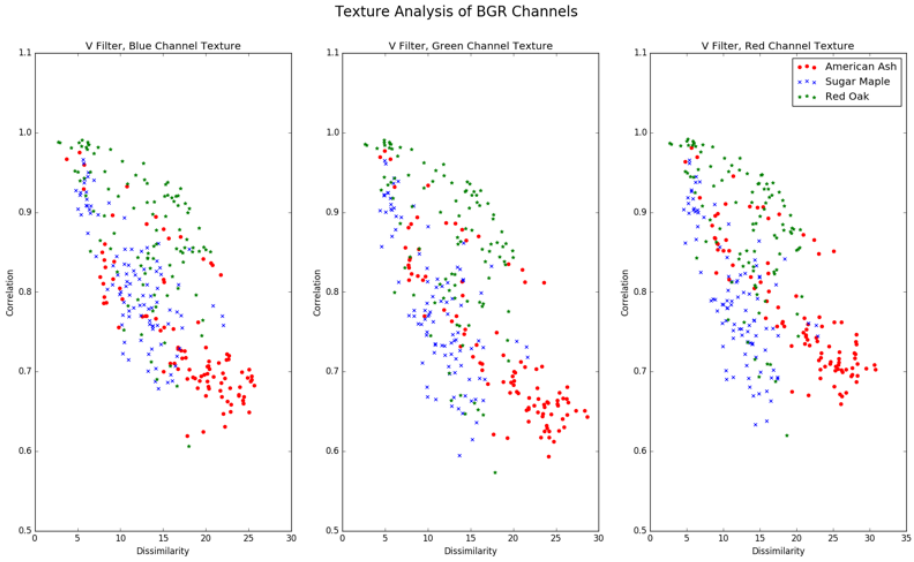


Figure 7.4: V filter GLCM dissimilarity and correlation for all species in the specular direction week 0

### 7.2.2 Specular Leaf Decomposition

As leaves start to undergo pigment breakdown and decomposition, the surfaces of the leaves provide more reflectance. The loss of water and pigment structure results in rougher external surface on the leaf that causes a more diffuse reflection, even when viewed at the Brewster angle. This results in a loss of magnitude of S1 polarization as the leaf decomposes. Visual changes to the surface of the leaf can be found in the original V filter images. Close inspection Figure 7.5 show that the

Figure 7.5: From left to right: Red Oak Freshly Removed and After One Week

new leaf is a darker green in color and has a smoother surface than the oak leaf after 1 week. The smooth, thick wax surface as it ages from week 0 to week 1, becomes flatter and segmentation of structures on the leaf surface becomes more evident.

Recording the leaves after one week to illustrate changes during decomposition and water loss for red oak can be seen in Figure 7.6. It should be noted that the blue channel contains a large amount of polarization after one week. In some cases, it has been seen to even exceed its 0-week counterpart. This may be due to the absorbance spectrum of chlorophyll and the lack of photosynthetic activity during decomposition. The overall S1 image shows the 0 week has higher polarization in S1 as its surface is more of a pure specular reflector. Again S2 only shows a slight

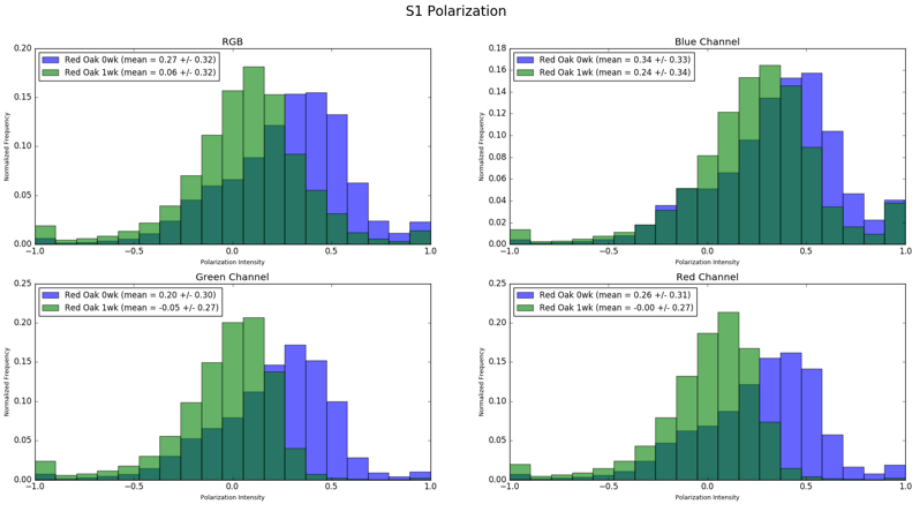


Figure 7.6: Red Oak 0 weeks and 1 week observed in the specular direction for S1

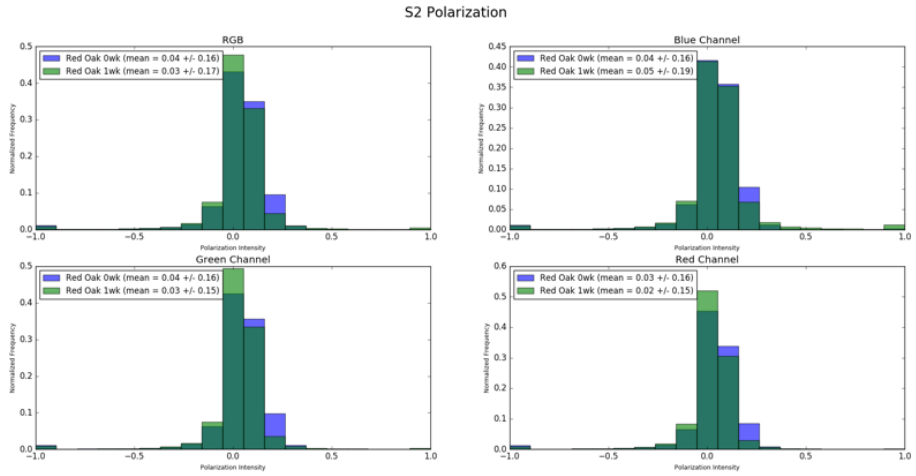


Figure 7.7: Red oak 0 weeks and 1 week observed in the specular direction for S2

variation even after re-measuring the leaf one week later.

The results of GLCM analysis for the P filter component can be found in Figure 7.8. Visual inspection of the GLCM scatter plot shows the best clustering using the P filter for this particular example. The full GLCM filter set can be found in the Appendix. As water leaves the leaf

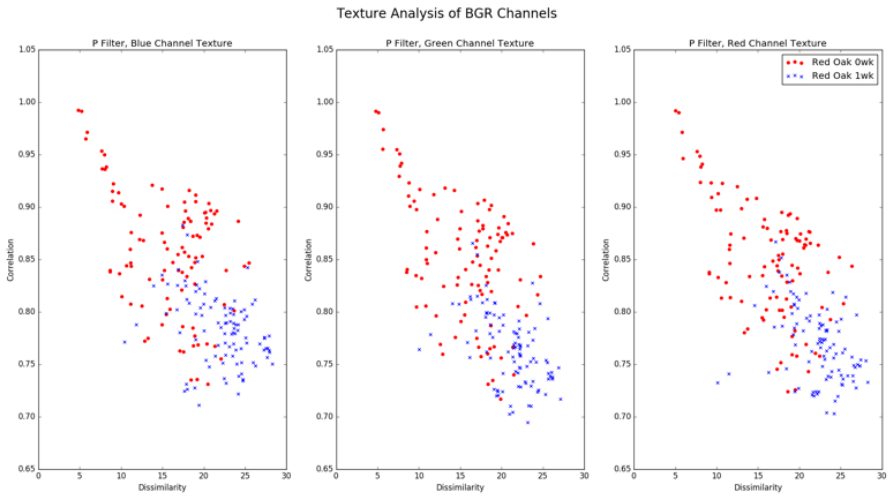


Figure 7.8: P filter GLCM dissimilarity and correlation in specular direction for 0 and 1 week.

which undergoes the decomposition process, the surface becomes rougher as the water that once supported much of the cells structure has been removed. The surface becomes more diffuse. The highly specular component of healthy leaves, creates maximum intensity levels on the cameras detector, making the surface appear smooth. This results in a higher amount of dissimilarity on the surface of the leaf after one week, as compared to one that is still healthy. The correlation is shown to also decrease as a result of this process as well.

### 7.2.3 Specular Classification Results

Classification was performed on datasets created by combining texture samples from leaves that were both zero week and one week old. This created variance within the classes themselves, as previously it has been shown how physiological changes within the leaf can lead to different polarization and texture results. The results of classification show that there is still an ability to distinguish between species with a high amount of precision.

The confusion matrix also shows the high level of accuracy when using ten fold stratified K fold validation. It can be seen that the highest accuracy of classification is when American ash is considered versus Maple or Oak. Visual inspection of each type of leaf shows the similarity between Oak and Maple when viewed under a microscope, so this result is not unexpected.

A learning curve was also generated for the results of using both texture and polarization features and is shown in Figure 7.10. As the number of training samples increases, the score of the classifier remains the same. This shows the low amount of training bias within the model created from our samples. Future samples should be collected and compared to further validate these re-

sults. The overall results for specular classification for all species using polarization and texture

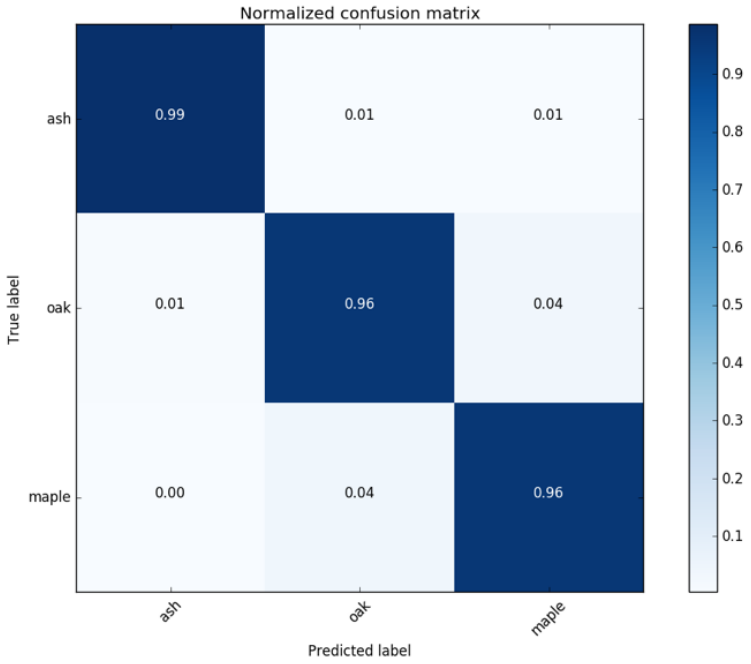


Figure 7.9: Confusion Matrix for All Species observed in the specular direction.

features where class 0 is American Ash, class 1 is Red Oak, and class 2 is Sugar Maple. It can be

| Class | Precision | Recall | F1 Score | Support |
|---|---|---|---|---|
| `0.0` | 0.99 | 0.98 | 0.99 | 600 |
| `1.0` | 0.95 | 0.95 | 0.95 | 600 |
| `2.0` | 0.96 | 0.96 | 0.96 | 600 |
| `avg/total` | 0.97 | 0.97 | 0.97 | 1800 |

Table 7.1: Scores for Classification in the Specular Direction with Polarization and Texture in Specular Direction.

seen that combining both polarization and texture features for classification, results in better precision, recall, and F1 scores than if either of the feature sets are used independently. This shows the benefit of using different types of features for classification.

### 7.2.4 Diffuse Leaves

Leaves from each species of tree were acquired at 0 degrees from the normal for the plane of incidence. Examples of each leaf captured through the H filter can be found in Figure 7.11.

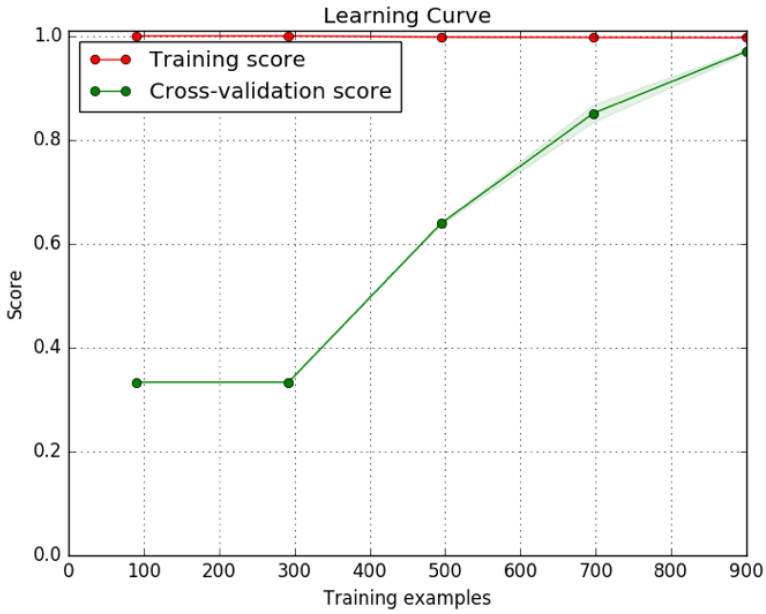


Figure 7.10: Learning curve for leaves observed in the specular direction.

| Class | Precision | Recall | F1 Score | Support |
|---|---|---|---|---|
| `0.0` | 0.95 | 0.97 | 0.96 | 600 |
| `1.0` | 0.88 | 0.92 | 0.90 | 600 |
| `2.0` | 0.93 | 0.87 | 0.90 | 600 |
| `avg/total` | 0.92 | 0.92 | 0.92 | 1800 |

Table 7.2: Scores for Classification in the Specular Direction with Just Polarization in Specular Direction.

The diffuse component of reflectance of a leaf is often thought of as being unpolarized. This assumption if based on a perfect Lambertian diffuse surface, which is often not the case. Although the portion of polarized light in the diffuse region of reflection is less than that of the specular portion, it cannot be discarded, as it may contain important information as to the biological and physiological processes within the leaf's internal structure.

As photons undergo multiple scattering processes and absorption and reemission by chlorophyll, they can become partially or completely polarized. These mechanisms are complex, and it is necessary to go beyond Fresnel's equations to dictate the major processes at work in the diffuse component of scattering. Polarimetric BRDF models attempt to ascertain the relationship between surface scatter and polarization of light.

Our results show that although the mean is centered around zero for S1, the S2 component shows various degrees of polarization. These may be due to multiple scattering mechanisms within the layers of the leaf.

| Class | Precision | Recall | F1 Score | Support |
|---|---|---|---|---|
| `0.0` | 0.97 | 0.96 | 0.96 | 600 |
| `1.0` | 0.86 | 0.89 | 0.87 | 600 |
| `2.0` | 0.90 | 0.87 | 0.88 | 600 |
| `avg/total` | 0.91 | 0.91 | 0.91 | 1800 |

Table 7.3: Scores for Classification in the Specular Direction with Just Texture in Specular Direction.

Figure 7.11: From left to right: Red Oak, American Ash, and Sugar Maple through H polarization filter in the Diffuse Direction.

The diffuse portion of polarization for each species is shown in Figure 7.12. It can be seen

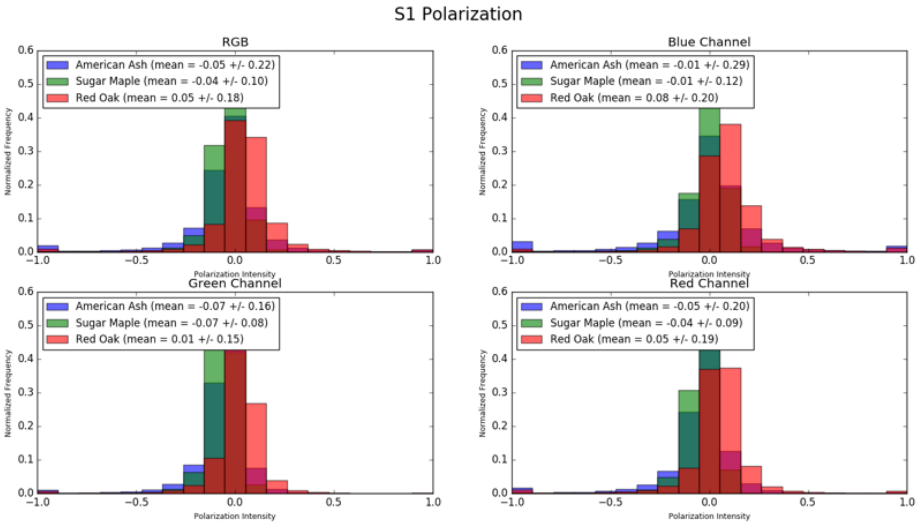


Figure 7.12: All species, for the diffuse angle of observation 0 week for S1.

that many of the leaves exhibit little to no S1 polarization. This is expected since much of the S1 polarization results from single scatter surface level phenomena. The polarization in S2 is shown to be significant.

The polarization can bee seen to be highest in the red and blue where absorption of photons by chlorophyll in the mesophyll layer of the leaf is most prominent. Structures such as veins may also cause unknown polarization states to result. Care should be taken when composing images as to what structures are desired for inspection.

The distribution between species in S2 are distributed around different means and variances are as shown in Figure 7.13. A GLCM analysis in the diffuse direction for all species shows visually

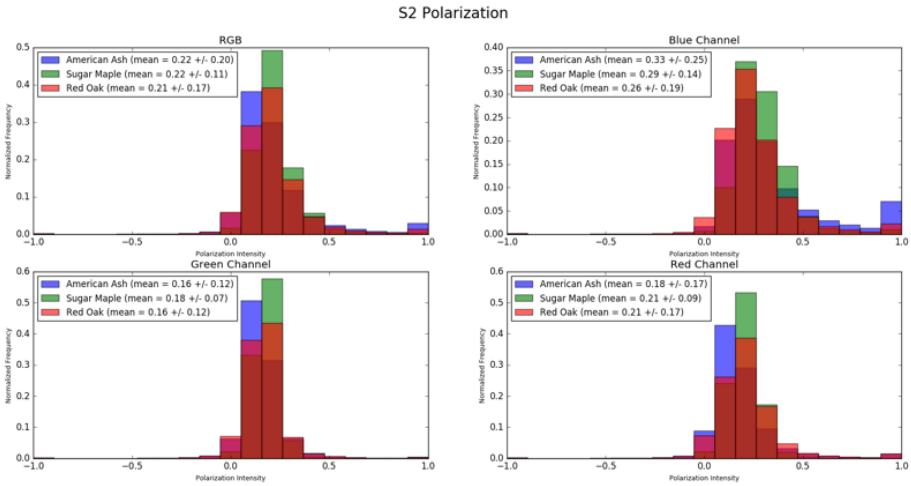


Figure 7.13: Polarization for all species in the diffuse direction of observation for S2.

distinct clustering. GLCM dissimilarity and correlation for diffuse scattering can be found in Figure 7.14.

### 7.2.5 Diffuse Leaf Decomposition

As the breakdown of the leaf occurs, fewer photons are utilized for photosynthesis. This results in fewer type B photon interactions as the leaves becomes more reflective. The diffuse portion of the fresh leaf contains a large amount of type B and C photons. Intricate structures can be seen in the leaf not seen in the specular images since the diffuse light does not oversaturate the sensor. The images above show that in the diffuse direction for Red Oak freshly removed, there are numerous micro segmentations on the leaf surface that were not evident in the specular direction. These complex wax structures increase the amount of multiple scattering. As the leaf decomposes, the micro segmentations become less evident as the larger structures become the most prevalent feature on the surface.

Figure 7.16 and Figure 7.17 show's the S1 and S2 polarization in the diffuse direction for a Red Oak leaf as it undergoes the decomposition. The S1 polarization component is low for both the fresh and decomposing leaf in the diffuse direction. Most of the polarization that results is not purely perpendicular or parallel to the incident surface. The S and P component of polarization are mostly cancelled out. There is S2 polarization that arises from each specimen, and it is shown to be higher for red oak leaves that are undergoing the process of decomposition.

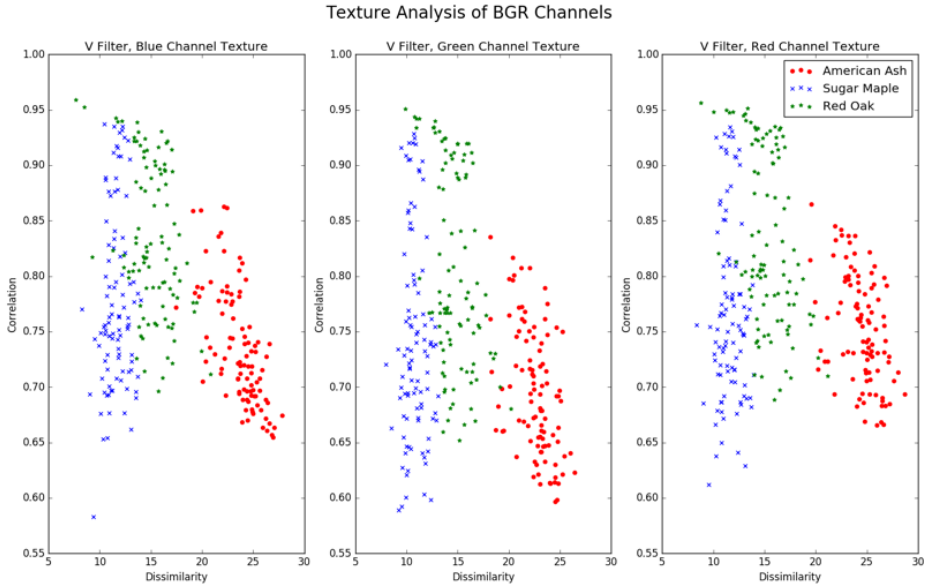


Figure 7.14: V filter GLCM dissimilarity and correlation for all species in diffuse direction 0 weeks.

Figure 7.15: From left to right: Red Oak Freshly Removed and After One Week

As the composition of a leaf changes, more polarization results as an effect of the physiological breakdown causes less absorption and more volume scattering. Although diffuse surfaces are supposed to create equal amounts of randomized polarized states, resulting in no overall polarization, it is shown here that in some cases the diffuse portion is polarized, especially in the S2 component. This information could potentially be useful for determining physiological properties of leaves.

The GLCM in the diffuse direction shows that as the wax structure becomes less filled with water and decompresses, the surface of the leaf appears smoother, since there is less noise caused by multiple scattering through the thicker wax cuticle of the fresh leaves. The result is that healthier leaves create more dissimilarity for the captured images. This is shown in Figure 7.18. The multiple scattering and microstructures evident in the thicker wax of a freshly removed oak leaf creates a high amount of dissimilarity and lower correlation than after a week of drying.

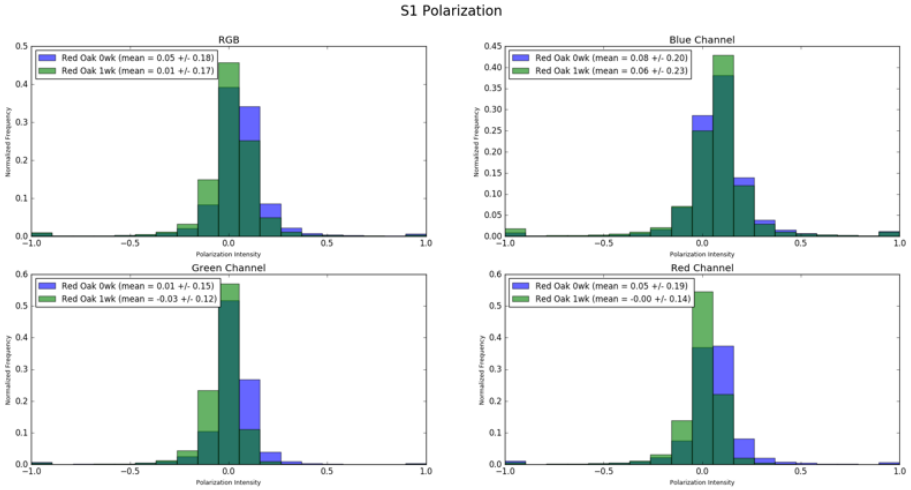


Figure 7.16: Red Oak in the diffuse direction for S1

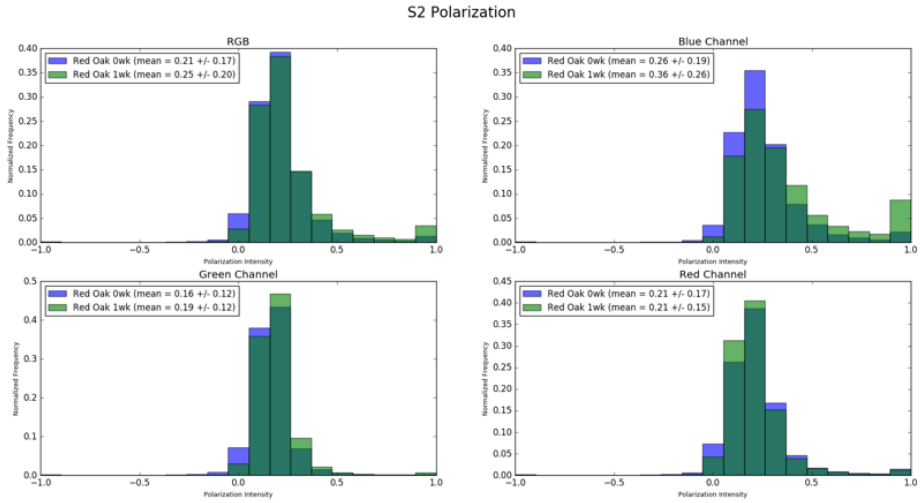


Figure 7.17: Red Oak in the diffuse direction for S2

### 7.2.6 Diffuse Classification Results

Support vector classification was performed on all leaves collected for each of the species with zero and one week combined in order to show the ability to classify similar species even if interclass variance exists. Overall the diffuse results were slightly less accurate than the specular results, but this may be due to the overall noise in the diffuse images acquired. Further investigation is required in this regard.

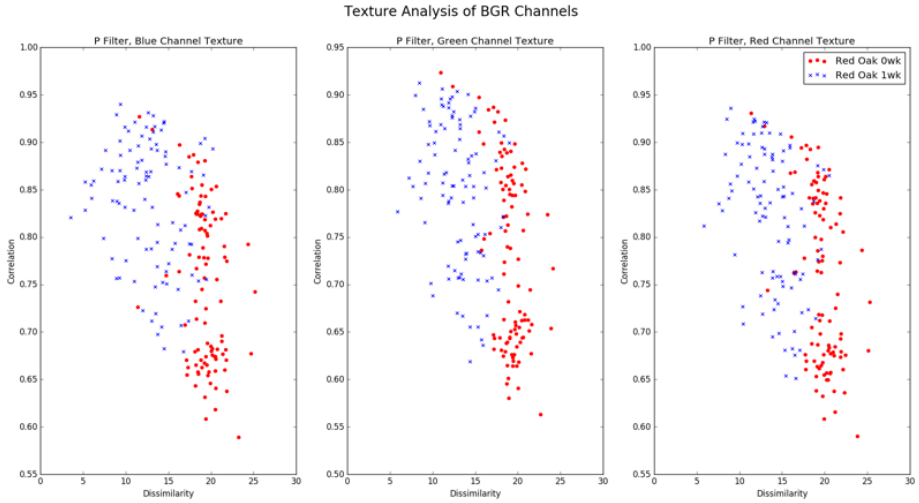


Figure 7.18: P filter GLCM dissimilarity and contrast in diffuse direction for red oak 0 week vs 1 week

The confusion matrix shows that ash is the most correctly identified class, with the highest precision and recall when compared to other classes. Classification precision for oak and maple were similar.

The learning curve shows good results as more samples are added, but towards the end shows the score decreases slightly. Additional samples should be investigated to ensure the validity of this model.

Overall the model does show correlation between each species texture and polarization characteristics. This is indicated by high accuracy in classification as shown by the confusion matrix and the precision scores seen in Table 7.4. Comparison of with the use of in Table limited feature

| Class | Precision | Recall | F1 Score | Support |
|---|---|---|---|---|
| `0.0` | 0.98 | 0.99 | 0.99 | 600 |
| `1.0` | 0.93 | 0.94 | 0.94 | 600 |
| `2.0` | 0.93 | 0.92 | 0.93 | 600 |
| `avg/total` | 0.95 | 0.95 | 0.95 | 1800 |

Table 7.4: Scores for Classification in the Diffuse Direction with Polarization and Texture in Diffuse Direction.

sets, shows again that texture combined with polarization returns better results than if only one were used. Overall classification in the diffuse direction was slightly less accurate than that of our specular measurements.

In the future principal component analysis should be utilized to isolate the top parameters for each group in order to eliminate any bias that is caused from there being more polarization features

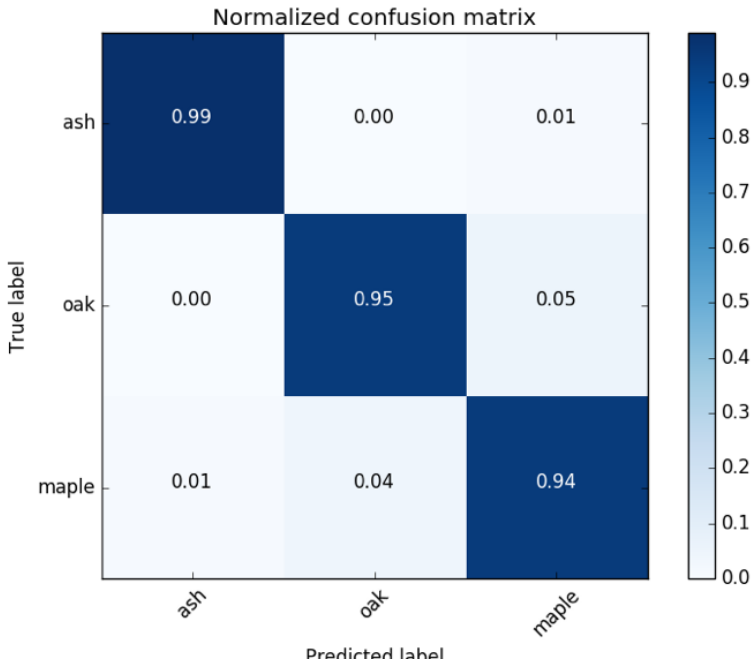


Figure 7.19: Confusion matrix for all species observed in the diffuse direction.

| Class | Precision | Recall | F1 Score | Support |
|---|---|---|---|---|
| `0.0` | 0.94 | 0.95 | 0.94 | 600 |
| `1.0` | 0.90 | 0.92 | 0.91 | 600 |
| `2.0` | 0.89 | 0.86 | 0.88 | 600 |
| `avg/total` | 0.91 | 0.91 | 0.91 | 1800 |

Table 7.5: Scores for Classification in the Diffuse Direction with Just Polarization in Diffuse Direction.

than texture features. An additional image should be acquired with no polarization filter in place, to represent $S_0$ and create a better mark for texture feature only comparison.

## 7.3 Regression

Previous results show that classification between species can be performed with high levels of accuracy even if a large amount of interclass variance exists due to varying physiological states of each leaf. Therefore, investigation into acquiring more accurate measures as to the plants' current physiological state, such as water and pigment concentration, would be useful for a more detailed explanation of previous results.

Determining the relationship between the relative water content of a plant's leaf, versus features extracted from images taken in the visible portion of the spectrum with a camera, requires data to

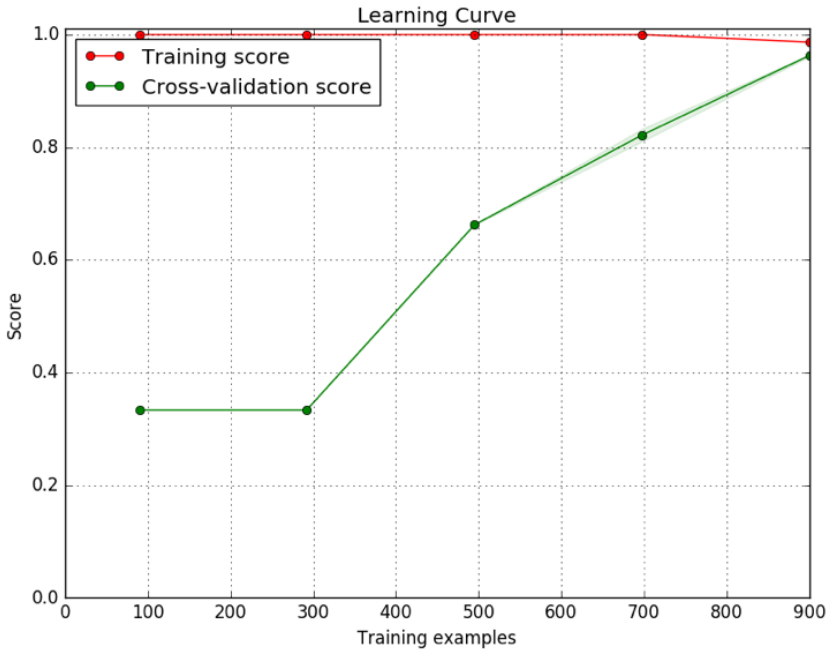


Figure 7.20: Learning curve for All species observed in the diffuse direction

be fit in a regression model. Support Vector Regression (SVR) is an extension of linear regression with the purpose of minimizing the distance of each point to the best fit line.

The y dependent variable was determined by measuring the relative water content of the Devils Ivy plant using the procedure previously described. Samples were extracted from each polarization filter for the purpose of GLCM analysis. The average dissimilarity, contrast, energy and correlation of 100 samples randomly selected from the entire image were utilized to quantify the texture of each individual leaf at different levels of RWC. The S1 and S2 polarizance parameters were also calculated for each individual pixel. Each pixel was binned together to create histograms for S1 and S2. The probabilities for 20 bins ranging from -1 to 1 were utilized to determine the polarization component of each sample.

| Class | Precision | Recall | F1 Score | Support |
|---|---|---|---|---|
| `0.0` | 0.98 | 0.99 | 0.99 | 600 |
| `1.0` | 0.77 | 0.85 | 0.81 | 600 |
| `2.0` | 0.84 | 0.74 | 0.79 | 600 |
| `avg/total` | 0.86 | 0.86 | 0.86 | 1800 |

Table 7.6: Scores for Classification in the Diffuse Direction with Just Texture in Diffuse Direction.

Principal component analysis was utilized to extract the most useful features for plotting against the RWC. The principal component can be seen plotted against RWC for the specular case in Figure 7.21. Analyzing the specular polarization and extracting texture features showed high

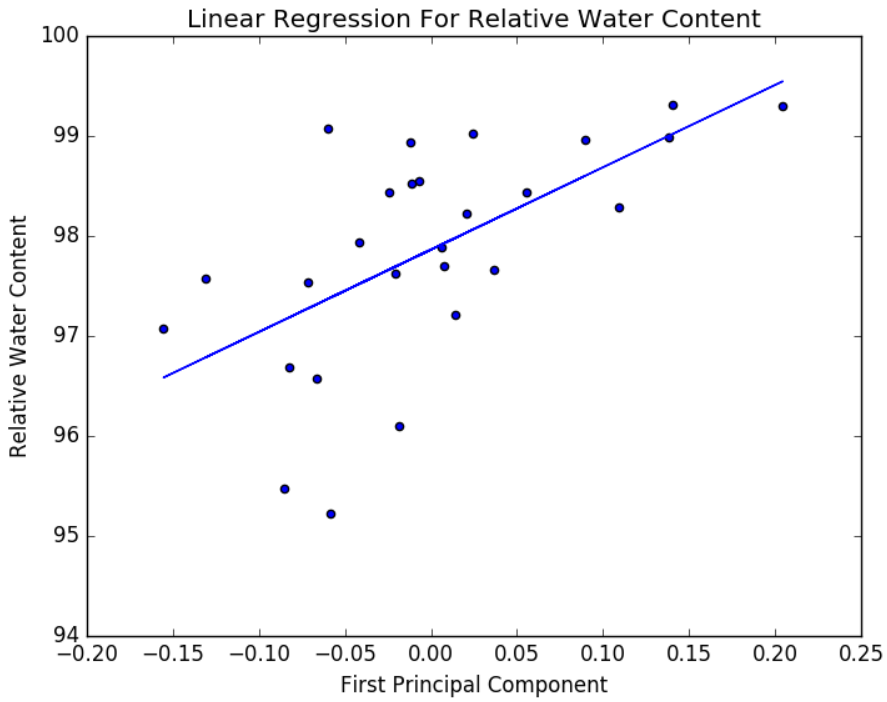


Figure 7.21: Linear Regression for RWC and 1st principal component - Specular

| Metric | Score |
|---|---|
| r2 | 0.376 |
| RMS | 0.758 |

Table 7.7: Scores for Regression in the Specular Direction

levels of correlation for biological regression problems with an $r^2$ of 0.376. The classifier was cross validated using K-fold validation with 10 folds. The performance of the classifier is summarized in Table. The root mean squared shows the accuracy to be within 0.5The diffuse direction did not have as much usefulness in determining the RWC for the data that was acquired and tested. The $r^2$ value was nearly zero, meaning the $Y$ values could not be explained by the input $X$ variables for the linear relationship tested. Figure 7.22 shows this poor relationship. Further analysis and data reduction techniques could be applied to further analysis any potential relationship between texture, polarization and relative water content.

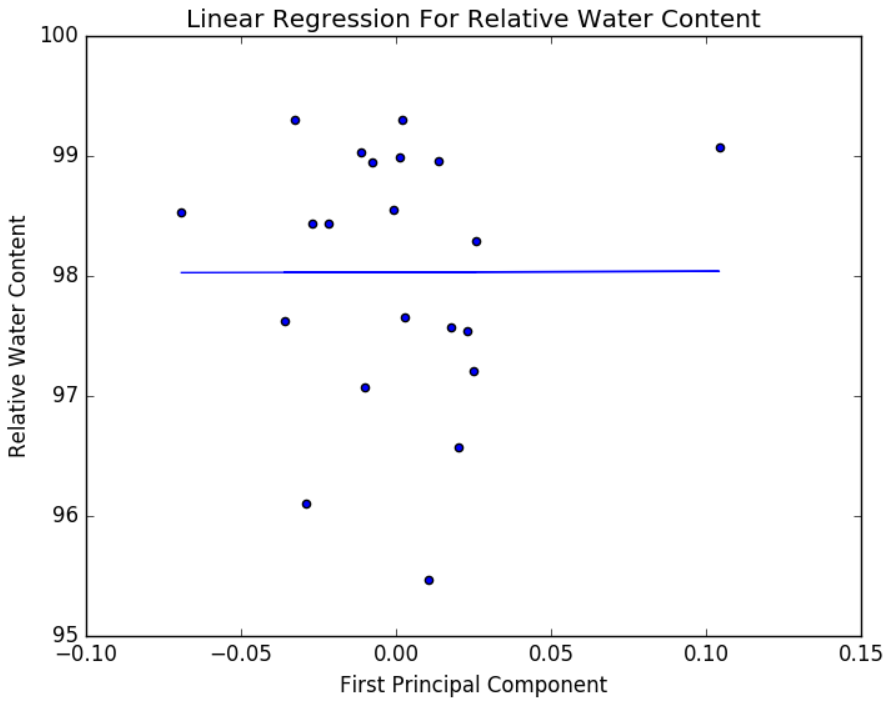


Figure 7.22: Linear Regression for RWC and 1st principal component - Diffuse

| Metric | Score |
|---|---|
| r2 | 4.178e-06 |
| RMS | 1.126 |

Table 7.8: Scores for Regression in the Diffuse Direction

# 8 Conclusion

"It would not be much of a universe if it wasn't home to the people you love."
*Stephen Hawking*

The need for precisely monitoring the health of vegetation as resources become more scare will become a necessity for human survival. The sensing technologies involved with satellites, drones, and indoor greenhouses provide information the first steps in technologies towards understanding photon vegetation interactions. Understanding the processes involved and influenced by these interactions allows for the potential to gain deeper understanding into the data we acquire.

The initial assumption of the diffuse portion of light being an unpolarized scattering mechanism is starting to give way with new experimentation and research into the properties of this interaction with a wide variety of materials and substances showing there is information to be gained in observing the polarization in the diffuse portion. Texture has been used in remote sensing technologies for the purpose of classifying the various areas within an image. The inclination to bring these ideas to micro scale agricultural systems in greenhouses throughout the solar system can be useful going forward as interest in this field grows.

This research has set a foundation for a discussion surrounding the information to be gained from observing the polarization response that results from incident unpolarized light onto a leafs surface. Images were acquired with plants in various physiological conditions, including decomposition and water stress. The texture of the leafs' surface was observed to change as these processes progressed.

The polarization created by a material when unpolarized light is incident, as in most natural settings, has been shown to reveal distinguishing characteristics for determining both the species and physiological state of vegetation. Although normally assumed to be unpolarized, the diffuse portion of reflectance contains information that can be useful for classification and plant health analysis. The specular portion of light also contains distinguishing information and in our results provided better classification.

As areas in precision agriculture expand into areas of indoor growing operations in more controlled environments, the application of precise amounts of agricultural inputs will become more viable. A better understanding of the effects of light on individual plants for determining their overall health will be useful in the future as resources become more scarce.

Results for Red Oak have been provided in detail for this report as it provides the simplest explanation for the results. Each species provides slightly different results depending on its composition. Further explanation would have to be given at an individual species level to account for these results.

The relative water content of leaves is shown to be correlated with both its texture and polarization response when captured by a digital microscope behind a rotating linear polarizer.

Further improvements to experiment design, plant health status control, image acquisition and segmentation should be taken to improve the results of regression. Plants can be controlled at a finer level when grown by starting seeds from scratch in a controlled environment. Inputs to each individual plant could be altered including various fertilizers and water amounts. Paper chromatography methodologies,as discussed in [41] could be used for determining the various distribution of pigments throughout smaller subsections of the leaves. By creating false images with polarization and texture information, smaller sections of leaves could be isolated and correlated with each feature. Image acquisition could be improved by reducing the amount of undulations on a leafs surface, in order to reduce the amount of effects that arise from masking and shadowing. Different light sources should be investigated to determine the consistency of our results. Image segmentation may prove beneficial to isolating the effects of localized features. Physiological indicators, such as pigment concentrations, in addition to relative water content should be investigated to further show health status and correlate the polarization response.

In the area of polarization and texture modeling, examples could be given as to how various textures, such as sandpaper, glass, etc. are related to their polarization response in a simplistic model.

Overall this study has provided a basis for many of the principles required for understanding the micro scale concepts involved with the sensing of vegetation. Improvements to current models and suggestions for areas of further study, have been provided.

# Acronyms

| | |
|---|---|
| ASM | angular second moment |
| BRDF | Bidirectional Reflectance Distribution Functions |
| COTS | Consumer off the shelf |
| DOCP | Degree of circular polarization |
| DOLP | Degree of linear polarization |
| DOP | Degree of polarization |
| DW | Dry weight |
| EM | electromagnetic |
| FW | Fresh weight |
| GLCM | Grey Level Co-Occurrence Matrix |
| GOES | Geostationary Operational Environmental Satellites |
| LP | Linear polarizer |
| MM | Mueller matrix |
| NAIP | National Agricultural Imagery Program |
| NDVI | Normalized Difference Vegetation Index |
| NEX | NASA Earth Exchange |
| NIR | Near infrared |
| pBRDF | Polarimetric Bidirectional Reflectance Distribution Functions |
| PCA | principal component analysis |
| QWP | Quarter wave plate |
| ROC | receiver operating characteristic |
| RSS | Residual Sum of Squares |
| RWC | Relative Water Content |
| SVC | Support vector classifier |
| SVM | Support vector machines |
| TA | Transmission axis |
| TE | transverse electric |
| TM | transverse magnetic |
| TSS | Total Sum of Squares |
| TW | Turgid weight |
| VARI | Visible Atmospherically Re- sistant Index |
| VI | Vegetation indices |

# Appendix

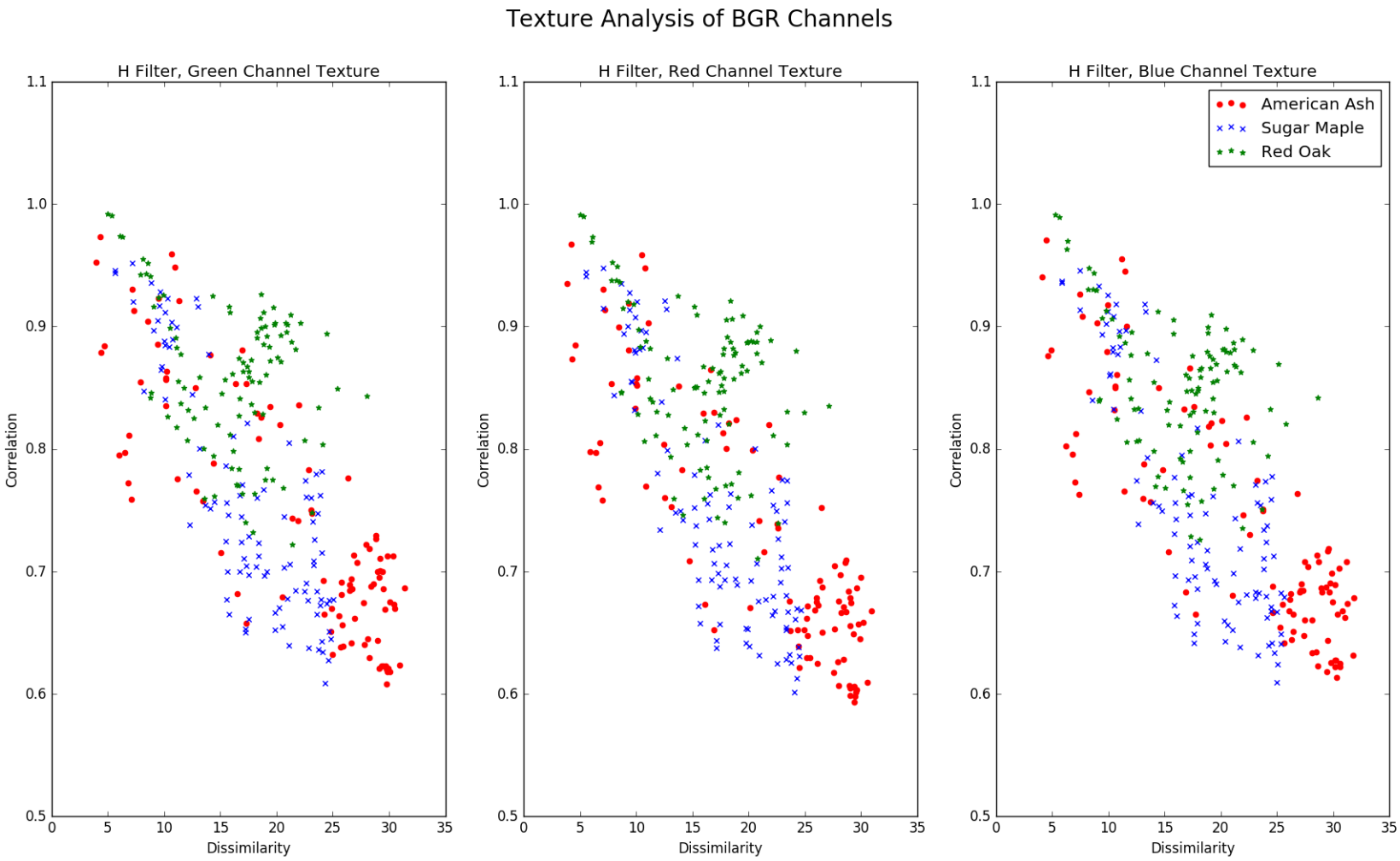


Figure 1: H filter GLCM Specular - All Species

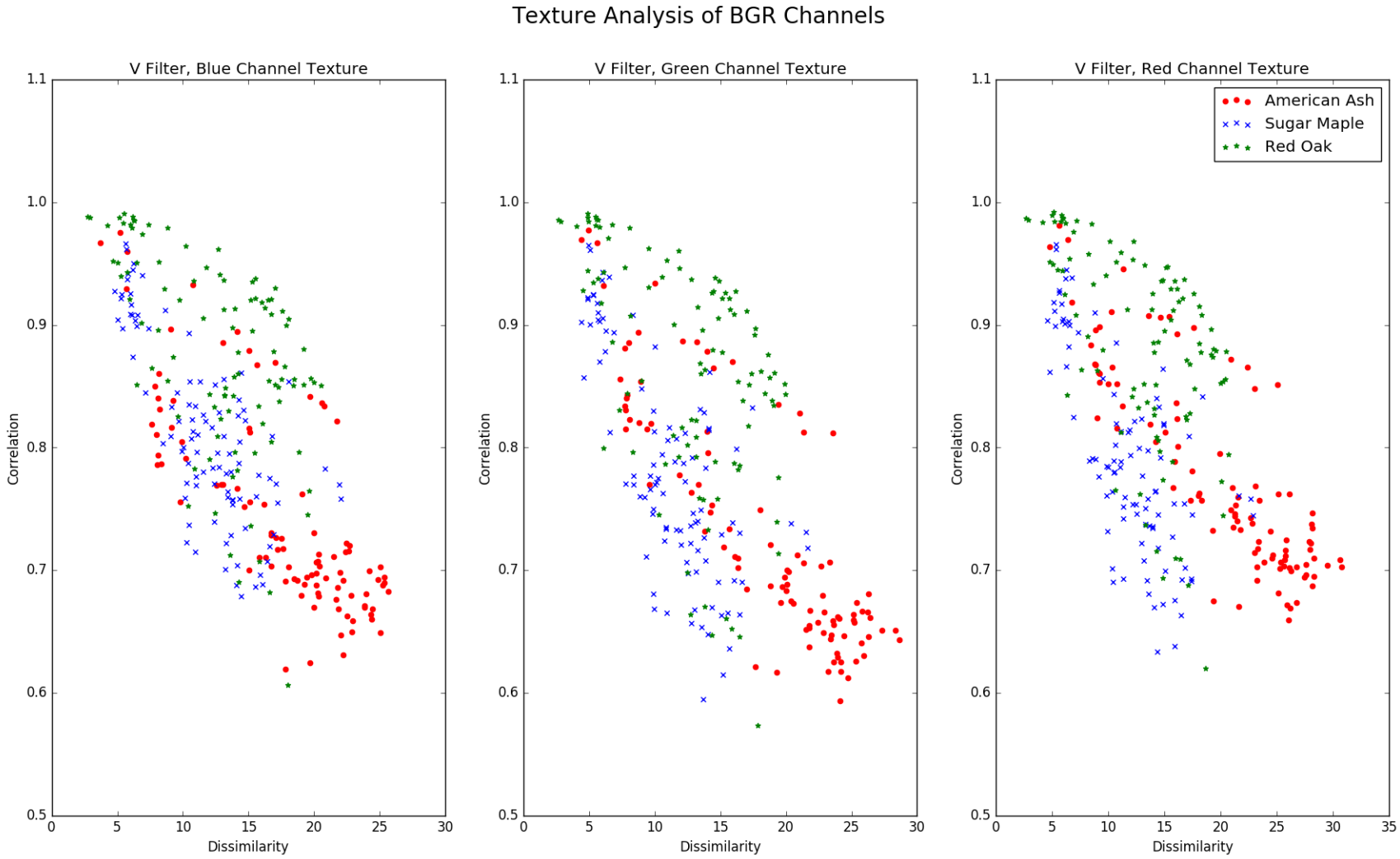


Figure 2: V filter GLCM Specular - All Species

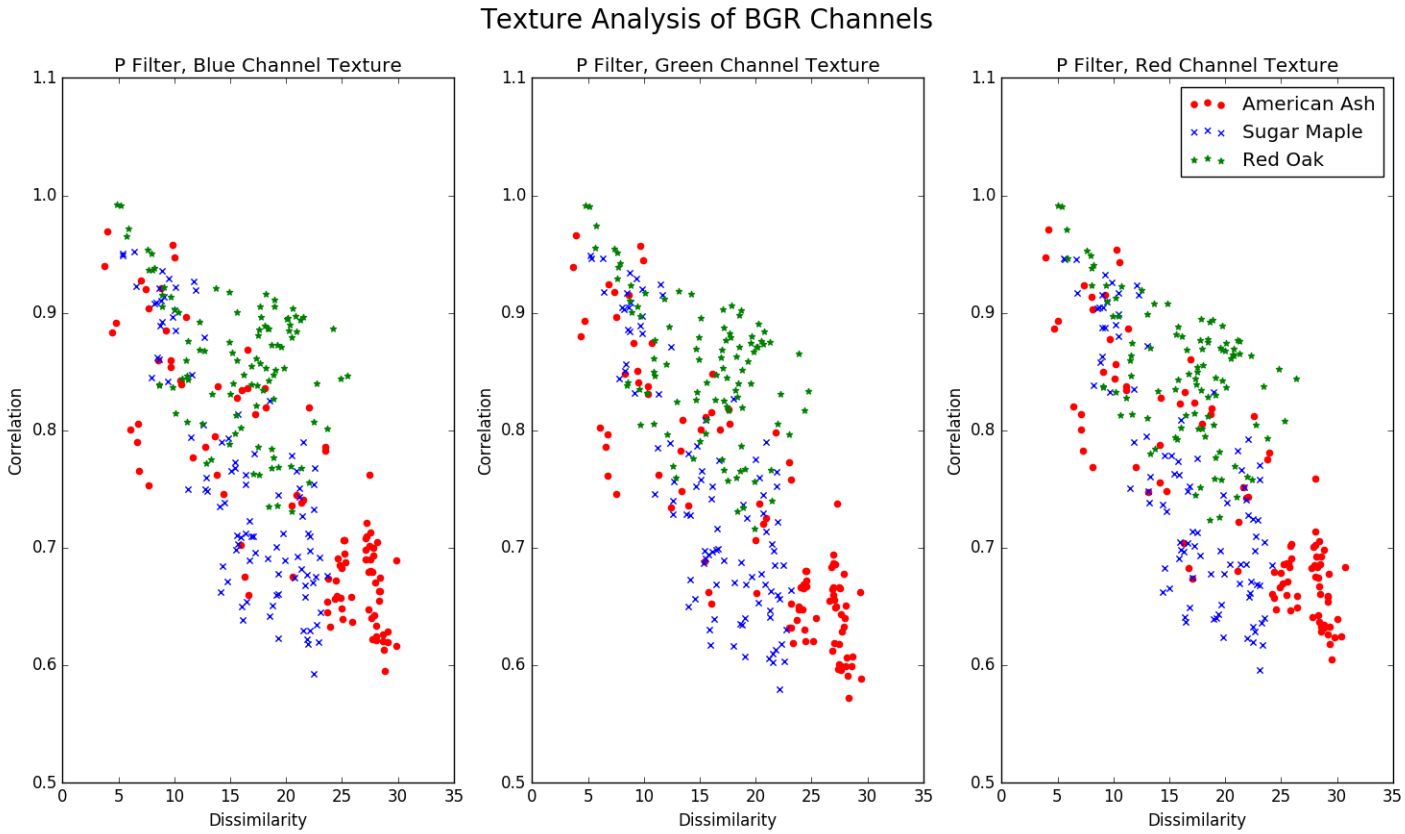


Figure 3: P filter GLCM Specular - All Species

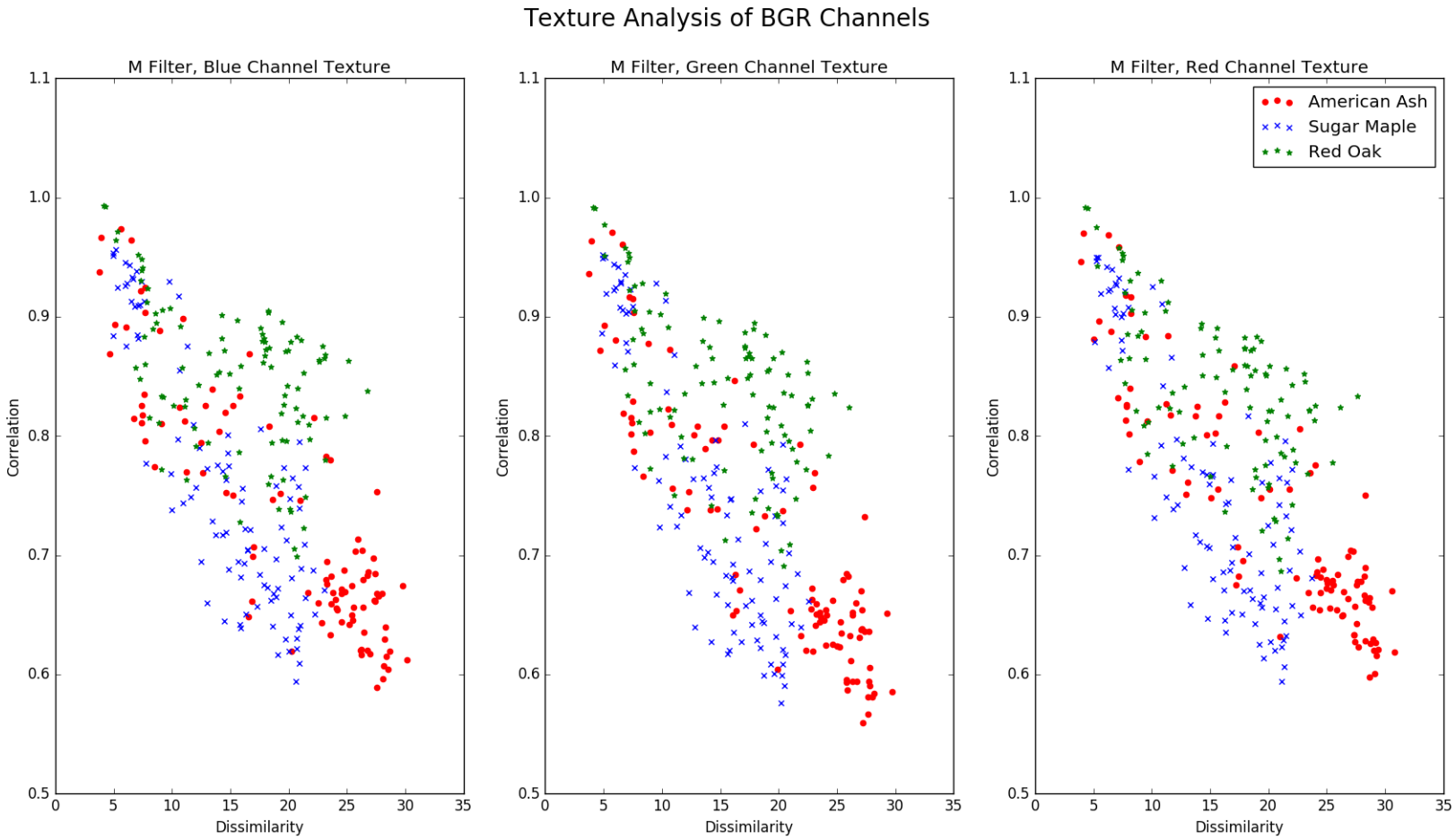


Figure 4: M filter GLCM Specular - All Species

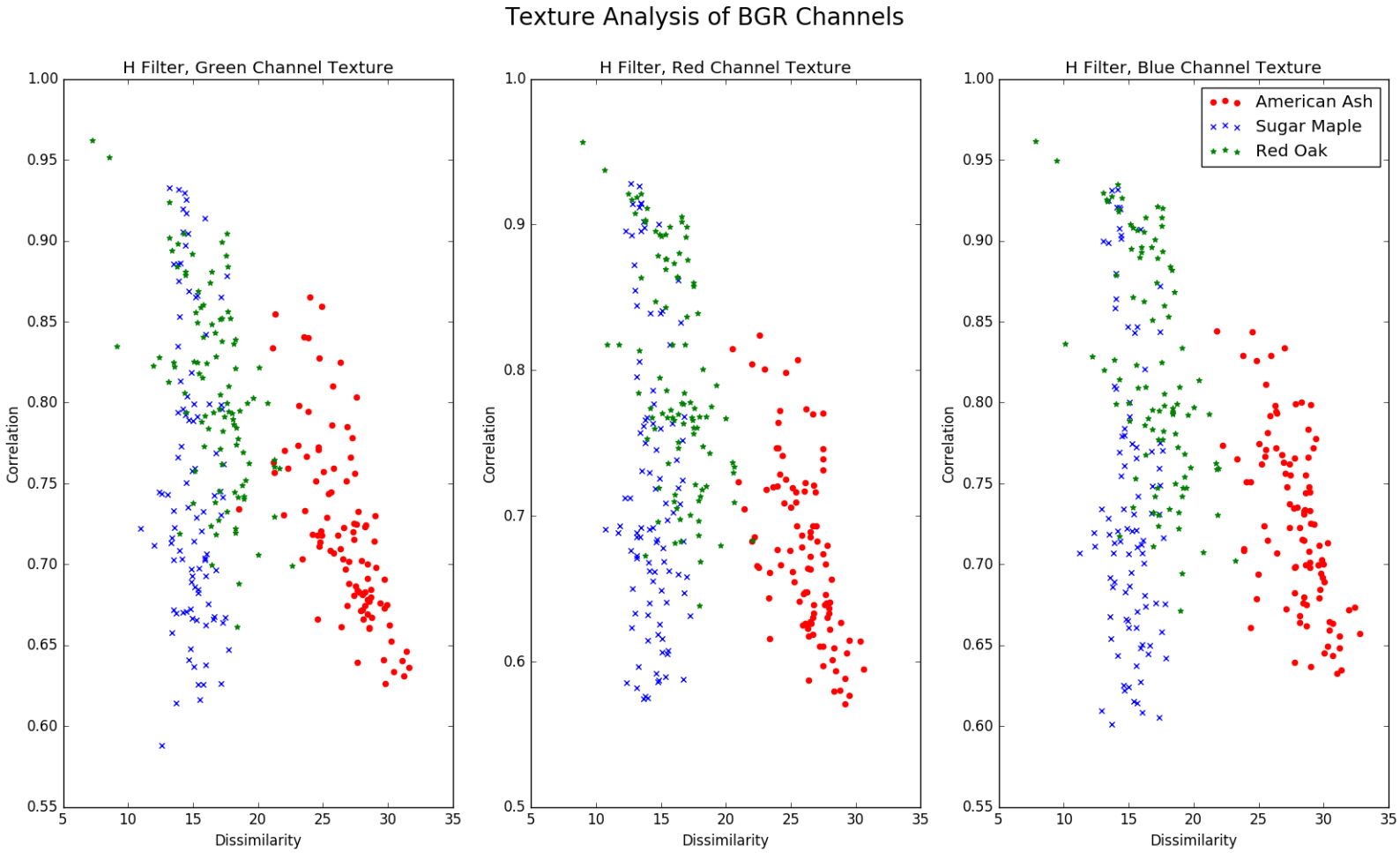


Figure 5: H filter GLCM Diffuse - All Species

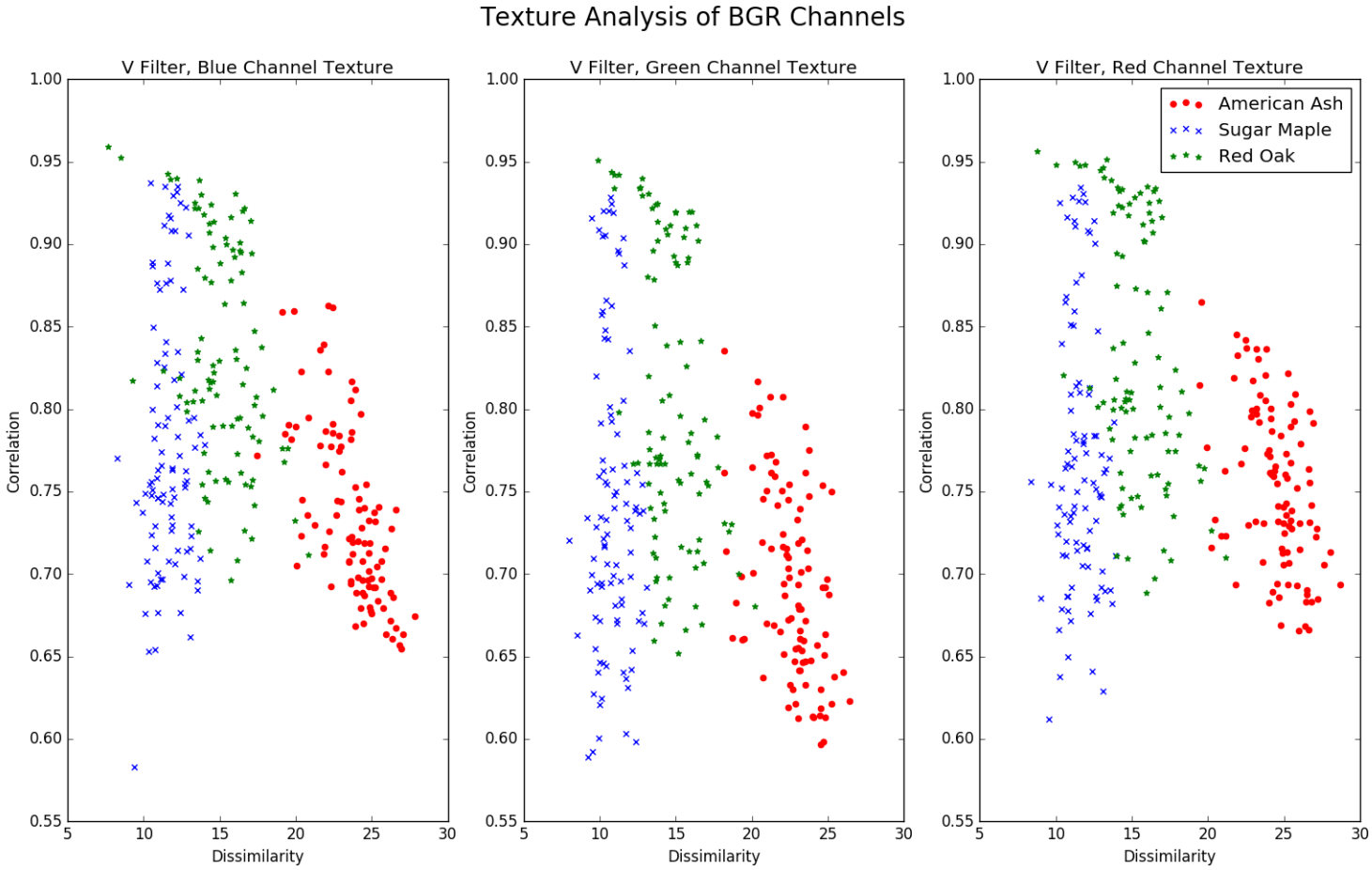


Figure 6: V filter GLCM Diffuse - All Species

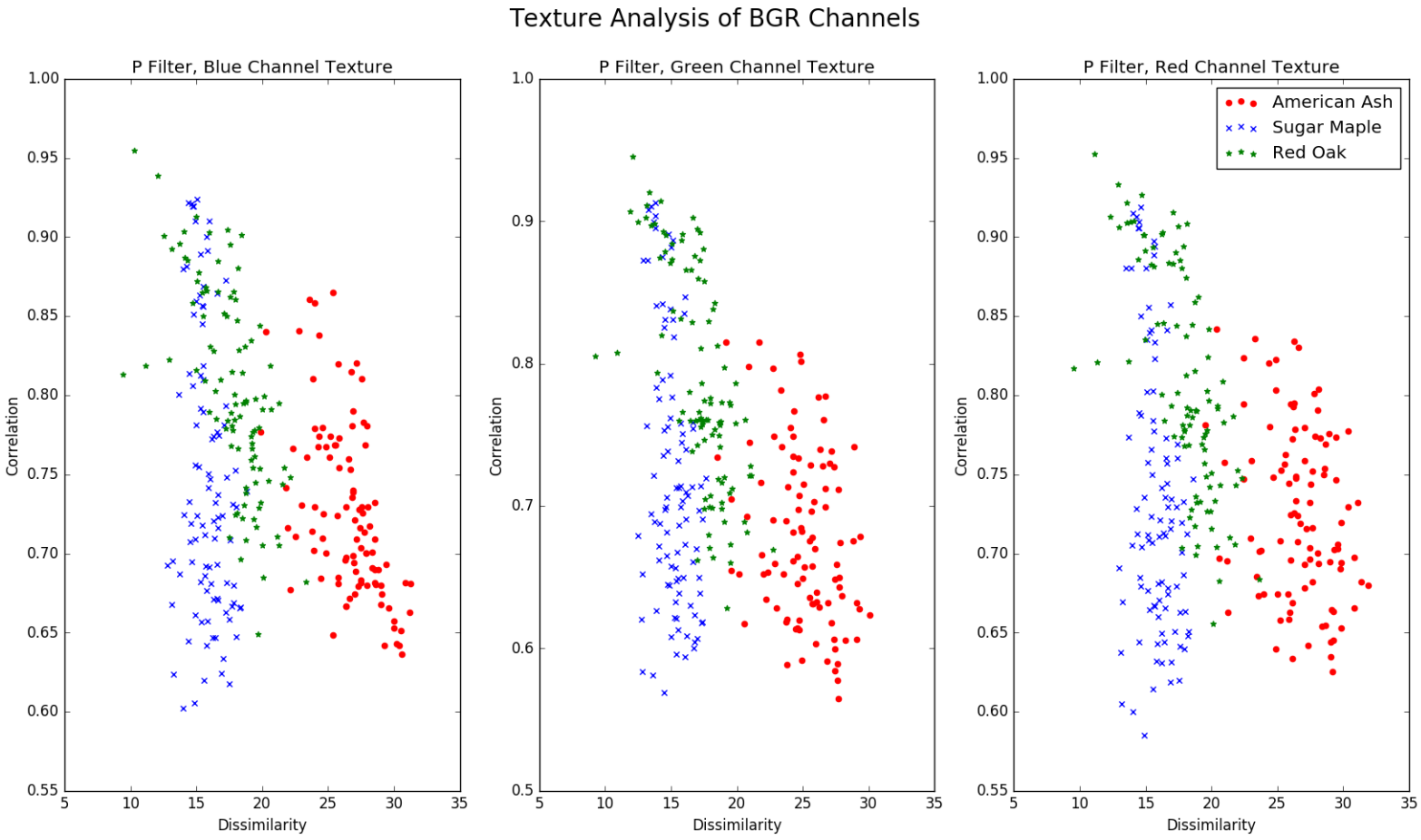


Figure 7: P filter GLCM Diffuse - All Species

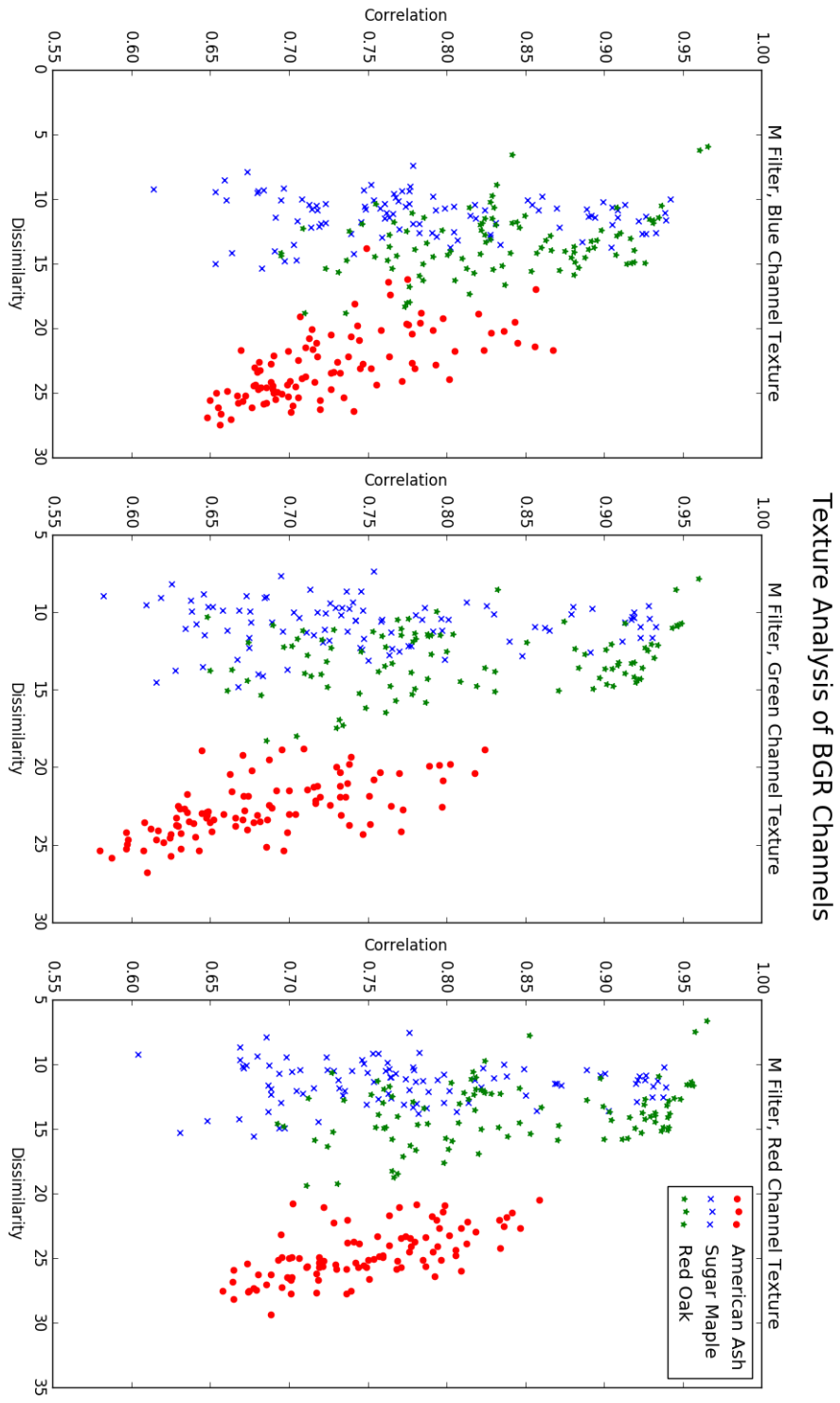


Figure 8: M filter GLCM Diffuse - All Species

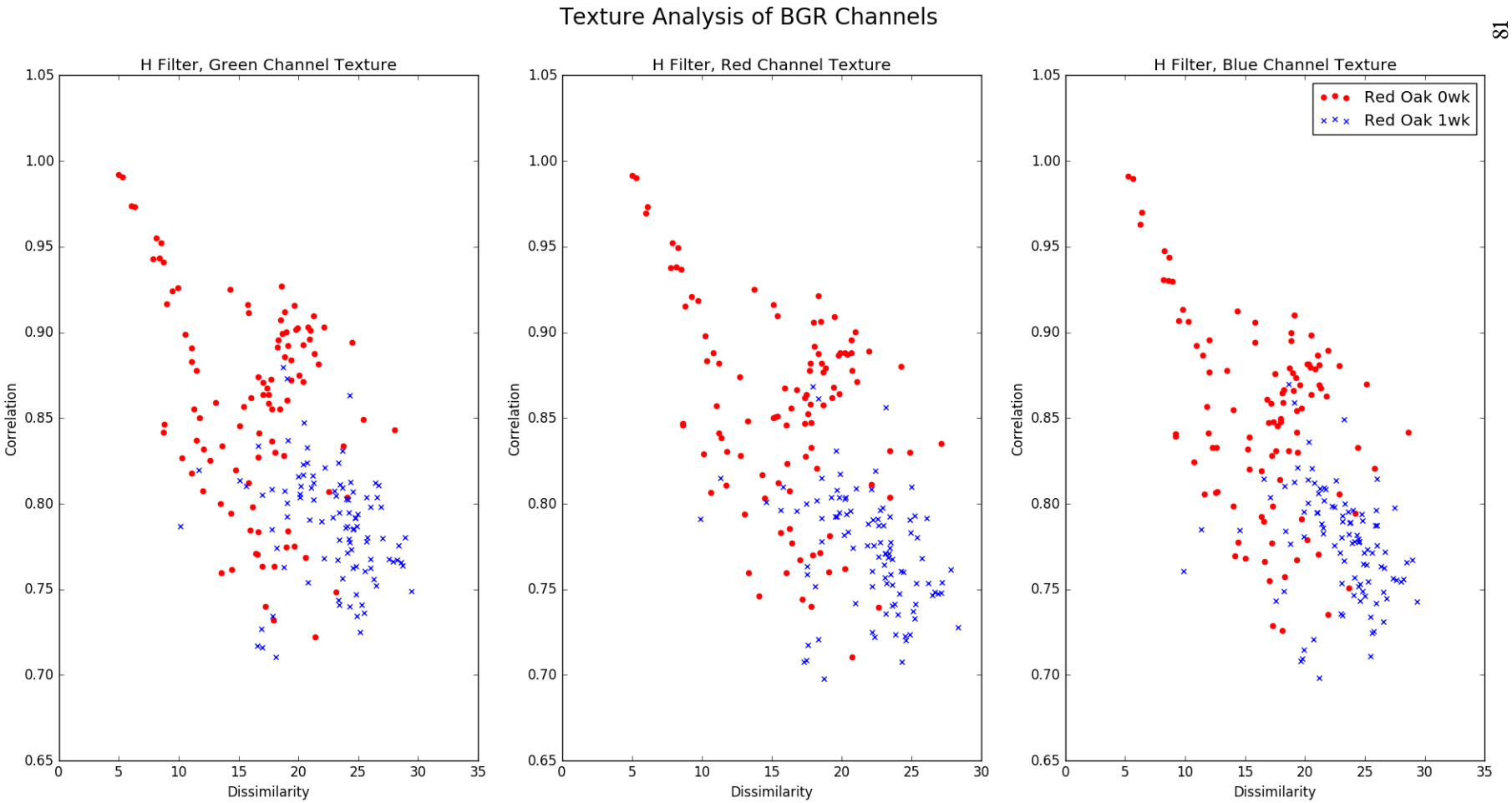


Figure 9: H filter GLCM Specular Decomposition - Red Oak

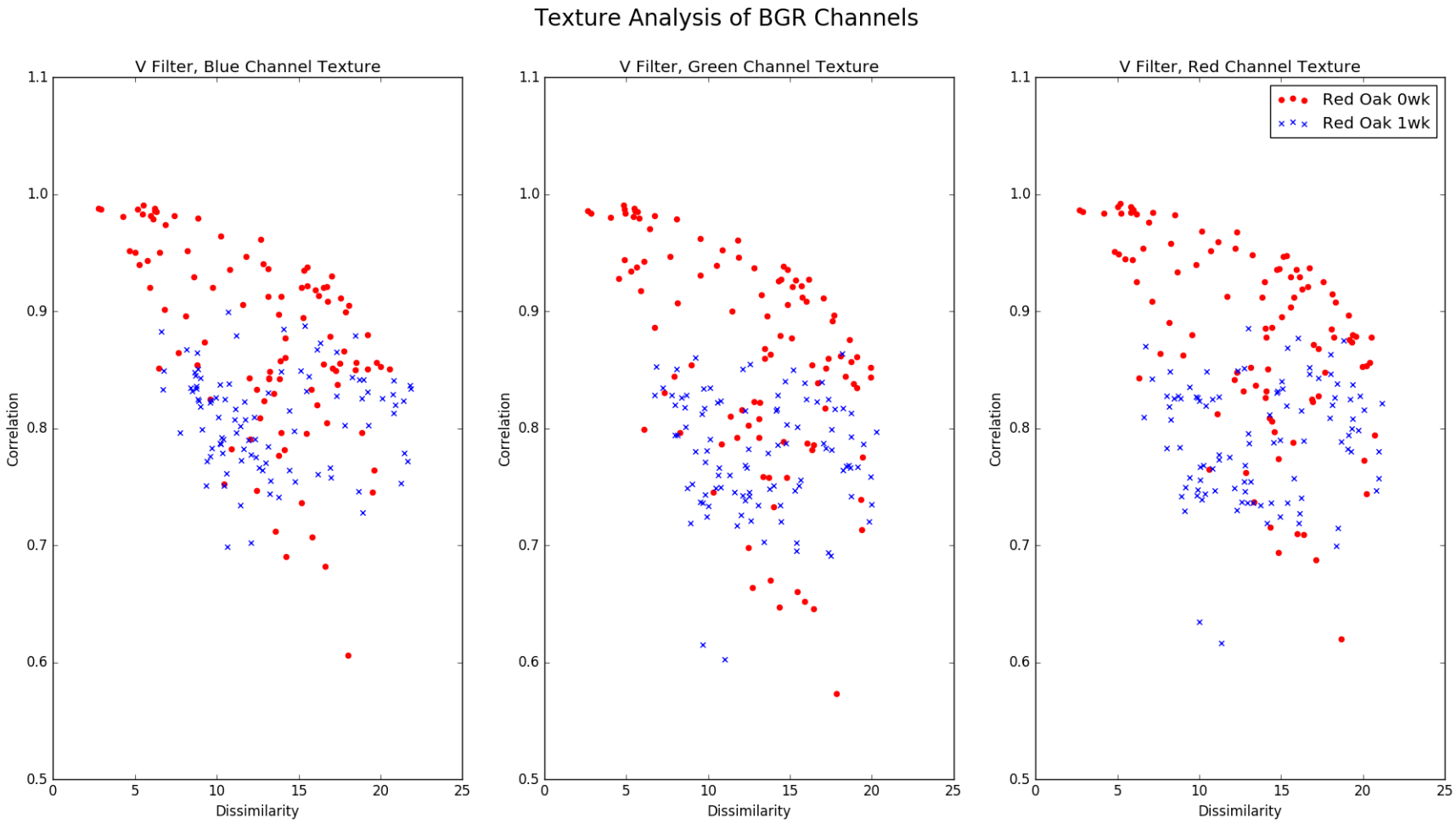


Figure 10: V filter GLCM Specular Decomposition - Red Oak

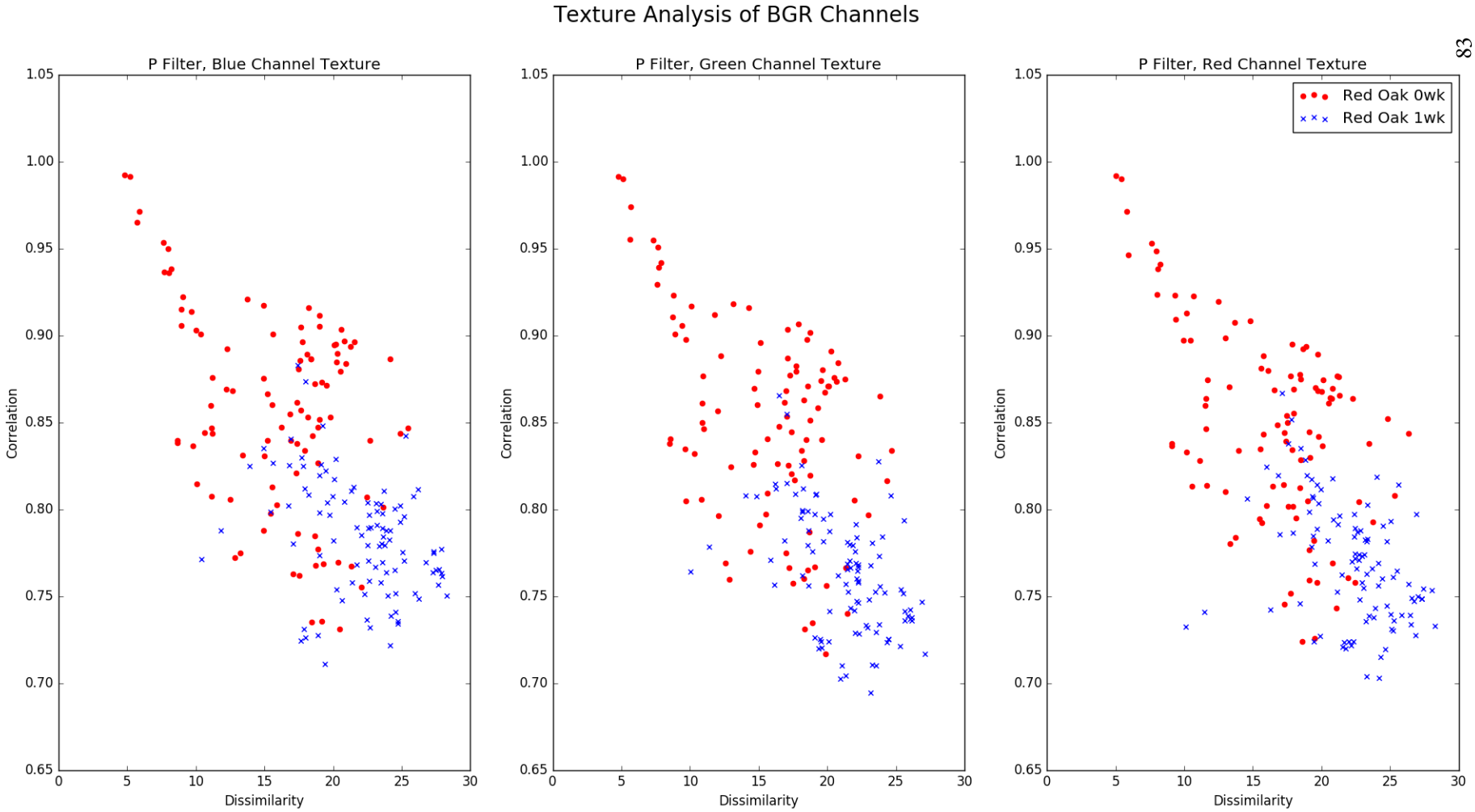


Figure 11: P filter GLCM Specular Decomposition - Red Oak

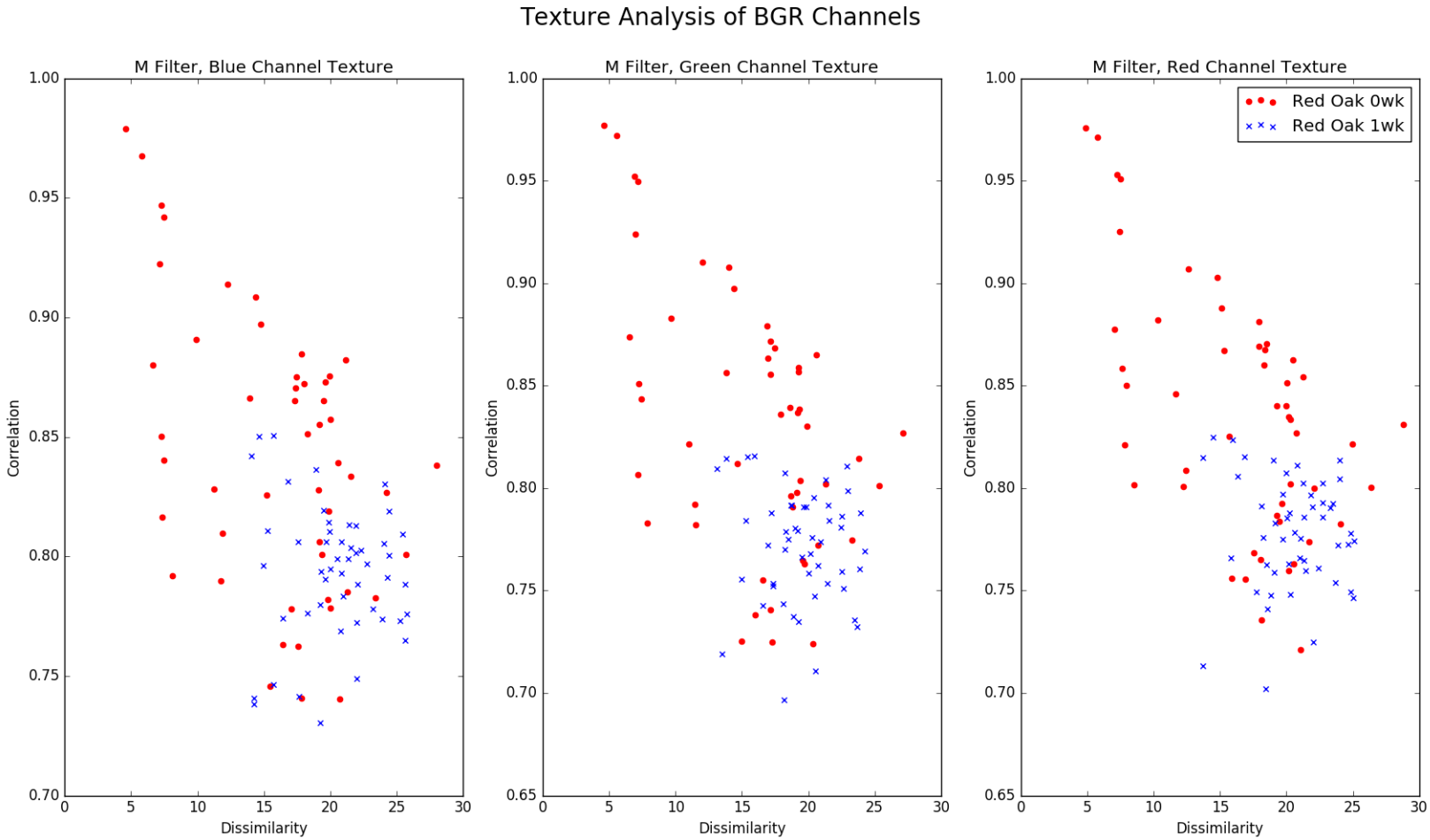


Figure 12: M filter GLCM Specular Decomposition - Red Oak

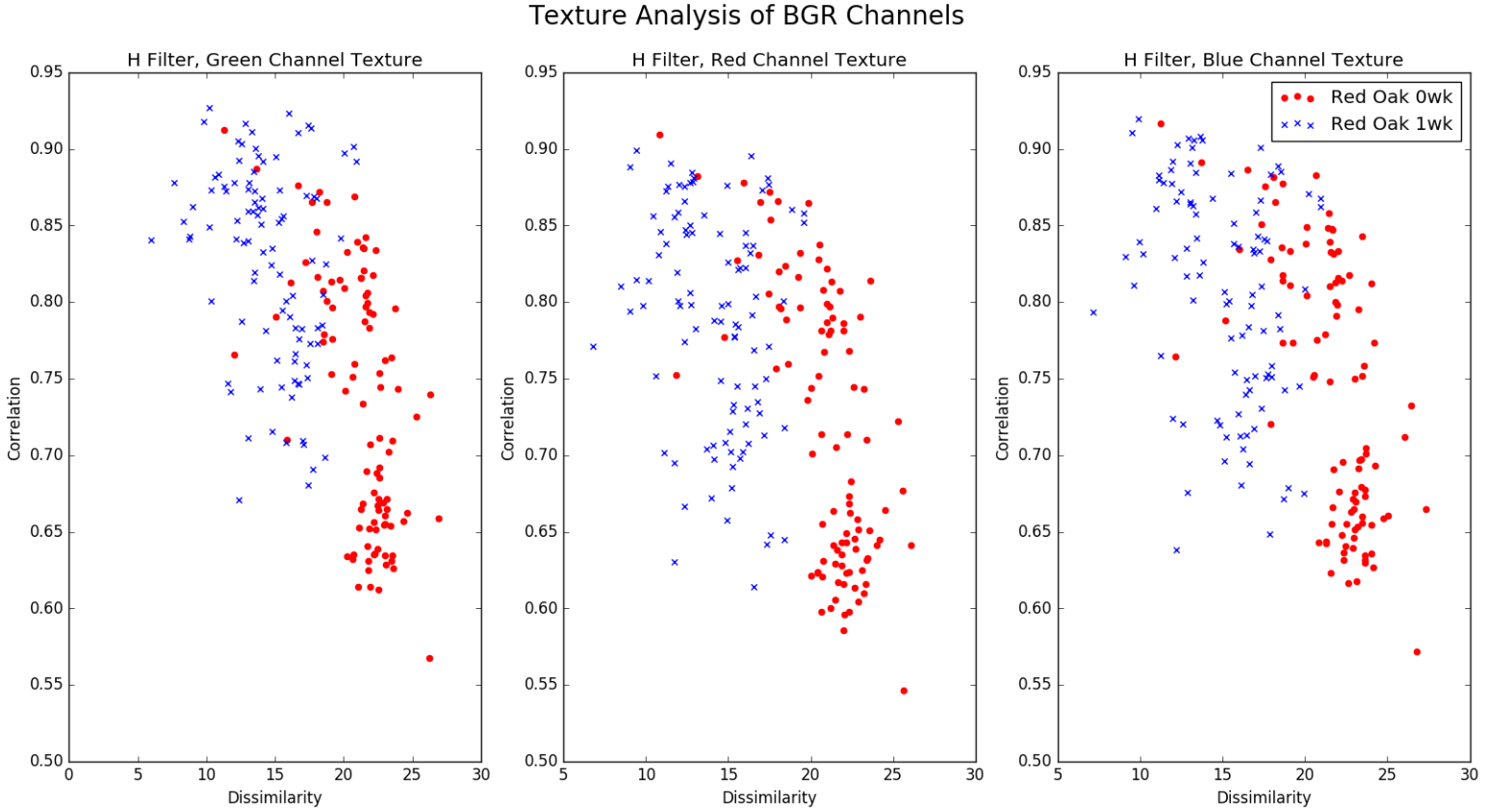


Figure 13: H filter GLCM Diffuse Decomposition - Red Oak

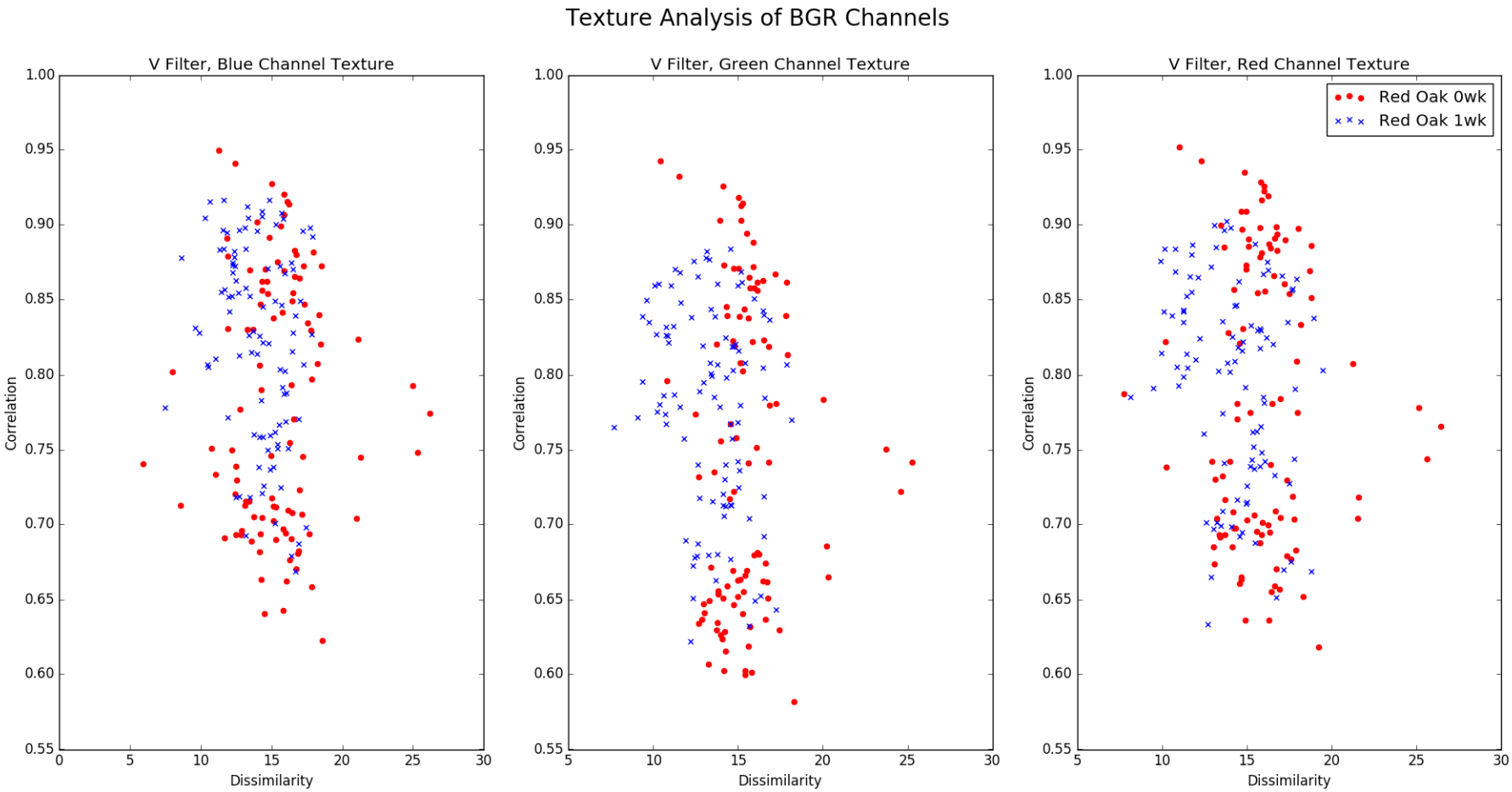


Figure 14: V filter GLCM Diffuse Decomposition - Red Oak

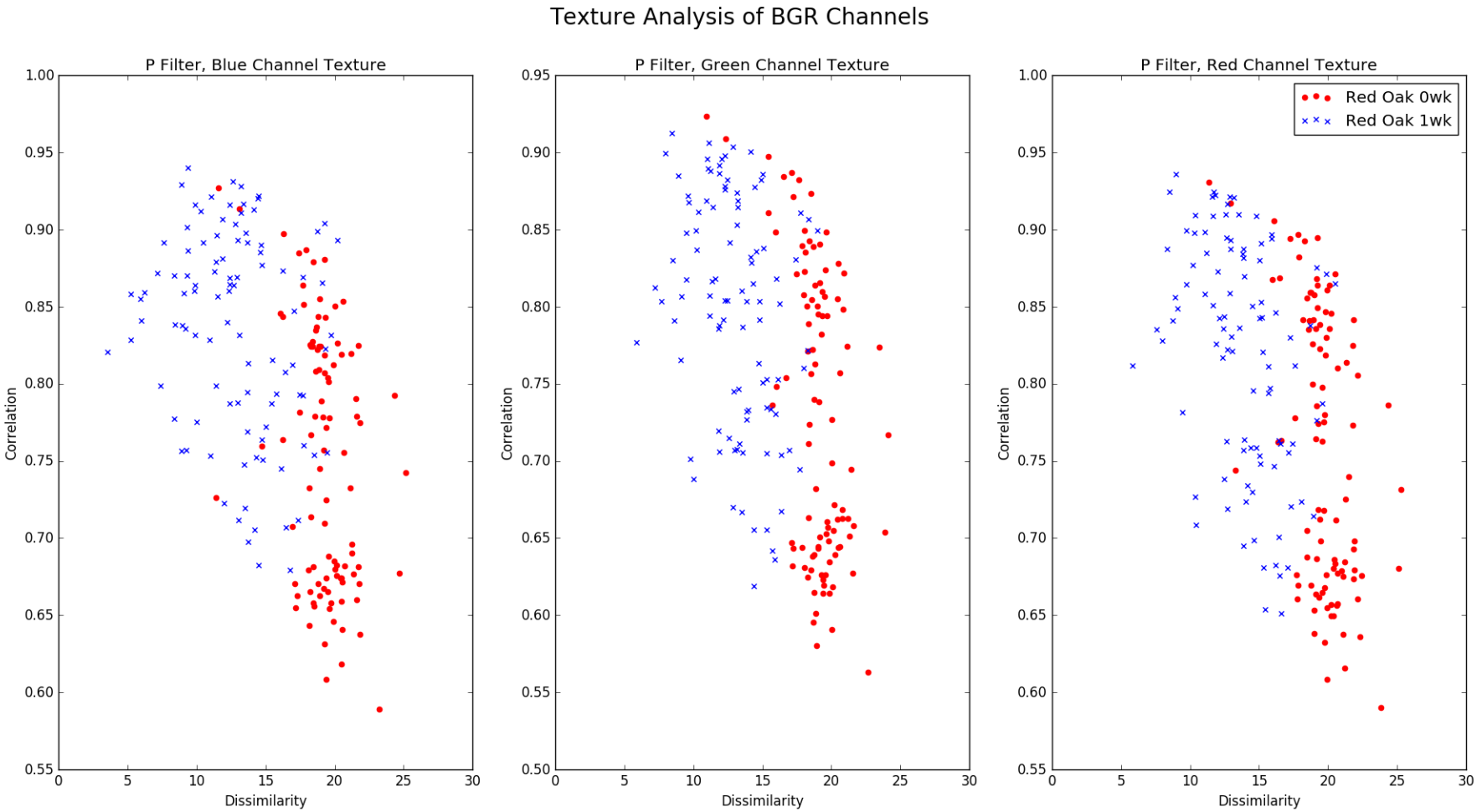


Figure 15: P filter GLCM Diffuse Decomposition - Red Oak

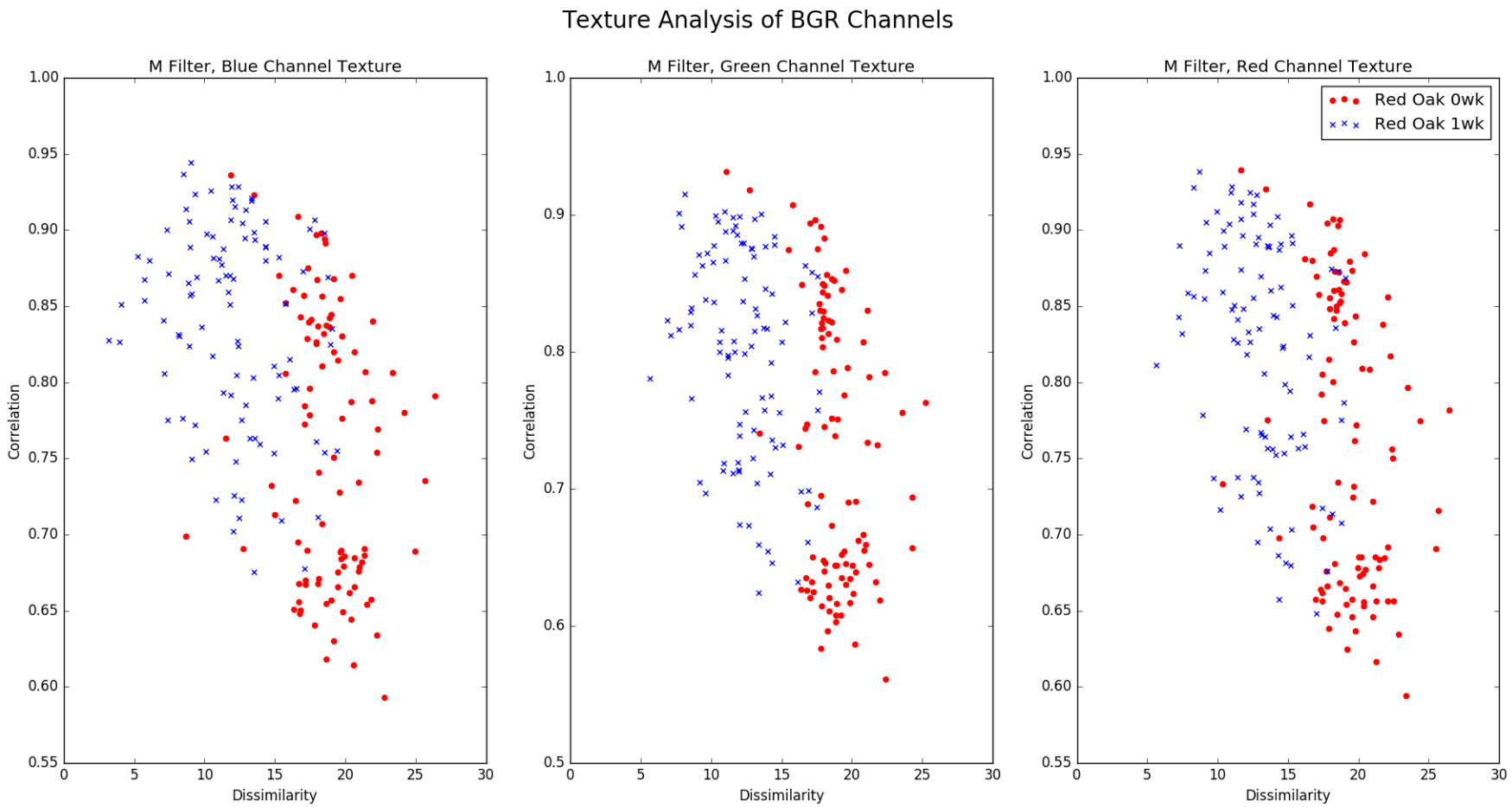


Figure 16: M filter GLCM Diffuse Decomposition - Red Oak

# Bibliography


1. R. Scott. *Linear Circuits*. Addison-Wesley Educational Publishers Inc, 1960. ISBN: 9780201068207.
2. Dabbiru, Aanstoos, Ball, and Younan. "Screening Mississippi River Levees Using Texture-Based and Polarimetric-Based Features from Synthetic Aperture Radar Data", 2017.
3. M. Karjalainen, H. Kaartinen, and J. Hyyppä. "Agricultural Monitoring Using Envisat Alternating Polarization SAR Images". *Photogrammetric Engineering & Remote Sensing* 1, 2008, pp. 117–126. DOI: https://doi.org/10.14358/PERS.74.1.117.
4. T. Lillesand, R. Kiefer, and J. Chipman. *Remote Sensing and Image Interpretation*. Wiley, 2007. ISBN: 9780470052457.
5. L. Soh. "Texture Analysis of SAR Sea Ice Imagery Using Gray Level Co-Occurrence Matrices". *IEEE Transactions on Geoscience and Remote Sensing* 37:2, 1999, pp. 780–795. DOI: https://doi.org/10.1109/36.752194.
6. R. Bosch. "Plant Classification System for Crop / Weed Discrimination Without Segmentation". *Applications of Computer Vision (WACV), 2014 IEEE Winter Conference*, 2014. DOI: https://doi.org/10.1109/WACV.2014.6835733.
7. D. Maxwell, J. Partridge, N. Roberts, N. Boonham, and G. Foster. "The Effects of Plant Virus Infection on Polarization Reflection from Leaves". *PLoS ONE* 11:4, 2016. DOI: https://doi.org/10.1371/journal.pone.0152836.
8. A. Bhardwaj, M. Kaur, and A. Kumar. "Recognition of plants by Leaf Image using Moment Invariant and Texture Analysis". *International Journal of Innovation and Applied Studies* 3:1, 2013, pp. 237–248.
9. S. Askraba, A. Paap, and K. Alameh. "Laser-Stabilized Real-Time Plant Discrimination Sensor for Precision Agriculture". *IEEE Sensors Journal* 16:17, 2016. DOI: http://dx.doi.org/10.1109/JSEN.2016.2582908.
10. J. Maxwell. *Dynamical Theory of the Electromagnetic Field*. Philosophical Transactions of the Royal Society, 1865. ISBN: 9781603866163.
11. M. Reigosa Roger. *Handbook of Plant Ecophysiology Techniques*. Springer Science & Business Media, 2001. ISBN: 9780792370536.
12. R. Chipman. *Polarimetry*. Handbook of Optics. McGraw-Hill Education, 2009. ISBN: 9780071498890.
13. E. Collett. *Field Guide to Polarization*. URL: https://spie.org/publications/fg05_p07-09_polarization_ellipse?SSO=1.
14. D. Goldstein. *Polarized Light*. CRC Press, 2003. ISBN: 9781439830406.
15. G. Giakos. "Polarimetric Phenomenology of Light Interaction with Early Lung Cancer Stages". *Measurement Science and Technology* 22:11, 2011.

16. R. Priest and T. Germer. "Polarimetric BRDF in the Microfacet Model: Theory and Measurements". *Proceedings of the Military Sensing Symposia (MSS) Specialty Group Meeting on Passive Sensors*, 2000.

17. I. Renhorn, T. Hallberg, and G. Boreman. "Polarimetric BRDF in the Microfacet Model: Theory and Measurements". *Swedish Defense Research Agency*, 2015.

18. J. Schott. *Fundamentals of Polarimetric Remote Sensing*. SPIE Tutorial Text. SPIE–The International Society for Optical Engineering, 2009. ISBN: 9780819475343.

19. L. Wolff. "Classification Of Material Surfaces Using The Polarization Of Specular Highlights". *SPIE Optics, Illumination, and Image Sensing for Machine Vision III* 1005, 1989. DOI: http://dx.doi.org/10.1117/12.949046.

20. L. Grant. "Diffuse and Specular Characteristics of Leaf Reflectance". *Remote Sensing of Environment* 22:2, 1987, pp. 309–322. DOI: https://doi.org/10.1016/0034-4257(87)90064-2.

21. G. Meister, R. Wiemker, and R. Monno. "Investigation on the Torrance-Sparrow specular BRDF model". *Geoscience and Remote Sensing Symposium Proceedings*, 1998. DOI: http://dx.doi.org/10.1109/IGARSS.1998.703752.

22. R. Montes and C. Ureña. "An Overview of BRDF Models", 2012.

23. F. Nicodemus. "Geometrical Considerations and Nomenclature for Reflectance ", 1977.

24. R. Haralick. "Textural Features for Image Classification". *IEEE Transactions on Systems, Man, and Cybernetics* SMC:3, 1973, pp. 610–621. DOI: https://doi.org/10.1109/TSMC.1973.4309314.

25. M. Hall-Beyer. *GLCM Texture: A Tutorial*. URL: https://prism.ucalgary.ca/handle/1880/51900.

26. N. Zayed and H. Elnemr. "Statistical Analysis of Haralick Texture Features to Discriminate Lung Abnormalities". *International Journal of Biomedical Imaging* 2015:10, 2015, p. 7. DOI: http://dx.doi.org/10.1155/2015/267807.

27. T. Yeats and J. Rose. "The Formation and Function of Plant Cuticles". *Plant Physiology* 163:9, 2013, pp. 5–20. DOI: https://doi.org/10.1104/pp.113.222737.

28. R. Munns, S. Schmidt, and C. Beveridge. *Plants in Action*. URL: http://plantsinaction.science.uq.edu.au/book/export/html/4.

29. S. Akıncı and D. Lösel. *Plant Water-Stress Response Mechanisms*. URL: https://www.intechopen.com/books/water-stress/plant-water-stress-response-mechanisms.

30. Brown, Lemay, Bursten, Murphy, and Woodward. *Chemistry the Central Science*. International Version. Prentice Hall, 2011. ISBN: 9780321696724.

31. R. Myneni and J. Ross. *Photon Vegetation Interactions*. Applications in Optical Remote Sensing and Plant Ecology. Springer-Verlag, 1991. ISBN: 9783642753916.

32. H. G. Solutions. *Broadband Greenness*. URL: http://www.harrisgeospatial.com/docs/BroadbandGreenness.html#Visible.

33. V. Vanderbilt, L. Grant, and C. Daughtry. "Polarization of Light Scattered by Vegetation". *Proceedings of the IEEE* 73:6, 1985. DOI: http://dx.doi.org/10.1109/PROC.1985.13232.

34. Bousquet, Lacherade, Jacquemoud, and Moya. "Leaf BRDF measurements and model for specular and diffuse components differentiation". *Remote Sensing of Environment* 98:2-3, 2005, pp. 201–211. DOI: https://doi.org/10.1016/j.rse.2005.07.005.

35. G. Atkinson and E. Hancock. "Recovery of Surface Orientation from Diffuse Polarization". *IEEE Transactions on Image Processing* 15:6, 2006. DOI: http://dx.doi.org/10.1109/TIP.2006.871114.

36. G. Atkinson and E. Hancock. "Shape from Diffuse Polarisation", 2004. DOI: http://dx.doi.org/10.5244/C.18.94.

37. N. Ericksen. *noobElectric*. URL: https://github.com/nicholasericksen/noobElectric.

38. F. Tanentzap, A. Stempel, and P. Ryser. "Reliability of Leaf Relative Water Content (RWC) Measurements after Storage: Consequences for in situ Measurements". *Botany* 93:9, 2015. DOI: https://doi.org/10.1139/cjb-2015-0065.

39. Wikipedia. *Receiver operating characteristic*. URL: https://en.wikipedia.org/wiki/Receiver_operating_characteristic.

40. G. James, D. Witten, T. Hastie, and R. Tibshirani. *An Introduction to Statistical Learning: with Applications in R*. Springer Texts in Statistics. Springer, 2017. ISBN: 9781461471370.

41. *Leaf Structure and Pigments*. URL: http://w3.marietta.edu/~biol/introlab/Leaves%20and%20Pigments.pdf.